Alternative winding patterns for twisted solenoid coils with improved characteristics for TRASE MRI

by

Nahid Ghomimolkar

A Thesis submitted to the Faculty of Graduate and Postdoctoral Studies of
the University of Manitoba
in partial fulfillment of the requirements of the degree of

Master of Science

Department of Physics and Astronomy
University of Manitoba
Winnipeg, Manitoba, Canada

Abstract

Magnetic resonance imaging (MRI) is a powerful noninvasive imaging modality; however, conventional high-field MRI systems rely on strong static magnetic fields and gradient coils, resulting in high system complexity, power consumption, acoustic noise, and limited accessibility. The development of low-field MRI systems has the potential to alleviate several of these challenges and motivate alternative spatial encoding techniques. One such approach is transmit array spatial encoding (TRASE). This gradient-free MRI method encodes spatial information using phase gradients in the radiofrequency (RF) magnetic field rather than static magnetic field gradients.

The twisted solenoid is the most commonly used RF coil geometry for TRASE MRI studies employing vertical B_0 magnets. While return wires must by necessity be included in experimental implementations of such coils, their effects are often neglected in theoretical modeling and simulation studies. This discrepancy motivates a systematic investigation of coil winding configurations and their influence on RF field characteristics relevant to TRASE imaging.

In this thesis, four winding patterns for twisted solenoid–based RF coils are investigated, including conventional configurations with and without an explicitly modeled return wire, as well as two alternative designs proposed in this work. The proposed designs are derived using stream function and surface current density concepts and include a discretized loop-based model and a double-wound wire configuration composed of two simple twisted solenoids. These winding patterns are compared in terms of magnetic field uniformity, RF phase behavior, and phase gradient linearity in the context of low-field MRI, including the influence of the concomitant B_1 field component. The results demonstrate that our proposed winding patterns significantly improve B_1 field uniformity and phase gradient linearity compared to conventional twisted solenoid designs. These configurations eliminate the symmetry-breaking effects introduced by return wires and provide a practical and effective path forward for the development of RF phase-gradient coils for low-field TRASE MRI.

Furthermore, truncated versions of all winding patterns are examined to assess their robustness to coil-length reduction. Numerical simulations based on the Biot–Savart law are used to quantify the impact of coil geometry on TRASE MRI performance. The results provide insight into the role of winding configuration in determining RF field quality and support the identification of optimized coil designs for low-field TRASE MRI.

Keywords:

Nuclear magnetic resonance (NMR)

Magnetic resonance imaging (MRI)

Transmit array spatial encoding (TRASE)

MRI coil

Radio frequency (RF) field

Twisted solenoid

Contributions of Authors

This thesis includes material from the following published manuscript:

N. Ghomimolkar, A. E. Krosney, and C. P. Bidinosti, "Alternative winding patterns for twisted solenoid coils with improved characteristics for TRASE MRI," *Journal of Magnetic Resonance*, vol. 388, 108068, 2026.

I, Nahid Ghomimolkar, performed the research presented in this manuscript, building on earlier preliminary work. I independently developed the simulation code, carried out the electromagnetic simulations and analysis of the proposed winding patterns, extended the work to include truncated coil designs and a solution to the return-wire problem, prepared the figures, and wrote the original draft of the manuscript.

Alexander E. Krosney conducted a preliminary study of the proposed winding patterns, which informed this work.

Prof. Christopher P. Bidinosti was the principal investigator and conceived the original idea for the project. He secured funding, supervised the research, provided guidance on the methodology and analysis, and reviewed and edited the manuscript.

All remaining chapters of this thesis are my own original work.

Acknowledgment

I would first like to express my deepest gratitude to my supervisor, Dr. Christopher Bidinosti, for his invaluable guidance, support, and mentorship throughout this journey. Beyond the scientific guidance provided in this work, your encouragement and understanding meant a great deal to me. You were always kind and patient in answering my questions and were generous with your time for discussions, despite your many responsibilities. I am sincerely grateful for your support.

I would also like to thank my family for their endless love and encouragement. My heartfelt thanks go to my mother, who has always believed in me and stood by my side, and to my father, whose spirit continues to inspire and guide me.

I am also deeply thankful to my dear friends, whose encouragement and support gave me strength and motivation during difficult moments and helped me continue this journey.

Finally, I would like to thank the Department of Physics and Astronomy for their continuous support and assistance. Their responsiveness and help made this path smoother and more manageable.

Contents

List of Tables

List of Figures

Chapter 1

Magnetic Resonance Imaging

1.1 Review

Magnetic resonance imaging (MRI) is a non-invasive medical imaging modality based on nuclear magnetic resonance (NMR) phenomena and is widely used to generate detailed images of internal anatomical structures. Image formation relies on carefully controlled magnetic fields and the precise application of radiofrequency (RF) electromagnetic fields. When a subject is placed inside a strong static magnetic field, the nuclear spins of certain atoms, most notably hydrogen, tend to align with the static magnetic field of the MRI scanner. An applied RF excitation perturbs this alignment, and as the spins relax back toward equilibrium, they induce voltages in nearby detection coils. These electromagnetic signals are detected and processed [1]. Both the phase and amplitude of the received signals play a central role in spatial encoding and image contrast in MRI.

Compared with other imaging modalities such as computed tomography (CT), MRI provides superior soft-tissue contrast due to its sensitivity to intrinsic tissue properties. In addition, MRI allows image acquisition in arbitrary planes without physically repositioning the subject. Because MRI relies on magnetic fields and RF excitation rather than potentially harmful ionizing radiation, it has become a widely adopted imaging technique across a broad range of clinical and research applications

Over the past several decades, MRI has undergone substantial development driven by advances in data acquisition methods, image reconstruction algorithms, and hardware design. Early MRI systems were primarily focused on producing anatomical images suitable for routine clinical use and are often referred to as conventional MRI systems. In practice, however, limitations such as image artifacts, restricted contrast mechanisms, and sensitivity to physiological motion motivated the development of more advanced imaging techniques [2]. Examples include diffusion-weighted imaging (DWI), perfusion imaging, magnetization transfer imaging, and functional MRI (fMRI). These approaches enhance sensitivity to specific biological or physical processes by exploiting differences in signal phase, timing, or contrast behavior.

In modern clinical settings, MRI systems most commonly operate at static magnetic field strengths of 1.5 T and 3 T and are therefore classified as high-field or conventional MRI systems. Increasing the magnetic field strength improves the intrinsic signal-to-noise ratio (SNR), which enables higher spatial resolution, faster imaging, and more sophisticated contrast mechanisms. Ultra-high-field MRI systems operating at 7 T provide further gains in SNR and improved sensitivity to susceptibility-based, functional, and spectroscopic contrasts, particularly in neuroimaging and musculoskeletal applications. These benefits, however, come with significant technical challenges. RF field inhomogeneity, increased specific absorption rate (SAR), and greater system complexity remain major obstacles and currently limit the widespread clinical deployment of ultra-high-field MRI systems [3].

Despite their strong diagnostic performance, high-field and ultra-high-field MRI systems are among the most expensive medical imaging technologies. High purchase costs, complex installation requirements, and ongoing operational expenses restrict their availability primarily to well-resourced healthcare environments. As a result, access to MRI remains limited in many low- and middle-income regions [4, 5]. In recent years, this has led to renewed interest in low-field MRI as a complementary and more accessible imaging approach. Low-field MRI systems offer advantages such as reduced cost, simpler infrastructure, improved portability, and greater flexibility in magnet geometry. Although operation at lower field strengths inherently reduces SNR, recent advances in acquisition strategies and image reconstruction increasingly emphasize diagnostic utility rather than direct equivalence with high-field image quality [6, 7, 8].

While low-field and high-field MRI systems differ substantially in their hardware implementation and performance characteristics, their fundamental operating principles remain the same. In conventional MRI, spatial encoding is achieved using time-varying magnetic field gradients superimposed on the static magnetic field. The generation and rapid switching of these gradients require substantial electrical power, contribute significantly to system cost and complexity, and can induce eddy currents in surrounding conductive structures. These issues become particularly restrictive in low-field and portable MRI systems, where constraints on size, power consumption, and hardware simplicity are critical. As a consequence, the development of low-field MRI has intensified interest in alternative spatial encoding strategies that reduce or eliminate reliance on conventional gradient coils. Transmit array spatial encoding (TRASE) represents one such alternative to traditional gradient–based spatial encoding in

MRI. Originally proposed by Sharp and King [9], TRASE uses spatially varying phase gradients of the RF transmit field to achieve spatial encoding. This approach removes the need for conventional gradient coils and avoids several associated challenges, including acoustic noise and increased hardware complexity. Subsequent studies demonstrated the feasibility of high-resolution imaging using TRASE-based encoding schemes [10]. Recent studies have shown that radial TRASE can reduce system complexity with improved tolerance to coil coupling, making it well-suited for practical implementations [11]. These characteristics make TRASE particularly attractive for low-field MRI, where RF-based encoding provides a potential pathway toward simplified, portable, and energy-efficient scanner designs.

Despite its promise, the practical implementation of TRASE MRI remains strongly dependent on the design of RF transmit coils capable of producing controlled, efficient, and spatially linear phase gradients. Achieving these characteristics depends critically on the coil's geometry and winding pattern. In this thesis, alternative winding patterns for twisted solenoid coils are investigated to improve radiofrequency magnetic field (B_1) uniformity and phase-gradient performance relative to existing designs. This work contributes to the development of more effective RF phase-gradient coils for TRASE MRI, particularly for low-field imaging systems.

1.2 Thesis outline

This thesis is organized into six remaining chapters. Chapter 2 presents the fundamental principles of magnetic resonance imaging and describes how MR images are formed. Chapter 3 introduces the theoretical framework of TRASE MRI and outlines the RF coil design concepts relevant to this approach. Chapter 4 describes the methodology employed in this study, including the stream function and surface current techniques used to design the proposed RF coils. It also presents four twisted solenoid winding patterns, two of which represent novel contributions of this work. Chapter 5 evaluates the performance of the various coil designs through a comparative analysis of magnetic field magnitude, phase, and phase gradient. Chapter 6 investigates truncated versions of the optimized coil designs and examines the resulting changes in magnetic field distribution and phase gradient behavior. Finally, Chapter 7 summarizes the main findings of this research and discusses potential directions for future work.

Chapter 2

A Review of MRI

2.1 History of MRI

MRI is a medical imaging modality that has become an essential tool in clinical diagnosis and biomedical research. Its development is based on NMR, which describes how atomic nuclei respond to magnetic fields. Long before MRI became an imaging technique, NMR was studied as a physical effect with applications mainly in physics and chemistry.

Early experimental work dates back to the 1930s, when Rabi studied the magnetic properties of atomic nuclei and demonstrated that nuclear spins can interact with applied magnetic fields [12]. This part of the research was studied further by Bloch and Purcell in the 1940s, who independently observed nuclear magnetic resonance in condensed matter [13, 14]. Their work in NMR was so significant that it later earned them the Nobel Prize in Physics. For many years, NMR was used exclusively as a spectroscopic technique and had no application in imaging modality.

The transition from NMR spectroscopy to imaging occurred in the early 1970s. A key development was introduced by Lauterbur [15], who showed that spatial information could be encoded by applying small spatial variations in the magnetic field, known as magnetic field gradients, allowing signals from different locations to be distinguished. Magnetic field gradients are discussed in more detail in the following sections. This idea enabled the reconstruction of spatial images from NMR measurements. Shortly after, Ernst demonstrated the use of Fourier transform methods for image reconstruction [16], which significantly improved data acquisition efficiency and image quality. Mansfield later contributed to the development of rapid imaging techniques, including echo-planar imaging, which reduced scan times and helped move MRI closer to practical clinical use.

In 1977, the first MRI experiment on a human subject was successfully performed [17], marking a major step toward clinical adoption. Since that time, MRI technology has continued to evolve through improvements in magnet design, gradient hardware, RF systems, and computational methods. These advances have led to a wide range of imaging techniques that extend beyond anatomical imaging to include functional, diffusion, and quantitative approaches.

Overall, the historical progression of MRI reflects a gradual shift from fundamental studies of nuclear spin behavior to increasingly sophisticated methods for spatial encoding and image reconstruction. These foundational developments form the basis of modern MRI and motivate continued exploration of alternative encoding strategies beyond conventional gradient-based approaches, particularly those based on RF field manipulation and phase-gradient methods. Table 2.1 shows a brief history of MRI developments [1], with major milestones discussed immediately here.

Year	**Event**
1857–1952	Larmor relationship – Sir Joseph Larmor
1930	Rabi measured nuclei's magnetic properties
1946	MR phenomenon – Bloch and Purcell
1952	Nobel Prize – Bloch and Purcell
1950s–1970s	NMR developed as an analytical tool
1973	Back projection MRI – Lauterbur
1975	Fourier Imaging – Ernst
1977	Echo-planar imaging – Mansfield
1980	FT MRI demonstrated – Edelstein
1986	Gradient Echo Imaging, NMR Microscope
1987	MR Angiography – Dumoulin
1991	Nobel Prize – Ernst
1992	Functional MRI
1994	Hyperpolarized ^{129}Xe Imaging
2003	Nobel Prize – Lauterbur and Mansfield

Table 2.1: Brief history of MRI developments.

2.2 MRI principles

As mentioned above, the basis of MRI is NMR [18], which arises from the magnetic properties of atomic nuclei. An atom consists of protons, neutrons, and electrons, with protons and neutrons located in the nucleus, which thus has a positive charge. Atomic nuclei possess a quantum property known as spin, or intrinsic angular momentum (S). The spin of the proton is associated with a magnetic moment (μ)

aligned with its spin axis, allowing protons to interact with external magnetic fields and serve as the source of the MRI signal [19]. Equation 2.1 shows the relation between spin and magnetic moment:

$$\mu = \gamma S, \tag{2.1}$$

where γ is called the gyromagnetic ratio. This constant is unique to each specific nucleus or element.

A significant portion of the human body is composed of water, and each water molecule contains hydrogen atoms, which consist of a single proton and one electron. The proton possesses a nuclear magnetic moment due to its intrinsic spin, which allows it to interact with external magnetic fields. Under normal conditions, the orientations of these nuclear magnetic moments are random. However, when an external magnetic field (B_0) is applied, the magnetic moments begin to precess around B_0 at the Larmor frequency, as illustrated in Fig. 2.1. Quantum mechanically, the moments are distributed between two energy states: a lower energy state with a component aligned along B_0, and a higher energy state with a component opposed to B_0 [20, 21]. In both cases, the moments are not strictly pointing along or against B_0, but rather precessing about it at a fixed angle. The population difference between the two states is governed by the Boltzmann distribution, with a slight excess in the lower energy state at body temperature. Although this excess is extremely small, the vast number of protons in the body produces a measurable net magnetization (M_0), which forms the basis of the detectable MRI signal [20]. The angular frequency (ω_0) of this precession depends on the strength of the applied magnetic field and is given by the Larmor equation:

$$\omega_0 = \gamma B_0. \tag{2.2}$$

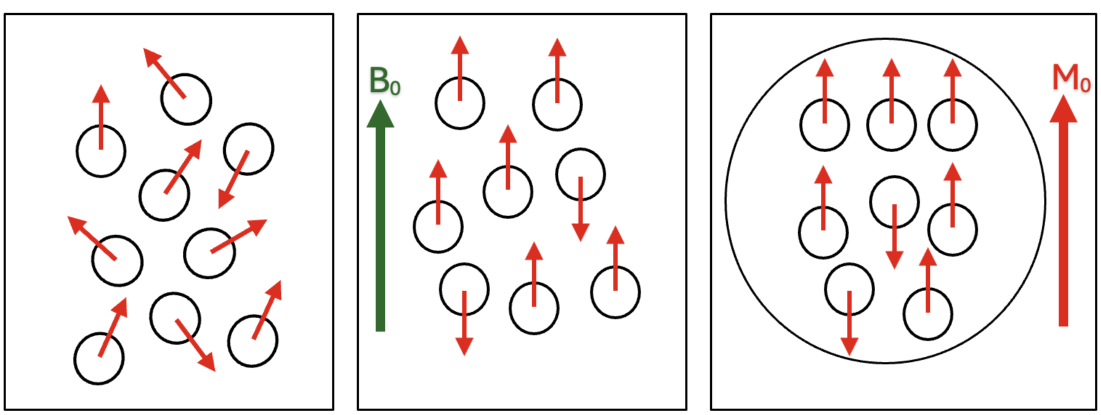

Figure 2.1: Spin alignment of hydrogen atoms placed in an external magnetic field. A) Random orientation with no external magnetic field, B) spin alignment after applying an external magnetic field, and C) the average of the proton magnetic moment as net magnetization.

2.2.1 Radiofrequency(RF) excitation and rotating frame

In MRI, resonance occurs when nuclei interact with an RF magnetic field applied at their Larmor frequency. The RF field, commonly referred to as B_1, is generated by a transmit coil and is oriented perpendicular to the main magnetic field B_0. When the RF frequency matches the Larmor frequency of hydrogen, energy is efficiently transferred to the spins, resulting in coherent excitation [20].

In the presence of only the main magnetic field (B_0), the net magnetization vector aligns along the longitudinal axis, parallel to B_0, as shown in Fig. 2.2(a). When an RF pulse at the Larmor frequency is applied, the magnetization vector begins to tip away from the B_0 direction, as illustrated in Fig. 2.2(b). The angle by which the magnetization is rotated away from the longitudinal axis is called the flip angle, and it increases for as long as the RF pulse is applied (Fig. 2.2(b)–(f)). At any instant, the magnetization can be decomposed into a longitudinal component M_z and a transverse component M_{xy}, as shown in Fig. 2.2(c). The flip angle is determined by both the amplitude and duration of the applied RF pulse. The maximum detectable signal occurs when the magnetization lies entirely in the transverse plane, corresponding to a 90° flip angle (Fig. 2.2(d)), as this produces the largest M_{xy} component. If the RF pulse continues beyond 90°, the magnetization continues to rotate, reaching the $-z$ axis at 180° (Fig. 2.2(g)) and returning toward the $+z$ axis for larger flip angles (Fig. 2.2(h)). The chosen flip angle influences image contrast by controlling the relative contributions of M_z and M_{xy} [20].

It is worth noticing that in the laboratory frame (i.e., the reference frame fixed to the scanner and the main magnetic field B_0), nuclear spins precess about the main magnetic field B_0 at the Larmor frequency, which is very fast, making both the conceptual and mathematical analysis of magnetization dynamics and RF pulse effects complicated. By moving to a rotating frame that rotates at the same frequency and direction, this rapid precession of the magnetization M (and of its individual spin components) around B_0 is effectively removed, and the magnetization appears stationary or slowly varying. In this frame, the B_1 RF field is no longer seen as rotating but instead appears as a static (or slowly varying) effective magnetic field, which makes it much easier to intuitively understand how the magnetization tips, precesses, and relaxes [20, 23]. Thus, the rotating frame is a powerful conceptual tool for simplifying and understanding MRI physics.

2.2.2 Phase behavior of magnetization

Following RF excitation, the net magnetization is rotated into the transverse plane, leading to a detectable MRI signal. In the transverse plane, the magnetization is characterized not only by its

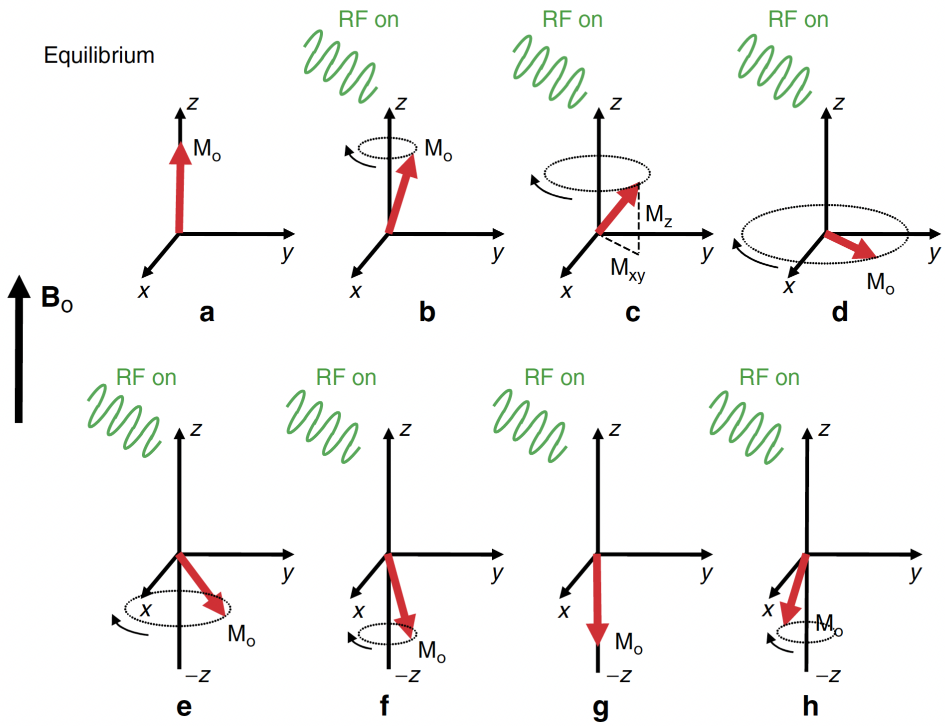

Figure 2.2: Effect of an applied RF pulse on the net magnetization vector M_0. (a) Equilibrium: M_0 aligned along B_0. (b)–(f) Progressive tipping of M_0 as the RF pulse is applied, with the flip angle increasing continuously. (c) Decomposition of M_0 into longitudinal (M_z) and transverse (M_{xy}) components. (d) Maximum M_{xy} at 90° flip angle. (g) M_0 reaches the $-z$-axis at 180°. (h) Further rotation back toward the $+z$-axis beyond 180°. (Image taken from Ref. [22] with permission from Copyright Clearance Center (CCC) under license number 6284910348146.)

magnitude but also by a phase, which describes its angular orientation with respect to a reference axis [24]. This phase is directly imposed by the phase of the applied RF field and plays a fundamental role in MRI signal formation [20]. In the presence of a perfectly homogeneous magnetic field, all spins experience the same magnetic environment and therefore maintain phase coherence over time, resulting in a strong measurable signal in the receive coil. In practice, however, small variations in the local magnetic field cause spins at different spatial locations to precess at slightly different frequencies. As time progresses, these frequency differences lead to dephasing, resulting in a gradual loss of phase coherence among the spins. As phase coherence is reduced, the net transverse magnetization decreases, leading to a corresponding reduction in the observed signal, which takes the form of a free induction decay (FID), a decaying oscillatory signal detected by the receive coil, as illustrated in Fig. 2.3.

Because the accumulated phase of a spin depends sensitively on the magnetic field it experiences, controlled variations in magnetic field strength can be used to impose predictable phase shifts across a sample. The sensitivity of phase to magnetic field variations forms the physical basis of spatial encoding techniques in MRI, which are discussed in later sections of this chapter.

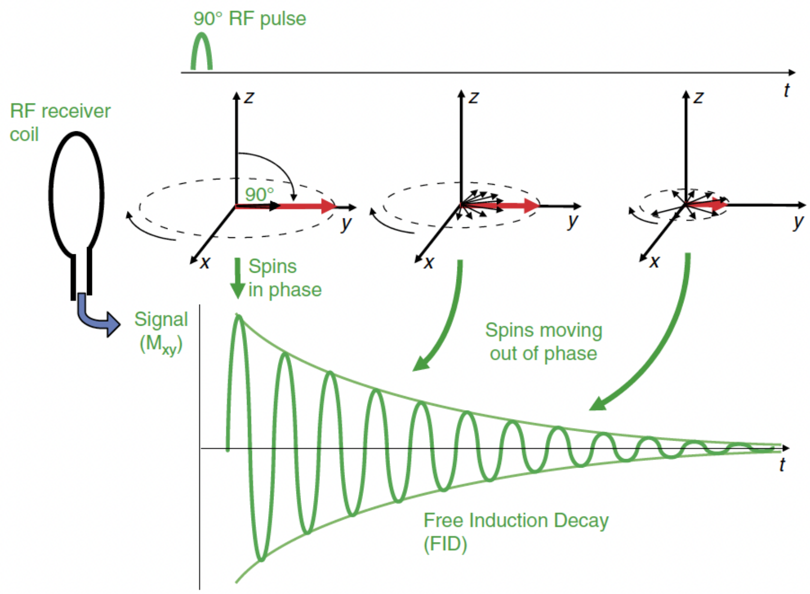

Figure 2.3: Spin dephasing and free induction decay (FID) following a 90° RF excitation pulse. The red arrow represents the net transverse magnetization M_{xy}, which generates a detectable oscillating signal in the RF receive coil. Initially all spins are in phase producing maximum signal amplitude. As the individual spins (black arrows) move out of phase with one another, the signal amplitude decays, producing the FID. (Image taken from Ref. [22] with permission from Copyright Clearance Center (CCC) under license number 6285420013561.)

2.3 Hardware of MRI

In this section, we focus on the essential components of an MRI scanner and their specific functions. All MRI scanners include a main magnet, RF transmit and receive coils, gradient coils, and a shim system. In addition, a computer system controls pulse sequence execution and processes the detected signals to reconstruct the final image. Below, we briefly describe the role of each component as shown in the Fig. 2.4.

2.3.1 Main magnet

The main magnet is the core component of an MRI system and is responsible for generating a strong, static, and highly uniform magnetic field, denoted as B_0. This field aligns the nuclear spins in the

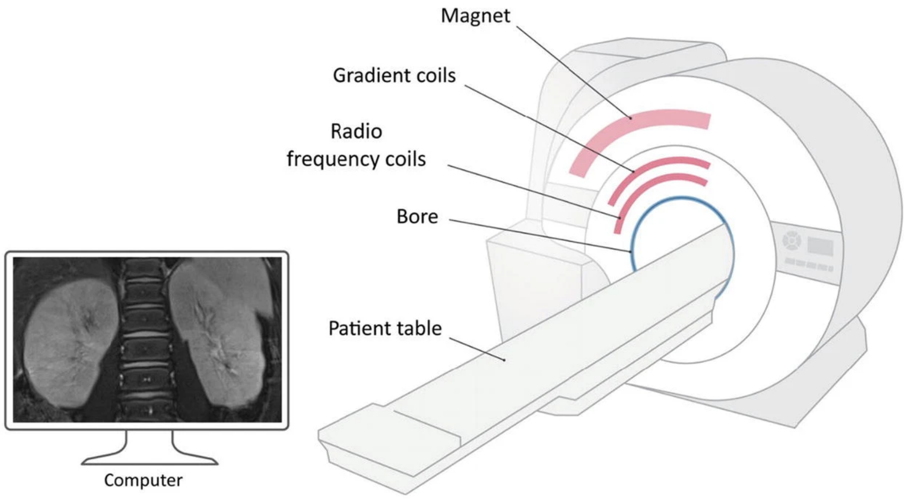

Figure 2.4: Schematic diagram of MRI scanner showing the main magnet, gradient coils, radiofrequency (RF) coils, bore, and patient table. (Image taken from Ref. [25] with permission from Copyright Clearance Center (CCC) under license number 6232640060526.)

human body and establishes the equilibrium net magnetization, forming the physical basis for MRI signal generation. The magnitude of B_0 also determines the Larmor frequency of the nuclear spins.

Based on their design and magnetic-field generation methods, three main types of magnets are used in MRI systems: permanent magnets, superconducting magnets, and resistive electromagnets. Permanent magnets are made from magnetized materials that retain their magnetic properties without requiring an external power supply. These magnets employ large magnetic structures to shape the magnetic field, and they do not require electrical power or cryogenic cooling, making them relatively simple and cost-effective. However, they are limited in the maximum magnetic field strength they can produce and are therefore primarily used in low-field MRI systems.

Superconducting magnets are the most widely used magnets in conventional clinical MRI scanners. They consist of coils made from superconducting materials that carry electrical current without resistance when cooled to cryogenic temperatures. This allows superconducting magnets to generate very strong, stable, and highly homogeneous magnetic fields, which are essential for maintaining phase coherence and image quality. The coils are typically cooled with liquid helium to achieve the required superconducting state [26].

Resistive electromagnets generate magnetic fields by passing an electrical current through conductive coils made of standard non-superconducting materials such as copper. The strength of the magnetic field can be adjusted by varying the current, providing flexibility in field control. However, resistive magnets generate significant heat due to electrical resistance, necessitating extensive cooling and resulting in high power consumption. Resistive magnets are typically limited to lower field strengths compared to superconducting magnets. As a result, their use in MRI systems is limited compared to superconducting magnets.

The static fields generated by the main magnet can pose safety hazards if electronic devices or metallic objects enter the imaging environment. To reduce the risk, most main magnets are shielded to limit the magnetic fields outside the imaging environment. Two principal approaches are used: active shielding and passive (ferromagnetic) shielding. Active shielding is achieved by incorporating an additional coil at a larger radius than the interior coil. The current in the second coil is in the opposite direction, producing an additional magnetic field which opposes the main magnetic field. This approach significantly reduces interior magnetic fields, therefore requiring a higher total current to maintain the desired B_0 field strength. It also significantly reduces stray magnetic fields and simplifies magnet installation without substantially increasing operating costs in superconducting systems. Passive shielding uses ferromagnetic materials to absorb and redirect magnetic fields away from areas where they could cause harm or interference. This can be implemented by incorporating ferromagnetic materials into the scanner room or by integrating them directly into the magnet design. Although effective, passive shielding can result in heavy, complex structures and is less commonly used in modern clinical MRI systems than active shielding.

2.3.2 Shimming system

Shimming refers to the process of correcting residual magnetic field inhomogeneities that remain after the main magnet has been manufactured and brought to its operating field. Due to unavoidable variations in coil winding, mechanical tolerances, thermal contraction at cryogenic temperatures, and environmental influences, the magnetic field produced by the magnet typically deviates from its ideal uniform profile. To achieve the level of field uniformity required for accurate imaging, corrective adjustments must be applied prior to data acquisition. Shimming is performed using either passive methods, which involve strategically placing ferromagnetic materials within the magnet bore, or active methods, which employ dedicated shim coils to generate compensating magnetic fields [20, 27, 28]. These adjustments are applied iteratively until the specified field uniformity is achieved. In practice, active shim coils are typically located in the same region as the gradient coils.

2.3.3 Gradient coils

Gradient coils are responsible for introducing controlled spatial variations in the main magnetic field B_0. While the main magnet generates a strong and uniform static magnetic field along the longitudinal (z) axis, gradient coils superimpose additional magnetic fields that vary approximately linearly with position along the x, y, or z directions.

The gradient system consists of three orthogonal sets of coils, each aligned with one of the Cartesian axes. A typical gradient coil set is shown in Fig. 2.5. Each gradient coil generates a small, position-dependent magnetic field designed to vary approximately linearly across the imaging volume. When superimposed onto the main magnetic field B_0, the resulting total magnetic field becomes spatially dependent, with a slight increase in field strength at one end of the imaging volume and a corresponding decrease at the opposite end.

For example, for a main magnetic field B_0 oriented along the $\hat{z}$ direction, applying a gradient along the x-axis introduces a magnetic field whose z-component varies linearly with position in x. The total magnetic field can then be expressed as

$$B_z(x) = B_0 + G_x x, \tag{2.3}$$

where G_x denotes the gradient strength along the x-axis.

It is worth noting that a strictly linear variation of only a single magnetic field component cannot exist in free space, as all magnetic fields must satisfy Maxwell's equations [20, 29, 30]. In practice, the linear variation of B_z produced by a gradient coil is accompanied by small additional field components in orthogonal directions, often referred to as concomitant gradient fields. However, since gradient fields are typically two to three orders of magnitude smaller than the main field B_0, these additional components produce only minor corrections to the effective field direction, and their primary observable effect is a small modification of the accumulated phase. As the ratio of gradient field strength to the main magnetic field increases at low field, concomitant effects become more pronounced and can introduce measurable phase distortions [31, 32].

Substituting Eq. 2.3 into the Larmor equation yields

$$\omega(x) = \gamma \left(B_0 + G_x x \right). \tag{2.4}$$

This equation shows that the Larmor frequency depends on the spatial position. Spins located in regions of higher magnetic field strength precess at higher frequencies, while those in regions of lower magnetic field strength precess at lower frequencies. This spatial dependence of frequency forms the physical basis for spatial localization in MRI, which will be discussed in subsequent sections.

In addition to frequency variation, gradients also cause spins at different spatial locations to accumulate different phases over time. This position-dependent phase accumulation is fundamental to spatial encoding and image formation, as will be described later. Gradient fields are time-dependent and are rapidly switched during pulse sequences to control spatial encoding. The performance of gradient coils is commonly characterized by their maximum gradient strength and switching rate, which influence achievable spatial resolution and imaging speed. The spatial location at which the applied gradient field is zero is referred to as the isocenter. At this point, the magnetic field strength remains equal to the original B_0 field.

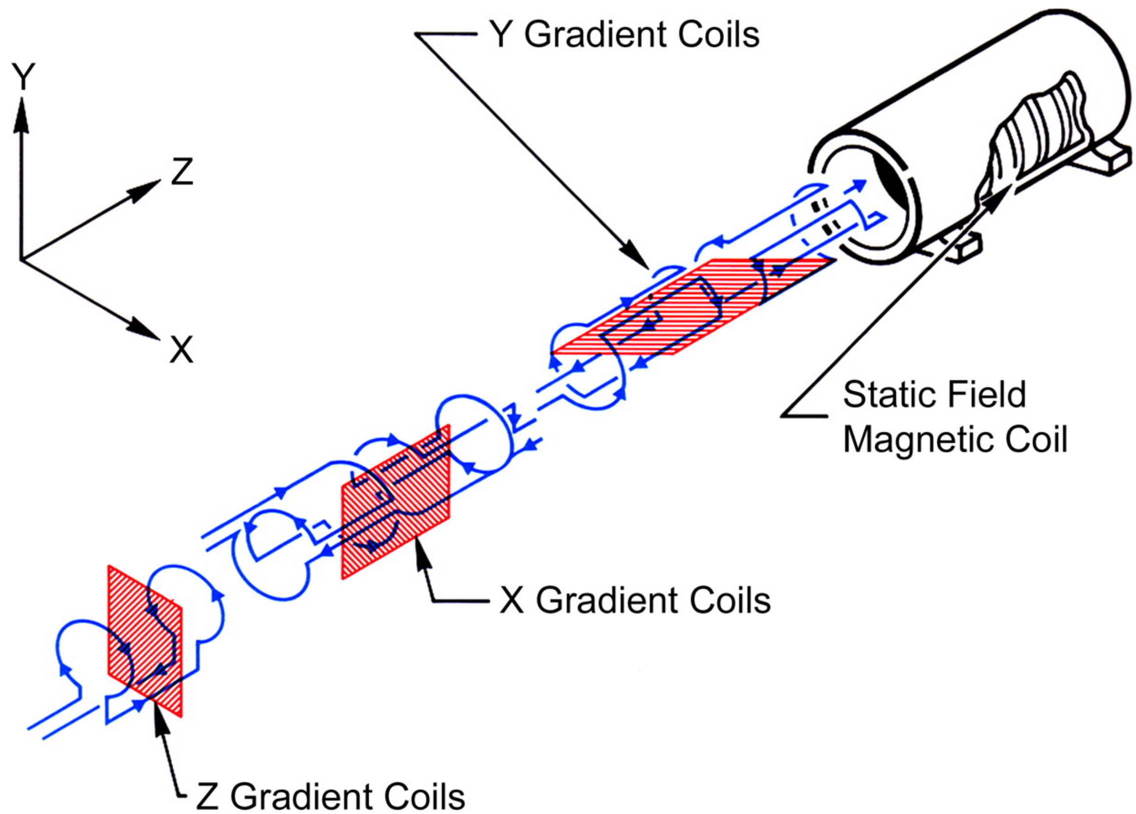

Figure 2.5: Representative gradient coil configuration for MR signal localization. Three x-, y-, and z-gradient coils produce controlled magnetic field gradients that enable three-dimensional image formation. The red planes indicate surfaces of constant total magnetic field resulting from the superposition of the applied gradient field and the main field B_0. (Image taken from Ref. [33] with permission from the Radiological Society of North America (RSNA) under license number 1706421-1.)

2.3.4 RF coils

RF coils constitute an essential component of the MRI system and are used for two primary purposes: spin excitation and signal detection. The RF coil, which is responsible for exciting the spin magnetization by generating an oscillating magnetic field that is oriented perpendicular to the main magnetic field B_0, is called the transmit RF coil. Unlike the static B_0 field, this time-dependent field, commonly denoted as B_1, operates at the Larmor frequency. As described previously, the interaction of the B_1 field with the nuclear spins produces resonance and rotates the net magnetization away from the longitudinal axis.

The second type of RF coil is the receiver coil, which detects the time-varying magnetization due to the excited spins precessing around B_0. Via Faraday's Law, then, the precessing magnetization induces a voltage in the receiver coil that can be measured and recorded. The detected signal depends on both the magnitude of the transverse magnetization and the sensitivity profile of the receive coil.

RF coils are generally classified into surface coils and volume coils. Surface coils are placed close to the region of interest and provide high sensitivity over a limited spatial extent, making them particularly suitable for signal reception. Volume coils, in contrast, are designed to produce a more homogeneous B_1 field over a larger imaging region and are commonly used for transmission [20, 26, 33, 34]. Fig. 2.6 illustrates the orientation of the transmit and receive coils and the perpendicular relationship between the main magnetic field B_0 and the RF magnetic field B_1 during excitation and signal detection.

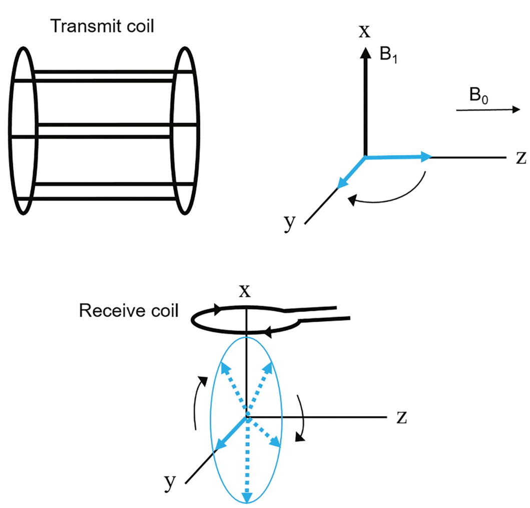

Figure 2.6: The B_1 magnetic field generated by the RF transmit coil flips magnetization from longitudinal orientation to the transverse one. The transverse magnetization precesses, inducing a signal that is detected by the receive coil. (Image taken from Ref. [35] with permission from Copyright Clearance Center (CCC) under license number 1699885-1.)

2.4 MRI physics

As previously defined, magnetization (M) can be regarded as the vector sum of the magnetic moments of all protons in the system. The equation of motion for a single proton in a magnetic field is expressed as [20]

$$\frac{d\vec{\mu}}{dt} = \gamma\vec{\mu} \times \vec{B}, \tag{2.5}$$

where $\vec{\mu}$ is the magnetic moment, γ is the gyromagnetic ratio, and $\vec{B}$ is the applied magnetic field. By extending this relation to the bulk magnetization of all protons, the equation becomes

$$\frac{d\vec{M}}{dt} = \gamma\vec{M} \times \vec{B}_{\text{ext}}, \tag{2.6}$$

where $\vec{M}$ denotes the net magnetization vector and $\vec{B}_{\text{ext}}$ is the external magnetic field. For the case of a static magnetic field applied along the z-axis, i.e., $\vec{B}_{\text{ext}} = B_0\,\hat{z}$, the magnetization components satisfy

$$\frac{dM_z}{dt} = 0, \tag{2.7}$$

and

$$\frac{d\vec{M}_\perp}{dt} = \gamma\vec{M}_\perp \times \vec{B}_{\text{ext}}, \tag{2.8}$$

where M_z is the longitudinal component and $\vec{M}_\perp$ is the transverse component of magnetization. It is important to note that in Eqs. 2.7 and 2.8, relaxation and other interactions of protons with their surroundings (such as spin–lattice or spin–spin interactions) are not considered.

2.4.1 Relaxation time

The concept of relaxation is fundamental in MRI because it directly influences image contrast, which is the ability to distinguish between structures in an image. The intrinsic properties of different tissues in the body, including proton density and the relaxation times of their hydrogen nuclei, determine the brightness in an MRI image following an RF pulse [20]. When a subject is placed inside the MRI scanner, the hydrogen nuclei align with the external magnetic field. An RF pulse from the RF transmit coil at the Larmor frequency perturbs the equilibrium magnetization. This RF energy excites the nuclei and tips away from the longitudinal direction, as demonstrated in Fig. 2.7.

Relaxation is the process by which the perturbed nuclear magnetization returns to equilibrium. During this return, the precessing transverse magnetization produces a time-varying magnetic flux that induces a voltage in the RF receive coil; the amplitude and temporal evolution of this signal determine the brightness of the corresponding tissue in the reconstructed image. In MRI, two primary types of relaxation are distinguished:

- **Spin–lattice relaxation (T_1 recovery):** The process by which nuclei transfer energy to their surrounding lattice (environment), defined as the recovery of longitudinal magnetization toward its equilibrium value M_0.
- **Spin–spin relaxation (T_2 decay):** The process by which nuclei interact and exchange energy with other nearby spins. This interaction causes loss of phase coherence (dephasing), leading to a reduction in transverse magnetization.

When these two relaxation processes are included, Eqs. (2.7) and (2.8) are modified as follows [20]:

$$\frac{dM_z}{dt} = \frac{1}{T_1}\left(M_0 - M_z\right) \tag{2.9}$$

$$\frac{d\vec{M}_\perp}{dt} = \gamma\,\vec{M}_\perp \times \vec{B}_{\text{ext}} - \frac{1}{T_2}\,\vec{M}_\perp \tag{2.10}$$

Beyond T_2 dephasing, static inhomogeneities in the external field cause additional loss of transverse coherence, commonly parameterized by T_2'. The dephasing associated with T_2' is reversible, whereas true T_2 relaxation is irreversible [20]. The combined effect of these mechanisms is described by the overall transverse relaxation time T_2^* [36, 37]:

$$\frac{1}{T_2^*} = \frac{1}{T_2} + \frac{1}{T_2'}. \tag{2.11}$$

The behavior described by Eqs. (2.9)–(2.10) and the combined transverse relaxation expressed in Eq. 2.11 are illustrated schematically in Fig. 2.7, which summarizes the evolution of longitudinal and transverse magnetization during the relaxation process.

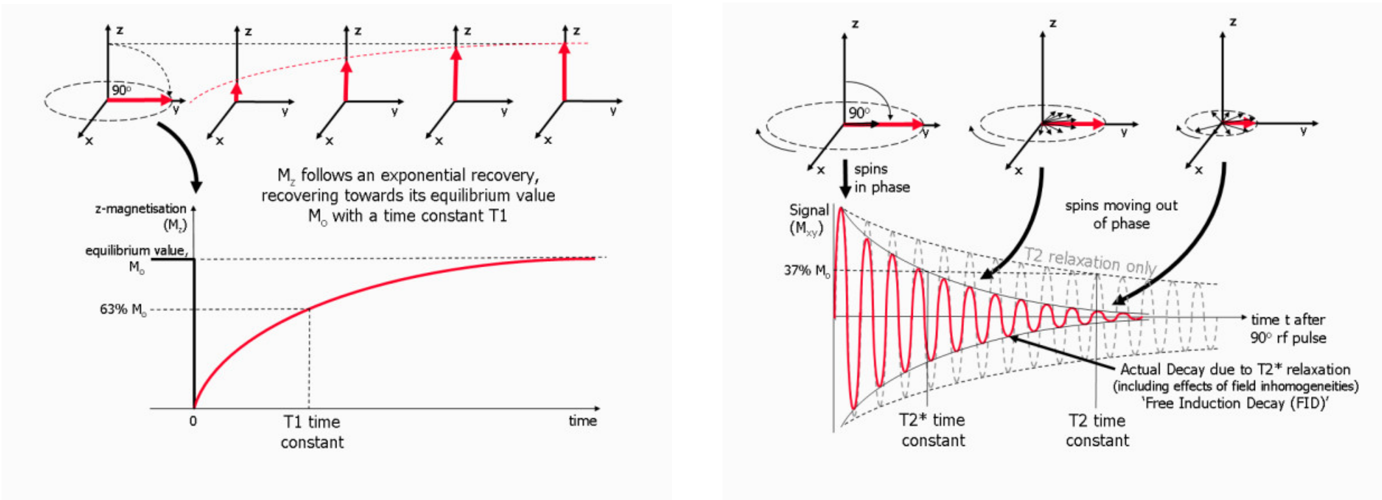

Figure 2.7: Relaxation mechanisms in MRI. **Left:** Longitudinal relaxation (T_1). After a 90° RF excitation, the z-magnetization M_z recovers exponentially toward its equilibrium value M_0 with time constant T_1. **Right:** Transverse relaxation and free-induction decay. Spins progressively dephase, reducing the transverse magnetization M_{xy}. The solid envelope depicts true T_2 (spin–spin) decay, while the faster dashed envelope illustrates T_2^* decay, which includes additional dephasing from B_0 inhomogeneities ($T_2^* < T_2$). (Image taken from Ref. [38], licensed under CC-BY.)

2.4.2 Bloch equation

The combined effects of magnetic precession and relaxation can be described by the Bloch equations, originally introduced by Felix Bloch to model the dynamics of nuclear magnetization under applied magnetic fields [13, 39]. The general form of the Bloch equation can be written as a combination of Eqs. (2.9) and (2.10)

$$\frac{d\vec{M}}{dt} = \gamma\,\vec{M} \times \vec{B} + \frac{1}{T_1}(M_0 - M_z)\hat{z} - \frac{1}{T_2}\vec{M}_\perp \tag{2.12}$$

For simplicity, three components of the Bloch equation are usually written as

$$\begin{aligned} \frac{dM_x}{dt} &= M_y\omega_0 - \frac{M_x}{T_2}, \\ \frac{dM_y}{dt} &= -M_x\omega_0 - \frac{M_y}{T_2}, \\ \frac{dM_z}{dt} &= \frac{M_0 - M_z}{T_1}. \end{aligned} \tag{2.13}$$

where $\omega_0 = \gamma B_0$. The analytical solutions of these equations are:

$$M_x(t) = e^{-t/T_2}\big(M_x(0)\cos(\omega_0 t) + M_y(0)\sin(\omega_0 t)\big) \tag{2.14}$$

$$M_y(t) = e^{-t/T_2}\big(M_y(0)\cos(\omega_0 t) - M_x(0)\sin(\omega_0 t)\big) \tag{2.15}$$

$$M_z(t) = M_z(0)e^{-t/T_1} + M_0\big(1 - e^{-t/T_1}\big) \tag{2.16}$$

For simplicity, these solutions assume a uniform magnetic field oriented in the z-direction, i.e. $\vec{B} = B_0\hat{z}$.

2.5 Spatial encoding

To understand how variations in spin magnetization give rise to a reconstructed image, it is essential to examine how magnetic field gradients influence the MR signal and how the concept of spatial encoding emerges. As discussed in previous sections, magnetic field gradients represent linear spatial variations of the main magnetic field. In the presence of a linear gradient $\mathbf{G} = G_x\hat{x} + G_y\hat{y} + G_z\hat{z}$, the total magnetic field becomes

$$B(\mathbf{r}) = B_0 + \mathbf{G}\cdot\mathbf{r}, \tag{2.17}$$

and the Larmor frequency becomes position-dependent:

$$\omega(\mathbf{r}) = \gamma B(\mathbf{r}) = \gamma\left(B_0 + \mathbf{G}\cdot\mathbf{r}\right), \tag{2.18}$$

where γ is the gyromagnetic ratio and $\mathbf{r} = x\hat{x} + y\hat{y} + z\hat{z}$ denotes spatial position. Thus, spatial location is encoded through controlled variations in frequency and phase.

Magnetic field gradients are applied along all three orthogonal directions, x, y, and z, each generated by a dedicated gradient coil within the MRI system. The primary objective of these gradient coils is to make a spatial variation of the detected signal within the body, a process referred to as spatial localization.

The three most commonly employed encoding mechanisms are the following:

- **Slice Selection (z-direction):** A gradient G_z is applied simultaneously with the RF excitation pulse so that only spins within a specific frequency bandwidth are excited. The slice thickness is given by

  $$\Delta z = \frac{\Delta\omega}{\gamma G_z}, \tag{2.19}$$

  where $\Delta\omega$ is the RF pulse bandwidth.

- **Frequency encoding (x-direction):** The frequency-encoding gradient, denoted as G_x and commonly referred to as the readout gradient, is applied perpendicular to the slice-selection gradient. It is activated during the signal acquisition period.

  In the presence of G_x, the magnetic field varies linearly along the x-direction, resulting in spins located at different positions along the x-axis precessing at different frequencies. The detected MR signal, therefore, contains a spectrum of frequencies that directly correspond to spatial locations along the frequency-encoding direction. By sampling this signal in time while the gradient is active, spatial information along the x-axis can be extracted.

- **Phase encoding (y-direction):** The phase-encoding gradient, denoted as G_y, is applied after slice selection and before signal acquisition along the axis perpendicular to both the slice-selection and frequency-encoding directions. When activated for a short duration, it introduces a linear variation in the magnetic field, causing spins at different spatial positions to precess at slightly different frequencies and accumulate position-dependent phase shifts. After the gradient is switched off, these frequency differences vanish, but the induced phase differences remain encoded in the transverse magnetization. This process is referred to as phase encoding, and the applied gradient direction defines the phase-encoding direction.

2.6 K-space and image reconstruction

The spatial encoding mechanisms described above introduce position-dependent frequency and phase variations into the MR signal. The measured signal therefore contains spatial information that must be systematically organized in order to reconstruct an image. This organization is performed in the spatial frequency domain, commonly referred to as *k-space* [20, 40].

In the presence of time-dependent gradients, the accumulated phase of spins at position $\mathbf{r}$ can be written as

$$\phi(\mathbf{r}, t) = -\gamma \int_0^t \mathbf{G}(\tau) \cdot \mathbf{r} \, d\tau. \tag{2.20}$$

Defining the k-space trajectory as

$$\mathbf{k}(t) = \frac{\gamma}{2\pi} \int_0^t \mathbf{G}(\tau) \, d\tau, \tag{2.21}$$

the phase expression becomes

$$\phi(\mathbf{r}, t) = 2\pi \mathbf{k}(t) \cdot \mathbf{r}. \tag{2.22}$$

The received MR signal can therefore be expressed as

$$s(t) = \int \rho(\mathbf{r}) e^{-i2\pi \mathbf{k}(t)\cdot\mathbf{r}} \, d\mathbf{r}, \tag{2.23}$$

where $\rho(\mathbf{r})$ represents the spin density distribution.

This equation demonstrates that the acquired signal corresponds to samples of the Fourier transform of the object in k-space. In conventional Cartesian imaging, the phase-encoding gradient determines discrete positions along the k_y direction, while the frequency-encoding gradient produces continuous traversal along k_x during signal acquisition. Each repetition of the sequence fills one line of k-space as illustrated in Fig. 2.8. In order to acquire sufficient spatial information for image reconstruction, the pulse sequence must be repeated multiple times. In Cartesian imaging, this is achieved by incrementally varying the amplitude of the phase-encoding gradient G_y at each repetition. Increasing the phase-encoding gradient amplitude produces different amounts of phase accumulation across the object, thereby sampling distinct spatial frequency components.

The time interval between successive repetitions is defined as the repetition time (TR). Furthermore, each sampled point of the MR echo signal corresponds to a unique location in spatial frequency space, or k-space. By systematically sampling these points over multiple repetitions, a complete k-space dataset is formed, from which the final image is reconstructed via inverse Fourier transformation.

In practice, the k-space data are acquired in the form of an echo rather than directly from the initial free induction decay (FID). Due to magnetic field inhomogeneities and applied gradients, the transverse magnetization rapidly dephases. To generate a measurable signal maximum at the center of k-space, rephasing techniques are employed [38].

In spin echo (SE) sequences, a 180° RF pulse reverses the accumulated phase dispersion, producing an echo primarily governed by T_2 relaxation. In contrast, gradient echo (GRE) sequences achieve rephasing by reversing the polarity of the frequency-encoding gradient without the use of a 180° pulse. While SE sequences are less sensitive to field inhomogeneities, GRE sequences allow faster acquisition but exhibit T_2^*-weighted contrast.

Once k-space is completely sampled, the final image is reconstructed by applying the inverse Fourier transform

$$\rho(\mathbf{r}) = \int s(\mathbf{k}) e^{i2\pi \mathbf{k}\cdot\mathbf{r}} \, d\mathbf{k}. \tag{2.24}$$

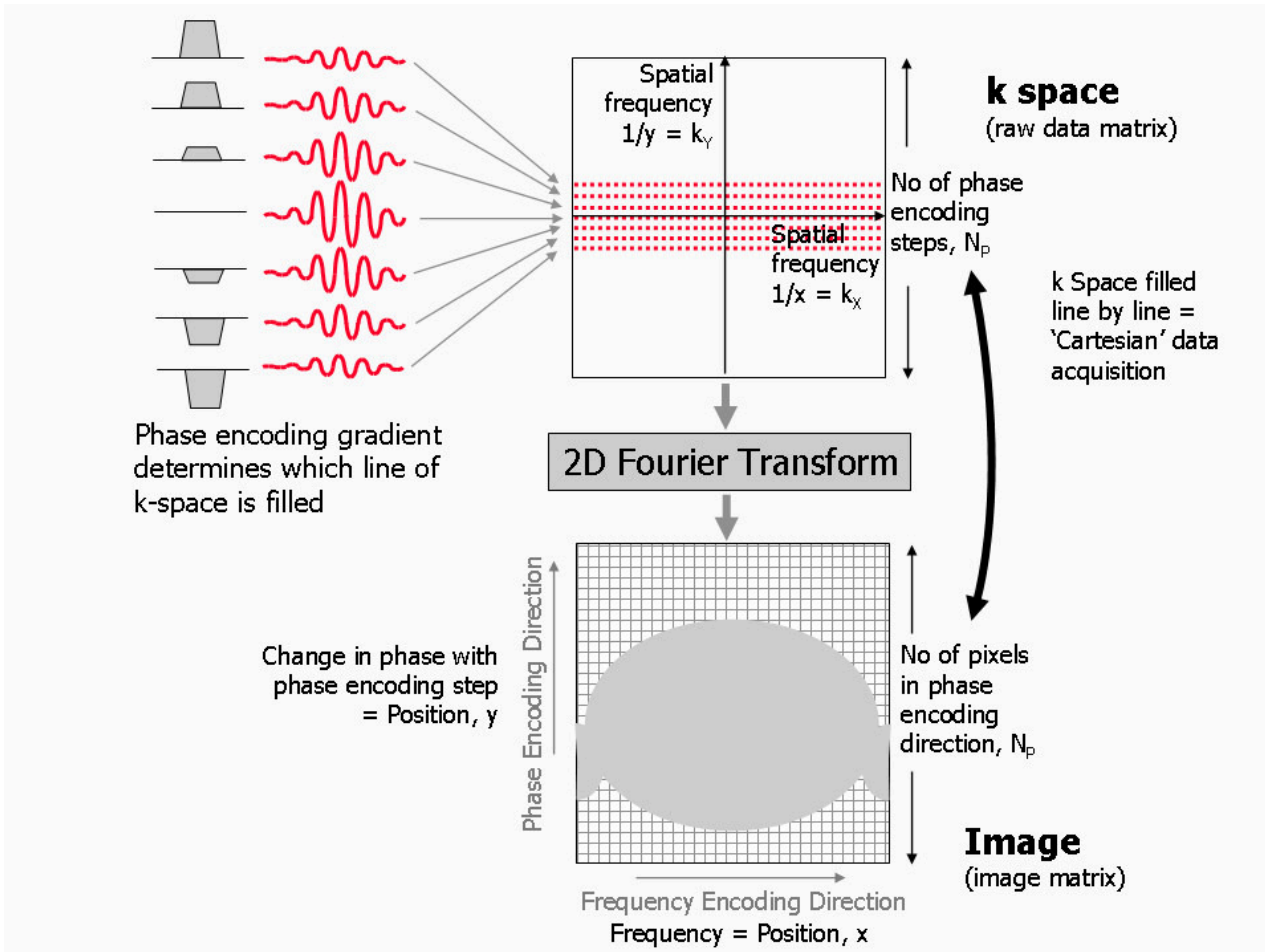

Figure 2.8: In Cartesian imaging, the MR signals acquired at successive phase-encoding steps are organized into a two-dimensional raw data matrix known as k-space. Each repetition of the sequence fills one line of k-space, with traversal along the k_x direction during frequency encoding and discrete positioning along k_y determined by the phase-encoding gradient amplitude. The coordinates of k-space correspond to spatial frequencies (k_x, k_y), where k_x is associated with frequency encoding and k_y with phase encoding. A two-dimensional Fourier transform of k-space yields the reconstructed spatial image, with the number of phase-encoding steps determining the image resolution along the phase-encoding direction. (Image taken from Ref. [38], licensed under CC-BY.)

2.7 Low-field MRI

Historically, the earliest clinical MRI systems operated at static magnetic field strengths in the range of approximately 0.05–0.35 T [41], which are now classified as low-field systems. With continued advances in magnet technology and RF hardware, higher field strengths became dominant in clinical practice due to their improved intrinsic signal-to-noise ratio (SNR). Ultra-high-field systems further extend these gains but introduce additional technical complexity. The classification of MRI field strengths is shown in the Table. 2.2. In recent years, growing interest in low-field MRI has emerged, driven by advances in magnet design, RF coil engineering, and reconstruction methods [7, 8].

Classification	Magnetic field strength
Ultra Low Field (ULF)	≤ 0.01 T
Very Low Field (VLF)	0.01 mT – 0.1 T
Low Field	0.1 T – 0.3 T
High Field	1 T – 3 T
Very High Field (VHF)	3 T – 7 T
Ultra High Field (UHF)	> 7 T

Table 2.2: MRI field classification. The table was modified from Ref. [7].

Low-field systems frequently employ permanent-magnet architectures, including Halbach arrays and other compact magnet configurations, to generate static magnetic fields without cryogenic cooling. Such designs enable compact and energy-efficient scanners suitable for portable or point-of-care applications. Unlike superconducting magnets, permanent magnet systems may exhibit greater intrinsic field inhomogeneity, requiring advanced shimming strategies and tailored pulse sequences to achieve acceptable image quality [42, 43]. Recent work has demonstrated that improvements in magnet design, shimming techniques, and reconstruction algorithms can substantially mitigate these limitations [44, 45, 46, 47].

The constraints imposed by compact and power-limited systems also affect spatial encoding strategies. Conventional MRI relies on rapidly switched B_0 gradient coils for slice selection, frequency encoding, and phase encoding. In portable and low-field platforms, gradient strength, switching rate, and power consumption are often limited by size and hardware simplicity. Furthermore, when the main magnetic field strength is reduced, non-ideal gradient effects and concomitant field contributions can become more significant relative to B_0, potentially influencing phase accumulation and image quality [29].

Overall, these developments reflect a broader shift toward alternative spatial encoding strategies that reduce or eliminate reliance on conventional linear magnetic field gradients superimposed on B_0 [48, 49, 50, 51]. These approaches aim to reduce hardware complexity, decrease power requirements, and mitigate acoustic noise from rapidly switched gradient coils. In particular, methods that exploit spatially varying phase gradients of the RF transmit field (B_1) offer a pathway to controlled spatial encoding without conventional gradient hardware. Transmit array spatial encoding (TRASE) MRI is one such strategy and is discussed in detail in the following chapter.

Chapter 3

Transmit Array Spatial Encoding (TRASE)

3.1 The TRASE concept

Conventional MRI achieves spatial encoding by applying time-varying linear gradients to the static magnetic field B_0, thereby generating controlled spatially dependent phase evolution. However, spatial encoding can also be achieved using other mechanisms that do not rely on gradients of the static magnetic field. In particular, radiofrequency (RF) fields can be used to introduce position-dependent excitation or phase shifts. These approaches represent three different spatial encoding mechanisms in MRI: conventional static-field gradients, RF magnitude gradients, and RF phase gradients. A conceptual comparison of these encoding mechanisms is summarized in Table 3.1. In the following discussion, we briefly review two RF-based encoding approaches that illustrate these alternative strategies.

The concept of using the radiofrequency (B_1) field for spatial encoding was first explored by Hoult [52], who demonstrated that spatially varying RF amplitude profiles could generate position-dependent excitation. This approach, referred to as rotating-frame imaging, relies on spatial gradients in the RF magnitude rather than in the static magnetic field. Although limited by practical constraints, it established the principle that RF fields can directly participate in spatial encoding.

A more complete alternative was proposed by Sharp and King in 2010 [9, 10], who introduced TRASE. Rather than employing gradients in B_0, TRASE uses linearly varying directions (or phase gradients) of the radiofrequency (B_1) field to achieve spatial encoding. In this approach, spatial encoding arises from phase manipulations imposed by RF pulses, replacing the phase evolution produced by conventional gradient fields and thereby avoiding the need for static-field gradient coils and their associated hardware challenges, such as acoustic noise. The following sections describe the physical principles and k-space behavior underlying TRASE encoding.

Encoding method	**Gradient type**	**Static field**	**RF field**
Frequency encoding	Main field	$B_0 + xG_x$	B_1
Rotating frame imaging	RF magnitude	B_0	$B_1 + xG_{1x}$
TRASE	RF phase	B_0	$B_1 e^{i\,xG_{1x}}$

Table 3.1: Comparison of three MRI encoding methods. Table reproduced from Ref. [9] with permission from the rights owner (John Wiley and Sons) under license number 1702086-1.

3.2 TRASE B_1 requirements

In TRASE, RF phase gradients are generated using dedicated transmit coils specifically designed to produce uniform B_1 magnitude with approximately linear spatial phase variation across the imaging volume. An RF field that generates a linear phase gradient can be mathematically described as

$$B_1(\mathbf{r}) = |B_1|e^{i\phi_1(\mathbf{r})}, \qquad \phi_1(\mathbf{r}) = 2\pi\mathbf{k}_1 \cdot \mathbf{r} = \mathbf{G}_1 \cdot \mathbf{r} \tag{3.1}$$

where $\phi_1(\mathbf{r})$ is the spatially varying RF phase at position $\mathbf{r}$, and $\mathbf{G}_1 = 2\pi\mathbf{k}_1$ is the RF phase gradient vector. The vector $\mathbf{k}_1$ characterizes the spatial phase variation in the RF field and defines both the direction and magnitude of the phase twist. A non-zero $\mathbf{k}_1$ corresponds to a specific location in three-dimensional k-space, whereas $\mathbf{k}_1 = 0$ represents the k-space origin and corresponds to a uniform RF phase distribution.

An RF phase gradient may be generated either through a dedicated coil geometry that intrinsically produces linear phase variation, or through controlled superposition of fields from multiple driven coil elements [9]. In TRASE, only a single RF phase gradient is required at any given time, and the RF field amplitude does not directly contribute to spatial encoding and is therefore preferably uniform.

From Eq. 3.1, the RF phase-gradient $\mathbf{G}_1$ is related to the spatial frequency vector by $\mathbf{G}_1 = 2\pi\mathbf{k}_1$. Thus, each RF phase gradient corresponds to a unique spatial frequency vector $\mathbf{k}_1 = k_{1x}\hat{x} + k_{1y}\hat{y} + k_{1z}\hat{z}$, which defines the associated point in three-dimensional k-space.

3.3 k-space in TRASE

In TRASE, the concept of k-space is fundamentally equivalent to that in conventional MRI, as it still represents the image's spatial frequency domain. The key distinction lies in how k-space is traversed: while conventional MRI employs gradients of the static magnetic field (B_0) to impart spatially dependent phase shifts, TRASE achieves the same effect through RF phase gradients of the transmit field (B_1) [9, 10]. Despite differences in the physical mechanisms of encoding, the underlying k-space framework and reconstruction principles remain the same.

This process can be understood by considering a spin initially aligned along the longitudinal (z) axis. After applying a 90° RF pulse (known as an excitation pulse) from a phase-gradient coil, the spins are tipped into the transverse plane. The applied RF phase gradient introduces a position-dependent phase in the transverse magnetization, which corresponds to a shift to a specific location $\mathbf{k}_1$ in k-space. The resulting transverse magnetization can therefore be written exactly as given in the following equation:

$$M_{xy} = M_0 e^{i\phi(\mathbf{r})} = M_0 e^{i2\pi\,\mathbf{k}_1\cdot\mathbf{r}} \;, \tag{3.2}$$

where M_{xy} is the transverse magnetization after excitation and M_0 is the initial longitudinal magnetization. As illustrated in Fig. 3.1(a), the applied RF phase gradient defines a coil-specific origin in k-space at $\mathbf{k}_1$.

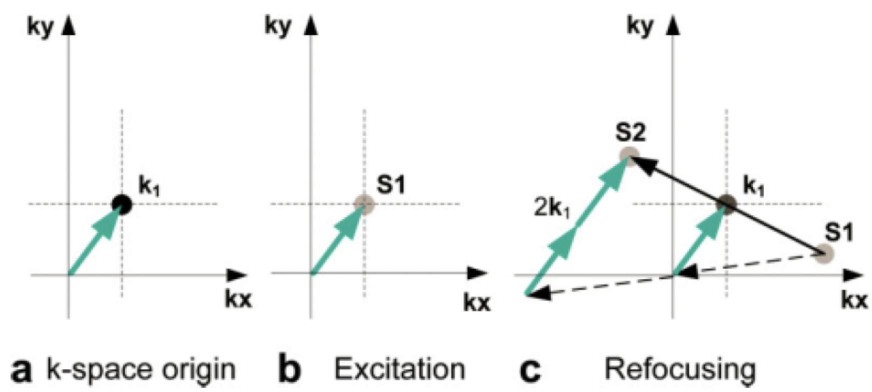

Figure 3.1: Basic k-space behavior in TRASE MRI. (a) An RF phase gradient defines a k-space origin at k_1 ; (b) A 90° excitation pulse directly moves the magnetization to k_1; (c) A 180° refocusing pulse reflects the magnetization about its coil k-space origin, resulting in controlled k-space displacement. (Image taken from Ref. [9] with permission from the rights owner (John Wiley and Sons) under license number 1702086-1.)

In contrast to conventional MRI, where spatial encoding occurs during the application of magnetic field gradients, in TRASE the excitation pulse itself directly establishes a point in k-space determined by the RF phase gradient. This direct positioning of the magnetization at $\mathbf{k}_1$ is depicted in Fig. 3.1(b). By using an ordinary receiver coil with uniform phase, we can observe this spatial encoding.

It is important to note that if the same phase-gradient coil is used for both transmission and reception, the spatial phase variation may not be observable in the detected signal. This occurs because the receive coil imposes an opposite k-space shift ($-k_1$) on the induced voltage signal, which cancels the transmit and receive phase gradients, even though spatial encoding has occurred.

A 180° RF refocusing pulse rotates the transverse magnetization about the phase of the applied RF field ($\phi(\mathbf{r})$). When the RF phase varies spatially, this reflection becomes position-dependent. As shown in Fig. 3.1(c), the magnetization undergoes a reflection about the coil-specific k-space origin. As a result, the transverse magnetization after refocusing can be expressed as

$$M_{xy}^{+} = M_{xy}^{-*}\, e^{i2\phi(r)} = M_{xy}^{-*}\, e^{i2\pi(2\mathbf{k}_1\cdot\mathbf{r})}\ , \tag{3.3}$$

where M_{xy}^{-} is initial transverse magnetization, M_{xy}^{-*} is complex conjugate of M_{xy}^{-}, and M_{xy}^{+} is transverse magnetization after adding refocusing pulse.

It is worth noting that applying a phase-gradient RF pulse for refocusing has two effects: first, it reverses the sign of k ($k \to -k$), as in conventional MRI, and second, it introduces an additional position-dependent phase shift equal to $2k_1$, as shown in the exponential term of Eq. 3.3, along the encoding direction. This can be written as

$$k_{+} = -k_{-} + 2k_1, \tag{3.4}$$

where k_{-} is the k-space position before refocusing, k_{+} is the k-space position after refocusing pulse, and k_1 is the coil k-space origin. We can rewrite Eq. 3.4 as

$$k_{+} - k_1 = -(k_{-} - k_1), \tag{3.5}$$

which in this form clearly shows that k-space undergoes a reflection about k_1, the coil's k-space origin. An important consequence is that if the same phase gradient is used for both excitation and refocusing ($k_{-} = k_1$), no spatial encoding occurs, as the trajectory collapses to ($k_{+} = k_1$). To avoid this, distinct phase gradients must be applied, meaning the excitation and refocusing pulses must be delivered by coils with different k-space origins. When the excitation coil has k-space origin $\mathbf{k}_{1A}$ and the refocusing coil has k-space origin $\mathbf{k}_{1B} \neq \mathbf{k}_{1A}$, the refocusing pulse shifts the k-space position by $2(\mathbf{k}_{1B} - \mathbf{k}_{1A})$, resulting in a net k-space displacement. The refocusing pulse, therefore, plays a crucial role in TRASE, enabling controlled traversal of k-space along a defined trajectory.

A sequence of these refocusing pulses forms an echo train which, unlike in conventional MRI, does not produce continuous phase evolution in TRASE; instead, the phase evolution occurs discretely at each refocusing pulse. So, TRASE requires echo train pulse sequences with alternating 180° pulses applied to a system of RF coils, as shown in Fig. 3.2(a). To achieve spatial encoding along a chosen axis, it is necessary to apply two RF fields for each encoding direction [10, 53], as the effective k-space step size is determined by the difference between successive RF phase gradients. The resulting discrete k-space pattern is illustrated in Fig. 3.2(b), where each echo corresponds to a distinct spatial frequency location determined by the coil phase origins k_{1A} and k_{1B}. As a result, multiple RF coils with phase-gradients along different axes are necessary to obtain spatial information about a sample.

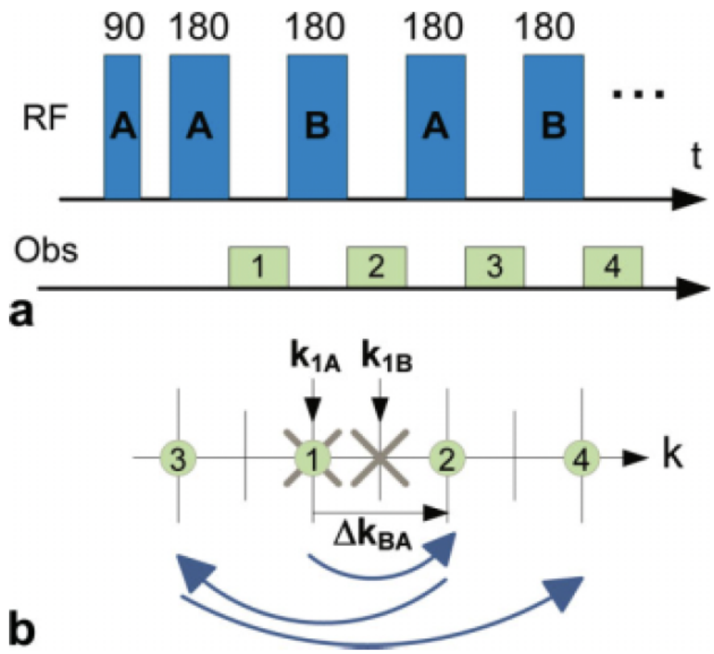

Figure 3.2: 1D TRASE phase gradient imaging. (a) Pulse sequence with a 90° excitation followed by alternating 180° refocusing pulses from coils A and B, with signals (1–4) recorded after each pulse. (b) Corresponding k-space positions determined by the difference between coil phase origins k_{1A} and k_{1B}. Each echo is related to a distinct k-space location defined by the applied RF phase gradients. (Image taken from Ref. [9] with permission from the rights owner (John Wiley and Sons) under license number 1702086-1.)

3.3.1 2D TRASE encoding

The one-dimensional TRASE mechanism described previously can be extended to two-dimensional imaging by using multiple RF phase-gradient coils with different spatial orientations. In TRASE, each RF phase gradient defines a specific k-space origin, denoted by its vector $\mathbf{k}_1$. When two coils produce phase gradients in different spatial directions (for example, along x and y), the difference between their k-space origins defines an encoding direction. In other words, the effective k-space step is determined by the vector difference between two coil origins.

For two-dimensional imaging, at least three non-collinear RF phase gradients are required. If we denote three coils by A, B, and C, with corresponding k-space origins $\mathbf{k}_A$, $\mathbf{k}_B$, and $\mathbf{k}_C$, then the effective encoding directions are given by

$$2(\mathbf{k}_B - \mathbf{k}_A), \qquad 2(\mathbf{k}_C - \mathbf{k}_A), \qquad 2(\mathbf{k}_C - \mathbf{k}_B). \tag{3.6}$$

These vectors define a two-dimensional region in k-space as shown in Fig. 3.3(a).

Two-dimensional k-space is traversed by applying a sequence of echo trains composed of excitation and refocusing pulses from different RF phase-gradient coils. The initial 90° excitation pulse establishes a starting point in k-space corresponding to the selected RF phase gradient. Subsequent 180° refocusing pulses, applied alternately from different coils, produce discrete reflections in k-space about their respective coil-specific k-space origins.

As shown previously, each refocusing pulse shifts the k-space position according to the relation

$$\mathbf{k}_+ = -\mathbf{k}_- + 2\mathbf{k}_i,$$

where $\mathbf{k}_i$ represents the k-space origin of the coil used for that pulse. When different coils are used sequentially, the net effect is a stepwise displacement in k-space equal to twice the difference between their k-space origins. In TRASE, k-space evolution does not occur continuously in time; instead, each 180° RF phase-gradient pulse produces a discrete reflection in k-space, resulting in a stepwise displacement determined by the difference between coil k-space origins [9, 10]. In two-dimensional TRASE imaging, spatial encoding is achieved through structured echo trains composed of multiple RF phase-gradient coils. Let N indicate the number of echoes within each echo train, corresponding to the number of discrete k-space steps generated along one encoding direction. Let M represent the total number of echo trains used to produce encoding along the orthogonal direction. Together, these define an $M \times N$ k-space matrix.

Figure 3.3 shows an example of using three RF coils and how the k-space can be traversed in the x and y directions with the help of three RF fields. The notation used in the figure, such as $(AB)_5$ or $(AC)_2$, specifies the number of repeated 180° pulse pairs applied during the echo train. For example, $(AB)_5$ indicates that the pulse sequence alternates between coils A and B five times. Since each AB pair consists of two 180° pulses, this sequence generates ten discrete k-space points. Similarly, $(AC)_2$ denotes two repetitions of the A–C pulse pair, producing successive k-space displacements along the direction defined by coils A and C. In general, the subscript determines the number of discrete k-space steps created in that direction.

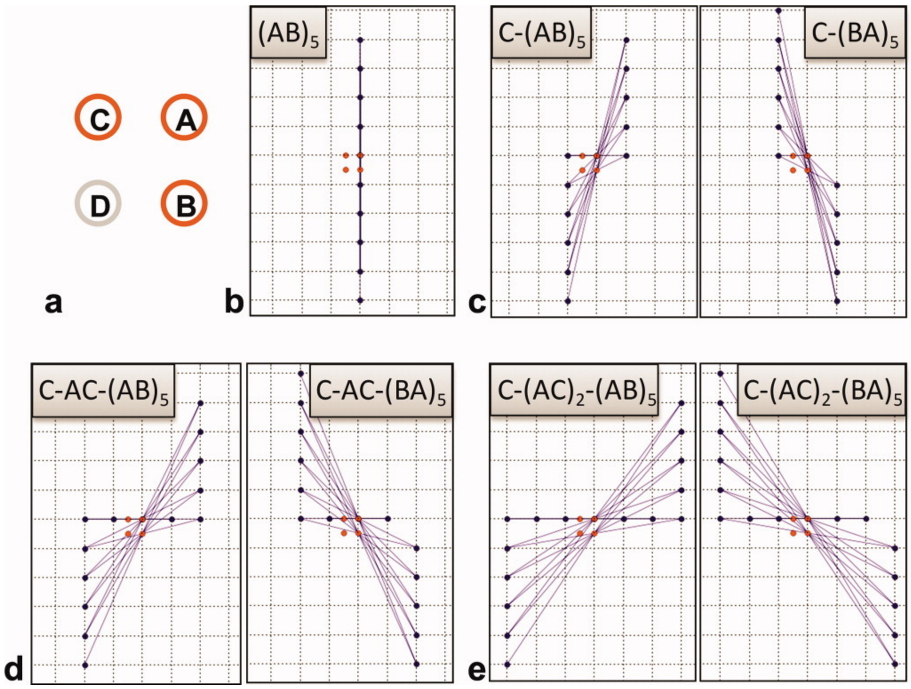

Figure 3.3: Example of 2D k-space traversal in TRASE using three RF phase-gradient coils (A, B, and C). (a) k-space origin of 4 fields corresponding to coils A, B, C, and D, where only coils A, B, and C are active (highlighted). (b) One-dimensional trajectory generated by repeated (AB) pulse pairs. (c)–(e) Progressive displacement of trajectories through additional (AC) repetitions, forming a two-dimensional k-space grid. (Image taken from Ref. [9] with permission from the rights owner (John Wiley and Sons) under license number 1702086-1.)

In all sequences, the initial 90° excitation pulse is transmitted through the coil A. Consequently, immediately after excitation, the transverse magnetization is located at the k-space origin defined by that coil, k_A. When no additional phase-gradient coil is applied prior to the echo train, as in $(AB)_5$ (Fig. 3.3 (b)), the trajectory begins at k_A and produces a single one-dimensional line in k-space.

For two-dimensional encoding, an additional refocusing pulse from coil C is applied before the AB echo train. This pulse shifts the initial position k_A to a new location given by $2k_C - k_A$. The subsequent AB or BA echo train then generates motion along the AB encoding direction, but about this shifted origin. As a result, the trajectory forms a displaced line in k-space, representing the first step toward two-dimensional coverage (Fig. 3.3 (c)).

A complete $M \times N$ k-space matrix can be constructed using a structured set of echo trains. One procedure is to use $M/2$ trains with refocusing pulses of the form

$$C - (AC)^i - (AB)^{N/2},$$

and $M/2$ additional trains with

$$C - (AC)^i - (BA)^{N/2},$$

where $i = 0, 1, \ldots, M/2 - 1$. The index i in $(AC)^i$ indicates the repeated application of the 180° pulse pair A–C, which progressively shifts the trajectory in the second encoding direction. The alternating (AB) and (BA) blocks generate symmetric k-space motion along the first encoding direction. By varying i, successive echo trains are displaced in the orthogonal direction, thereby filling a two-dimensional region of k-space. In Fig. 3.3(d)–(e), increasing the number of (AC) pulse pairs displaces the trajectories and fills the two-dimensional k-space region.

3.3.2 The first 2D imaging in TRASE

Once the desired two-dimensional k-space region has been filled, a standard two-dimensional inverse Fourier transform performs image reconstruction in the same manner as in conventional MRI. Therefore, although the physical mechanism of encoding differs fundamentally from gradient-based imaging, the mathematical framework of k-space and Fourier reconstruction remains unchanged.

The experimental feasibility of two-dimensional TRASE encoding was demonstrated at 0.2 T using an RF phase-gradient array capable of producing phase gradients of approximately 4.1 deg/cm [10]. A direct comparison between conventional B_0 gradient encoding and RF phase-gradient encoding showed nearly identical image appearance at the same nominal spatial resolution. Both methods resolved structural features separated by 3 mm, confirming that RF-based encoding can achieve resolution comparable to that of conventional gradient-based MRI.

To evaluate in-vivo performance, tomographic imaging of the human wrist was performed as shown in Fig. 3.4 (C). Despite the reduced signal-to-noise ratio associated with operation at 0.2 T, the resulting images demonstrated clear anatomical detail, supporting the diagnostic feasibility of the TRASE approach.

3.4 Field of view and pixel size in TRASE

In both conventional MRI and TRASE, the relationship between k-space and image domain is based on the Fourier transform. As a result, the spacing between adjacent k-space data points determines the image field of view (FOV), while the total extent of k-space determines the achievable spatial resolution. Physically, FOV refers to the spatial extent over which the object can be imaged.

Let Δk denote the spacing between sampled points. The field of view is given by

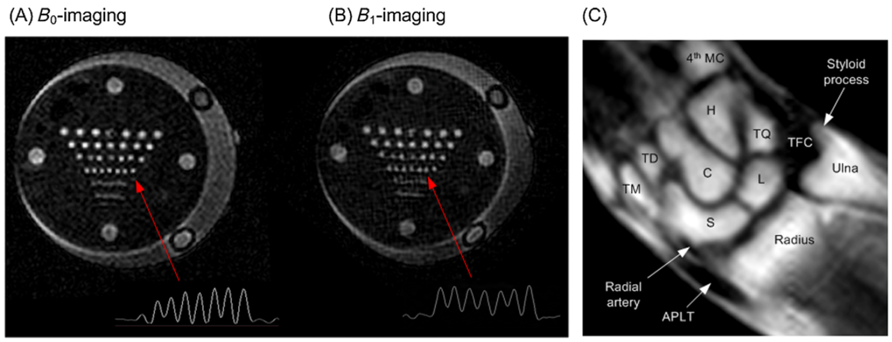

Figure 3.4: The first in-vivo TRASE images. (a) MR image acquired with conventional B0 encoding. (b) MR image acquired with TRASE B1 encoding. (c) Two-dimensional TRASE image of the human wrist. (Image taken from Ref. [10] with permission from the rights owner (John Wiley and Sons) under license number 6231420582545.)

$$\mathrm{FOV} = \frac{1}{\Delta k}. \tag{3.7}$$

Furthermore, since the image is discretized into a finite number of points (N), the following relation also holds:

$$\mathrm{FOV} = N \cdot \Delta\omega, \tag{3.8}$$

where $\Delta\omega$ is image pixel size. The above equation leads to the fundamental relationship between image and k-space parameters:

$$\Delta\omega \cdot \Delta k = \frac{1}{N}. \tag{3.9}$$

In a one-dimensional TRASE sequence using two RF phase-gradient coils A and B, the effective k-space step size is determined by the difference between their phase-gradient vectors:

$$\Delta k = 2(k_B - k_A). \tag{3.10}$$

Therefore, using the general relationship between k-space and the image domain illustrated in Fig. 3.5, the TRASE field of view becomes

$$\mathrm{FOV} = \frac{1}{|2(k_B - k_A)|}. \tag{3.11}$$

Thus, a smaller separation in k-space results in a larger FOV, whereas a larger separation reduces the FOV and may lead to aliasing if the object extends beyond this range [20].

The image pixel size (spatial resolution) $\Delta\omega$, as introduced in Equation. 3.9, is determined by the total k-space range traversed during the echo train. The pixel size may also be expressed as

$$\Delta\omega = \frac{FOV}{N} = \frac{1}{\Delta k \cdot N}. \tag{3.12}$$

In a 1D TRASE sequence, the echo train length (ETL) corresponds to the total number of steps through k-space. If the echo train length is denoted by ETL, then

$$\Delta\omega = \frac{1}{\Delta k \cdot \mathrm{ETL}} = \frac{1}{|2(k_B - k_A)| \cdot \mathrm{ETL}}. \tag{3.13}$$

This expression shows that increasing the echo train length or increasing the phase-gradient difference between the coils improves spatial resolution. In practice, however, signal decay along the echo train (e.g., due to T_2 relaxation) limits the achievable resolution [54].

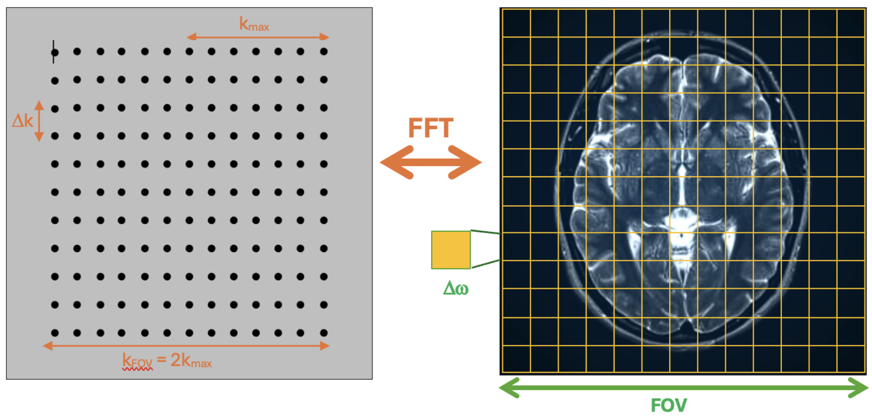

Figure 3.5: Relationship between image field of view (FOV) and pixel size $\Delta\omega$ and the corresponding k-space parameters Δk and k_{FOV} in MRI. This relationship holds for both conventional gradient-based MRI and TRASE MRI, as both methods rely on Fourier-based image reconstruction. (Image adapted from the concept presented in Ref. [55].)

3.5 RF coils in TRASE MRI

The characteristics of the B_1 field produced by the RF coil play a central role in TRASE performance. Consequently, following the introduction of TRASE, several RF coil geometries have been investigated to generate the RF phase gradients required for spatial encoding and to determine the most suitable configuration. In the following, we briefly describe several RF designs as illustrated in Fig. 3.6.

- **Spiral birdcage coil**:

  A modified birdcage coil with a spiral geometry introduces an approximately linear RF phase variation along the main magnetic field (B_0), while preserving a relatively uniform $|B_1|$ magnitude. This was used in the original experimental demonstration of TRASE [9].

- **Helmholtz–Maxwell coil**:

  This configuration combines Helmholtz and Maxwell coil pairs to generate an RF field with approximately uniform magnitude and linear spatial phase variation through controlled superposition of fields. In the first in-vivo TRASE implementation, Sharp et al. [10] used a Helmholtz–Maxwell coil configuration at 0.2 T to perform two-dimensional wrist imaging.

- **Birdcage–Maxwell coil**:

  A transmit array composed of a standard birdcage coil combined with a Maxwell coil was implemented to generate orthogonal cosine and sine B_1 field components, producing a linear B_1 phase gradient for TRASE encoding along the patient axis [56].

- **Twisted Saddle coil**:

  A saddle coil with twisted conductors introduces a controlled spatial variation in RF phase, producing a phase gradient along the coil axis suitable for TRASE encoding [57].

- **Twisted Solenoid coil**:

  A more recent development in TRASE MRI RF coils is the twisted solenoid coil, which evolved from earlier double-helical coil configurations [58, 59, 60, 61]. The twisted solenoid was introduced as an efficient method for producing approximately linear RF phase gradients, particularly in MRI systems with transverse or vertical B_0 magnetic field geometries. Its application to TRASE imaging was first demonstrated by Yong et al. [62] and later implemented by Sun et al. [63].

  Further advancements include the introduction of geometrically decoupled twisted solenoid arrays to improve phase linearity while minimizing mutual inductance between transmit elements [64], as well as truncated coil geometries [65] designed to reduce overall coil length while maintaining phase-gradient strength and field uniformity. Because this coil geometry is used so predominantly now in TRASE, and thus forms the basis of the design investigated in this thesis, its structure will be discussed in greater detail in the following section.

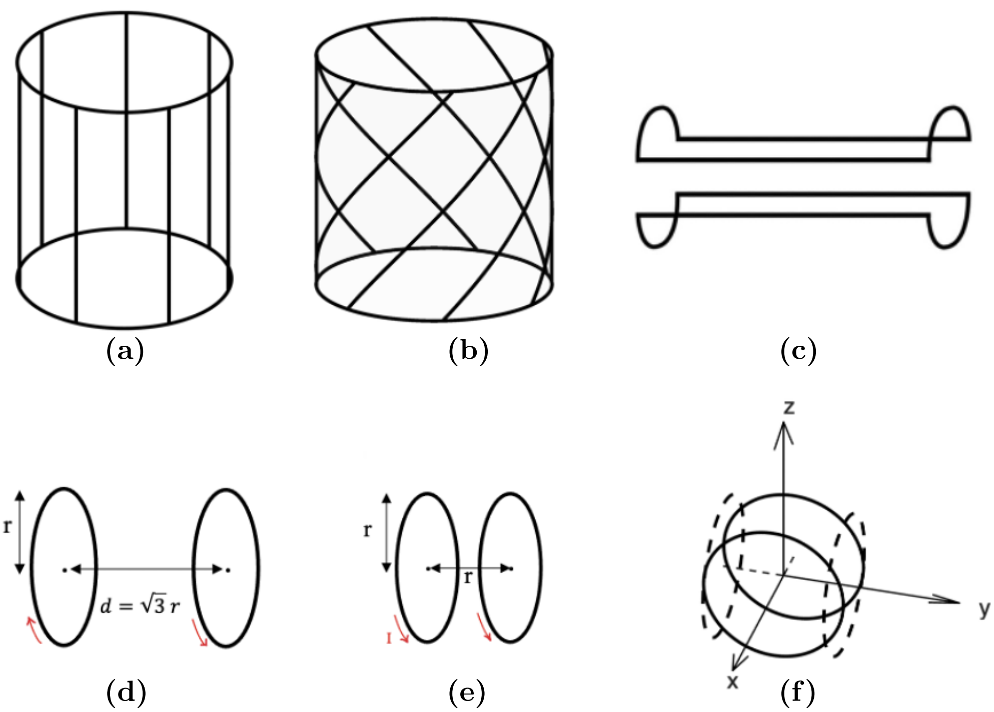

Figure 3.6: Schematic representations of RF coil geometries used to generate RF phase-gradient fields in TRASE MRI: (a) birdcage coil, (b) spiral birdcage coil, (c) saddle coil pair, (d) Maxwell pair, (e) Helmholtz pair, and (f) orthogonal Maxwell–Helmholtz configuration. In this configuration, the dashed loops represent the Maxwell coils, while the solid loops represent the Helmholtz coils. These geometries produce RF phase gradients through different current distributions and field superposition mechanisms.

3.6 Geometry of the Twisted Solenoid

The Cartesian coordinates of the winding pattern at the heart of twisted solenoid designs [63, 64, 65] are given by the parametric curve

$$P(\theta) = \left[a\cos(\theta), a\sin(\theta), A_n \sin(n\theta + \varphi) + \frac{h}{2\pi}\theta\right], \tag{3.14}$$

with each quantity (and its associated SI unit) defined as follows [66] :

- θ (rad) – the azimuthal angle in cylindrical coordinates.
- a (m) – the radius of the cylindrical former on which the coil is wound.
- n – the multipole order of the coil. (For TRASE coils, $n = 2$ [63].)
- A_n (m) – the multipole modulation or twist amplitude. (For a uniform solenoid, $A_n = 0$.)
- φ (rad) – the winding shift.
- h (m) – the coil turn advance. (The coil pitch (turns/m) is $1/h$.)

This curve represents the spatial path of the current-carrying wire wound on the cylinder as shown in the Fig. 3.7. The winding is constrained to the surface of a cylinder of radius a, with its position specified by the azimuthal angle θ. The x and y components therefore describe circular motion around the cylinder, while the z coordinate consists of a linear turn advance combined with a sinusoidal modulation.

One notable finding reported for a twisted solenoid coil is that phase gradients can be generated in different directions by physically rotating the coil [63]. Moreover, it is demonstrated that the required coil rotation can be directly related to the winding shift parameter φ used to define the coil geometry. In particular, a physical rotation of the coil by 90° corresponds to a winding shift of 180°. Accordingly, Table 3.2 presents the configurations required to generate the four orthogonal phase gradients $+G_x$, $-G_x$, $+G_y$, and $-G_y$, together with the corresponding coil rotation angles for each case.

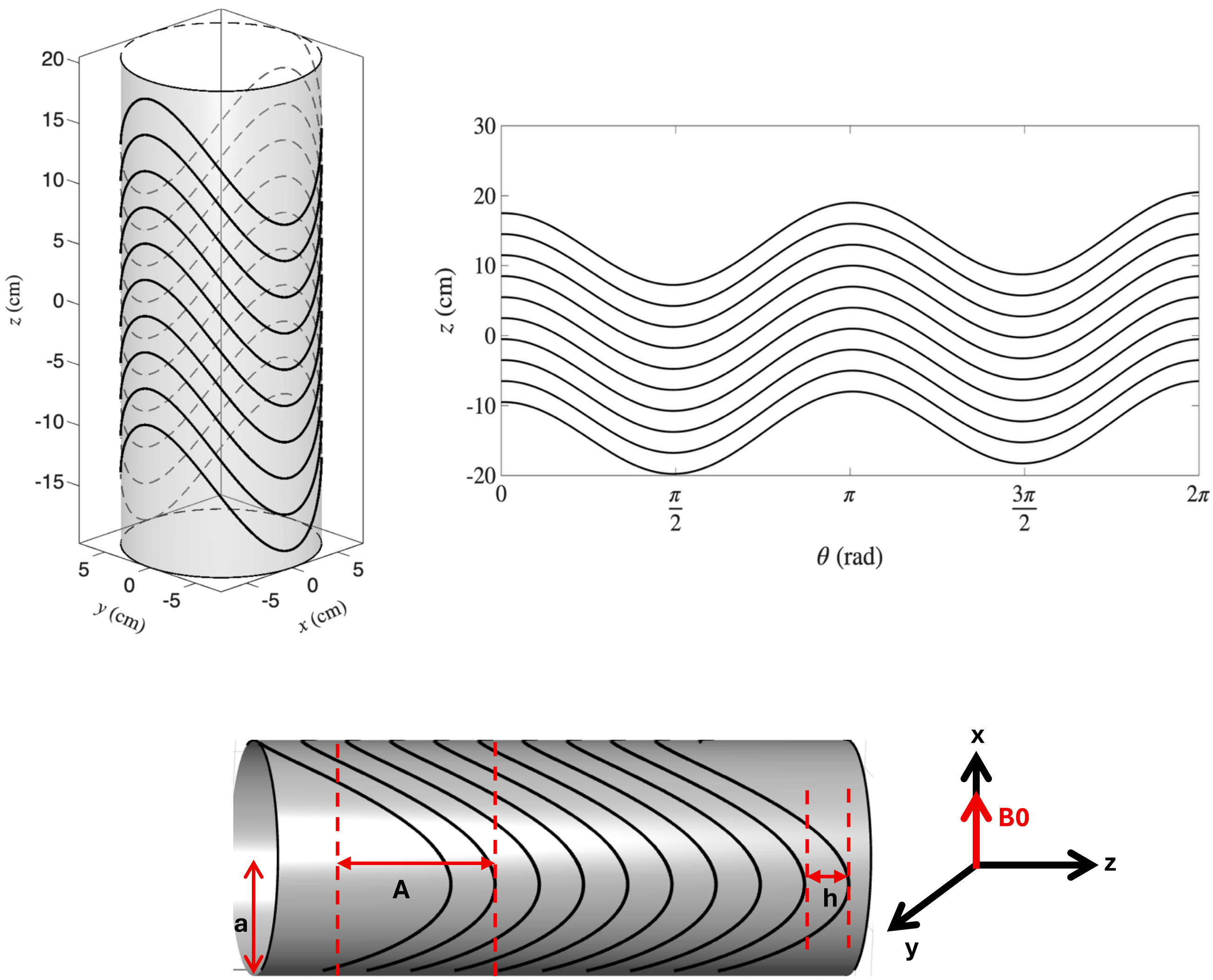

Figure 3.7: Geometry of a twisted solenoid coil with winding phase shift $\varphi = 90°$. (Top left) Three-dimensional representation of the wire winding pattern on a cylindrical former. (Top right) Axial coordinate z plotted as a function of azimuthal angle θ for individual turns, illustrating the sinusoidal modulation. (Bottom) Definition of the geometric parameters, including the cylinder radius a, modulation amplitude A, and turn advance h, together with the orientation of the main magnetic field B_0.

Although the parametric curve in Eq. 3.14 describes the winding pattern of the twisted solenoid, the practical implementation of a twisted solenoid with a winding pitch requires the current to return to the starting point after completing the winding. As a result, a return wire must be included to provide a path for the current. This return wire does not follow the winding pattern and generates unwanted magnetic fields that disrupt the intended RF phase gradient distribution and affect coil performance.

Phase Gradient	Winding Shift (φ)	Coil Rotation
$+G_x$	$0°$	$0°$
$-G_x$	$180°$	$90°$
$+G_y$	$270°$	$135°$
$-G_y$	$90°$	$45°$

Table 3.2: Relationship between phase gradient direction, winding shift, and coil rotation (Table taken from Ref. [63])

An example of a physically constructed twisted solenoid coil, including the return wire, is shown in Fig. 3.8. The effects of this return wire on the RF field distribution will be discussed in the following chapters. In this thesis, the twisted solenoid geometry described above forms the foundation of the novel coil designs proposed and their subsequent analysis. Throughout this work, the static magnetic field B_0 is assumed to be aligned along the x-axis, consistent with the configuration shown in Fig. 3.7.

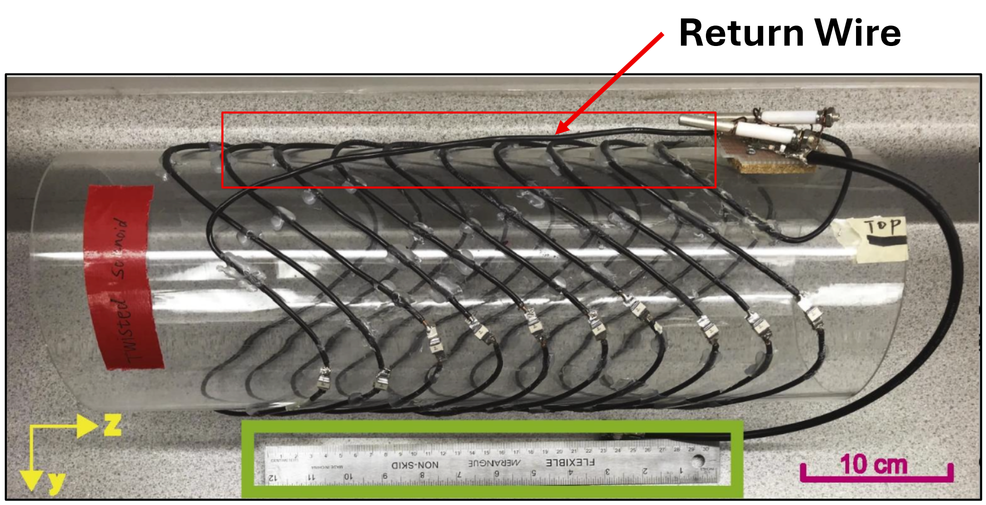

Figure 3.8: Photo of the constructed twisted solenoid coil. The red box indicates the location of the return wire, and the red arrow indicates the return wire. (Image modified from Ref. [63] with permission from Copyright Clearance Center (CCC) under license number 6230860503486.)

Chapter 4

Stream-Function-Based Coil Design and Biot-Savart Simulation

The image quality of TRASE MRI depends critically on the generation of a B_1 field with the appropriate properties (uniform magnitude and linear phase), making RF coil design crucial for this system. Improving coil performance can reduce imaging artifacts, increase efficiency, and improve overall signal quality. The twisted solenoid geometry described in Chapter 3 has demonstrated a strong capability to generate approximately linear RF phase gradients suitable for TRASE encoding. In this work, we extend the twisted-solenoid concept by exploring alternative winding patterns. One design is derived from the stream-function approach and discretized into a wire configuration, while the other combines two twisted solenoids wound in opposite directions to form a closed-loop configuration. Both designs are evaluated and shown to have improved performance over existing coils presently in use.

This chapter first introduces the concept of the stream function for RF coil design and applies it to the twisted solenoid geometry relevant to TRASE MRI. The continuous surface-current distribution is then discretized into practical wire windings using a standard method [67, 68, 69]. Finally, the Biot–Savart law is introduced as the framework for computing the magnetic field of the resulting coil geometries, to be used subsequently for field map generation and analysis of RF magnitude and phase characteristics

4.1 The stream function

The primary objective in RF coil design for TRASE MRI is to generate a magnetic field pattern with uniform magnitude and a linear phase gradient suitable for spatial encoding. Achieving this requires determining a surface current distribution that produces the required magnetic field while satisfying

Maxwell's equations. A convenient way to determine such current distributions is through the stream function method. Originally developed in fluid mechanics, the stream function has been widely applied to magnetic field synthesis and RF coil design [67, 68, 69]. This approach provides a practical way to construct surface current patterns that generate the required magnetic field.

For divergence-free surface currents confined to a conducting surface, the current density can be described using a scalar stream function ψ defined on that surface. The current density $\mathbf{j}$ is then given by

$$\mathbf{j} = \nabla \times (\psi \hat{\mathbf{n}}), \tag{4.1}$$

where $\hat{\mathbf{n}}$ denotes the unit normal vector to the surface. For the cylindrical former considered in this work, the surface normal direction corresponds to the radial unit vector $\hat{\rho}$ in cylindrical coordinates. which automatically satisfies

$$\nabla \cdot \mathbf{j} = \nabla \cdot (\nabla \times (\psi \hat{\mathbf{n}})) = 0. \tag{4.2}$$

In this representation, contours of the scalar stream function on a surface correspond to current streamlines, and differences in stream-function values between contours correspond to integrated current flow. Figure 4.1 illustrates the equivalence between flow streamlines and stream-function contours.

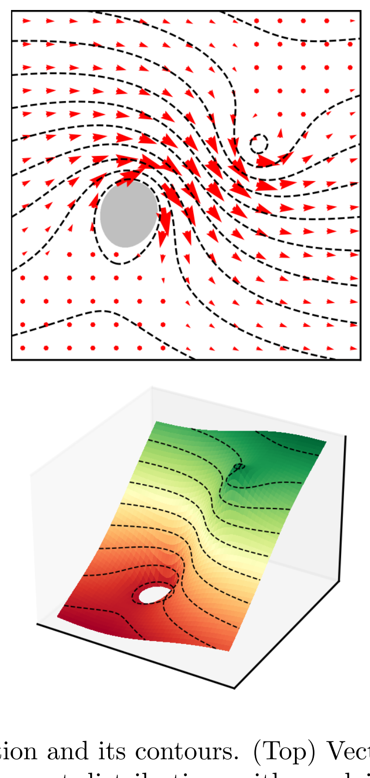

Figure 4.1: Example of a stream function and its contours. (Top) Vector field forming closed-loop trajectories, representing a divergence-free surface current distribution, with overlaid stream lines (dashed). (Bottom) The magnitude of the scalar stream function (vertical, color-coded), with contour lines (dashed) corresponding to specific constant values. (Image from `https://commons.wikimedia.org/wiki/File:Stream_function.png`.)

4.1.1 Application of stream function to the twisted-solenoid geometry

To apply the stream function concept to TRASE RF coil design, we consider the twisted-solenoid geometry introduced in Chapter 3. Since the winding is constrained to the surface of a cylinder, the surface current distribution can be naturally described on this geometry. The Cartesian coordinates of the winding pattern for twisted solenoid are given by the parametric curve

$$P(\theta) = \left[a\cos(\theta), a\sin(\theta), A_n \sin(n\theta + \varphi) + \frac{h}{2\pi}\theta\right]. \tag{4.3}$$

In the limit of a tightly-wound coil with thin wires carrying a current I, this can be represented by a surface current [61] (on a cylinder of radius a) comprising three terms:

$$\boldsymbol{j}(\theta, z) = \frac{I}{ha}\left[a\,\hat{\boldsymbol{\theta}} + \left(A_n n\cos(n\theta + \varphi) + \frac{h}{2\pi}\right)\hat{\boldsymbol{z}}\right], \tag{4.4}$$

where $\hat{\theta}$ and $\hat{z}$ are the azimuthal and axial unit vectors, respectively. The first term represents a uniform azimuthal surface current, corresponding to current circulating around the cylinder. The second term corresponds to a cosine–theta surface current distributed along the axial direction, which introduces the spatial modulation responsible for generating the desired phase-gradient behavior. The third term represents a uniform axial surface current component, which by Ampere's law produces no net magnetic field inside the coil volume [66]. Consequently, the third term can be neglected and, as we will show, one can arrive at a new twisted solenoid design that does not rely on a winding pitch and return wire.

By keeping only the components that contribute to the desired transverse magnetic field, the final expression for the surface current density of our novel twisted solenoid will be

$$\boldsymbol{j}(\theta, z) = \frac{I}{ha}\left[a\,\hat{\boldsymbol{\theta}} + A_n n\cos(n\theta + \varphi)\,\hat{\boldsymbol{z}}\right]. \tag{4.5}$$

Since only azimuthal and axial current components exist, the surface current is entirely tangent to the cylindrical surface. Therefore, the stream function must be oriented normal to the surface (i.e., in the radial direction), consistent with Eq. (4.1),

$$\boldsymbol{\psi} = \psi(\theta, z)\,\hat{\rho}, \tag{4.6}$$

where $\hat{\rho}$ is the radial unit vector.

Using the cylindrical-coordinate curl, the relationship between the stream function and the surface current components can be derived explicitly:

$$\nabla \times \boldsymbol{\psi} = \frac{\partial \psi}{\partial z}\hat{\theta} - \frac{1}{\rho}\frac{\partial \psi}{\partial \theta}\hat{z}. \tag{4.7}$$

Equation (4.1), Equation (4.5) and Equation (4.6) at $\rho = a$ gives

$$j_\theta = \frac{\partial \psi}{\partial z} = \frac{I}{h} \tag{4.8}$$

$$j_z = -\frac{1}{a}\frac{\partial \psi}{\partial \theta} = \frac{IA_n n}{ha}\cos(n\theta + \varphi). \tag{4.9}$$

A suitable scalar stream function on the cylindrical surface is thus

$$\psi(\theta, z) = Kz - KA_n \sin(n\theta + \varphi)\,, \tag{4.10}$$

which provides the desired surface current components, and K is the magnitude of the uniform azimuthal surface current (equal to I/h). The usefulness of the stream function lies in the properties that (i) contours of ψ represent the stream lines (or flow lines) of current on the cylindrical surface, and (ii) evenly spaced contours of ψ contain equal integrated surface current, as shown next.

4.1.2 Streamlines and equal-current contours

We now need an expression for contours of constant value of stream function mentioned in Eq. 4.10. Contours of this stream function correspond to current streamlines on the cylindrical surface. To verify that the streamline geometry matches the winding trajectory, consider the parametrized curve on the cylinder

$$P(\theta) = [a, \theta, A_n \sin(n\theta + \varphi) + z_i]\;, \tag{4.11}$$

which gives the cylindrical components of a contour of value $\psi = Kz_i$, where z_i is a constant (The subscript i will serve as a loop index in due order). This can be verified by substituting Eq. (4.11) for z in Eq. 4.10:

$$\begin{aligned}\psi(\theta) &= K\big(A_n \sin(n\theta + \varphi) + z_i\big) - KA_n \sin(n\theta + \varphi) \\ &= Kz_i = \text{const.}\end{aligned} \tag{4.12}$$

This shows that the stream function remains constant for all values of θ and the streamline follows the same path as the surface current.

Another important aspect of the stream function, which we mentioned earlier, is that equally spaced contours of ψ represent equal integrated surface current [68]. This indicates that the difference in ψ between any two adjacent contours corresponds to the same total surface current passing through the region between them. Consequently, plotting evenly spaced contours of ψ on the cylindrical surface provides a practical wire layout for building the coil. In this way, the stream function serves not only as a mathematical representation of the current distribution but also as a rigorous design tool outlining the wire paths needed to generate the desired magnetic field.

This is illustrated schematically in Fig. 4.2, where two adjacent contours ψ_1 and ψ_2 bound a surface region. The net current crossing any curve connecting the two contours is

$$\Delta I = \int_{l_1}^{l_2} \mathbf{j} \cdot \hat{\mathbf{n}}\, dl. \tag{4.13}$$

For example, integrating along a path of fixed θ (so $dl = dz$ and $\hat{\mathbf{n}} = \hat{\theta}$) gives

$$\Delta I = \int_{z_A}^{z_B} j_\theta\, dz = \int_{z_A}^{z_B} \frac{I}{h}\, dz = K(z_B - z_A). \tag{4.14}$$

From Eq. (4.10), the stream-function difference between the same endpoints at fixed θ is

$$\Delta\psi = \psi_2 - \psi_1 = K(z_B - z_A), \tag{4.15}$$

so that $\Delta I = \Delta\psi$. An analogous result is obtained for a path of fixed z (integration in θ), confirming that stream-function differences represent equal integrated current between adjacent contours:

$$\Delta I = \int_{\theta_A}^{\theta_C} \mathbf{J} \cdot \hat{\mathbf{z}}\, a d\theta = a \int_{\theta_A}^{\theta_C} J_z d\theta. \tag{4.16}$$

Taking J_θ from Eq. (4.5)

$$\Delta I = a \int_{\theta_A}^{\theta_C} \frac{I A_n n}{2\pi a} \cos(n\theta + \varphi) d\theta \quad = K A_n (\sin(n\theta_C + \varphi) - \sin(n\theta_A + \varphi)) \tag{4.17}$$

For $\Delta\psi = \psi_2 - \psi_1$ with fixed z

$$\begin{aligned} \Delta\psi &= K A_n \big[\sin(n\theta_C + \varphi) - \sin(n\theta_A + \varphi)\big] + K(z - z) \\ &= K A_n \big[\sin(n\theta_C + \varphi) - \sin(n\theta_A + \varphi)\big] \\ &= \Delta I \end{aligned} \tag{4.18}$$

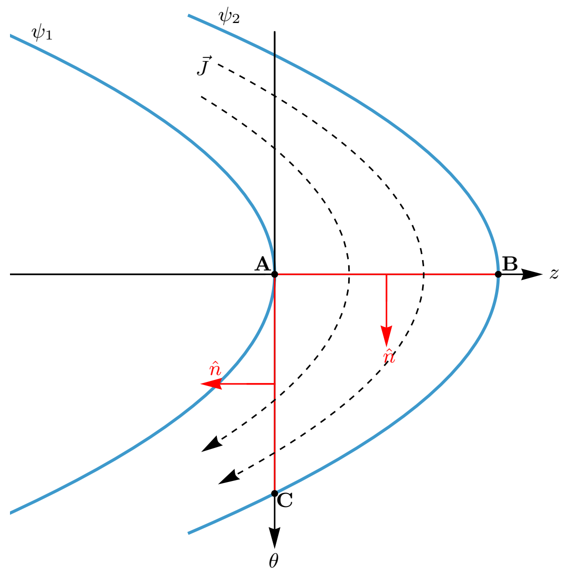

Figure 4.2: Schematic illustration of the stream function for surface current in (θ, z) coordinates. The contours ψ_1 and ψ_2 represent adjacent streamlines of the scalar stream function $\psi(\theta, z)$, along which the surface current $\mathbf{j}$ (dashed-curve)flows tangentially. Points **A**, **B**, and **C** indicate locations lying on these contours. Paths AB and AC correspond to the two different integration examples, with their respective unit normal vectors $\hat{\mathbf{n}}$.

4.2 Discrete current approximation

For the twisted solenoid RF coil considered in this work, the stream function formulation results in a continuous surface current distribution on the cylindrical surface. In order to obtain a discrete representation of this current distribution that approximates the same electromagnetic behaviour, the continuous current sheet must be transformed into a discrete set of wire contours. The methods laid out in Refs. [67, 68, 69] provide an efficient procedure for this transformation. The pertinent details are given here.

Consider two adjacent stream-function contours with values ψ_1 and ψ_2. The surface region between them acts as a current sheet carrying a net current

$$I = \psi_2 - \psi_1. \tag{4.19}$$

The discretization problem is to replace this sheet with a closed-loop wire that carries the same net current, thereby preserving the magnetic effect of the distributed current as closely as possible. Peeren [67] showed that, in this sense, the optimal wire location is the contour corresponding to the midpoint value:

$$\psi_c = \frac{1}{2}(\psi_1 + \psi_2), \tag{4.20}$$

which preserves the centroid of the current distribution and thus maintains its magnetic effect.

To generate N discrete loops spanning a stream function range from $\psi_{\min}$ to $\psi_{\max}$, we choose a uniform stream function increment that carries the same current through each loop

$$I = \frac{\psi_{\max} - \psi_{\min}}{N}. \tag{4.21}$$

The midpoint contour C_k then defines the centerline of the k-th loop:

$$C_k : \quad \psi = \psi_{\min} + \left(k - \frac{1}{2}\right) I, \qquad k = 1, 2, \ldots, N. \tag{4.22}$$

Eq. 4.22 therefore provides a constructive rule for placing discrete windings: loops are placed on the midpoint of stream function contours to avoid intersections, ensure equal current partitioning, and preserve the centroid of the original continuous surface-current distribution.

4.2.1 Discrete approximation for the twisted solenoid

Equation 4.11 describes the cylindrical coordinates of a contour corresponding to a constant value of the stream function given by Eq. 4.10. Applying the discretization rule defined in Eq. 4.22 to this stream function yields

$$K z_c - K A_n \sin(n\theta + \varphi) = \psi_{\min} + \left(k - \frac{1}{2}\right) I, \tag{4.23}$$

where z_c defines the axial coordinate of the centreline of the k-th discrete loop. Solving Eq. (4.23) for z_c gives

$$z_c = A_n \sin(n\theta + \varphi) + \frac{\psi_{\min}}{K} + \left(k - \frac{1}{2}\right) \frac{I}{K}. \tag{4.24}$$

Since $K = I/h$, the final term simplifies to $(k - \frac{1}{2})h$. Furthermore, the quantity $\psi_{\min}/K$ is a constant offset along the axial direction, which we denote by z_0. The axial coordinate of each discrete loop can therefore be written as

$$z_c = A_n \sin(n\theta + \varphi) + z_0 + \left(k - \frac{1}{2}\right) h. \tag{4.25}$$

To ensure that the discrete winding set is centred about the origin, the axial centre of the coil is required to lie at

$$z_{\text{center}} = \frac{z_{\max} + z_{\min}}{2} = 0, \tag{4.26}$$

where $z_{\min}$ and $z_{\max}$ correspond to the axial coordinates of the first $(k = 1)$ and last $(k = N)$ loops, respectively. Substituting Eq. 4.25 for $k = 1$ and $k = N$ into Eq. 4.26 gives

$$z_0 = -\frac{Nh}{2}. \tag{4.27}$$

With this choice of z_0, the discrete twisted-solenoid windings are symmetrically distributed about $z = 0$, preserving the axial centroid of the original continuous surface current distribution. The final format of

Eq. 4.11 will now be

$$P(\theta) = \left[a, \theta, A_n \sin(n\theta + \varphi) - \frac{Nh}{2} + (k - \frac{1}{2})h\right] . \tag{4.28}$$

To highlight the difference between the winding patterns resulting from Eq. 4.3 versus Eq. 4.28, we present two examples of each, side by side in Fig. 4.3. Uniform solenoids ($A_n = 0$) are shown in the top row. In contrast, twisted solenoids of the type used in TRASE ($n = 2$) are shown in the bottom row. Evenly spaced contours of the stream function of Eq. 4.10, which thereby contain equal integrated surface current, are also shown in each row for $A_n = 0$ and $n = 2$, respectively. All coils comprise ten turns. As can be seen in the left-side examples, Eq. 4.3 results in coils wound of a single contiguous wire that, owing to the winding pitch, traverses a region of equal integrated surface current (of Eq. 4.8 and Eq. 4.9) following each turn. Conversely, as seen in the right-side figures, Eq. 4.28 results in coils composed of discrete loops centred within each region of equal integrated surface current. As a result, this discretization procedure produces a set of independent loops that eliminate the continuous winding pitch, thereby removing the need for a return wire in the coil design.

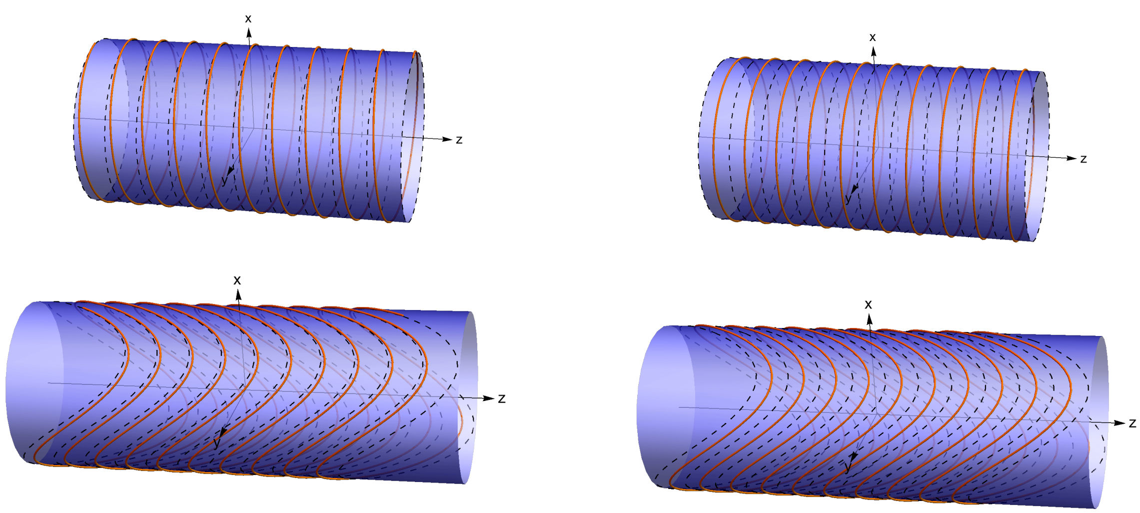

Figure 4.3: Conceptual examples of wire-wound approximations of the uniform (top row) and twisted (bottom row) solenoid. Left-side: single-wire pitch models via Eq. 4.3. Right-side: discrete-loop models via Eq. 4.11. For all drawings, the red lines are the wires, while the dashed lines indicate stream function contours of Eq. 4.10 containing equal integrated surface current. These contours are the same (left and right) for each of the two coil types (top with $A_n = 0$ and bottom with $n = 2$).

4.3 Visualization of the various twisted solenoid designs

To evaluate the performance of the proposed coil geometries, we compare our new stream-function-based twisted solenoid design with existing twisted solenoid winding patterns. In particular, a previous study [63] analyzed a pitch-wound twisted solenoid that, in practice, requires a return wire to complete the current path. This work also considers an idealized version of this geometry that ignores the return wire, which simplifies Biot–Savart simulations but does not represent a physically realizable coil.

In addition to these existing models, we introduce two alternative winding strategies designed to mitigate the effects of the return wire. The first alternative is a double-wound twisted solenoid in which two opposing pitch windings form a closed current loop. The second alternative is a discrete-loop twisted solenoid obtained from the stream-function discretization described in the previous section. To facilitate a direct comparison between these approaches, archetypal coil models considered in this thesis are illustrated in Fig. 4.4.

They can all be defined by a parametric curve of the form

$$\begin{bmatrix} P_x(\theta) \\ P_y(\theta) \\ P_z(\theta) \end{bmatrix} = \begin{bmatrix} a\cos\theta \\ a\sin\theta \\ A\sin(2\theta+\varphi)+H(\theta) \end{bmatrix}, \tag{4.29}$$

where we have dropped the subscript on A for simplicity, and the function $H(\theta)$ is specific to each coil type as described below.

For the incomplete twisted solenoid (ITS), often contemplated in Biot–Savart simulations in Refs. [63, 64, 65],

$$H(\theta) = \frac{h}{2\pi}\theta, \tag{4.30}$$

where the parameter θ runs from $-N\pi$ to $N\pi$ and N is the number of turns in the coil. As shown in Fig. 4.4(a), the current path is incomplete, since there is no return wire associated with this model. As such, it may be useful for conceptualization or exploring the broad characteristics of the twisted solenoid, but in general, should not be relied upon to provide detailed information about any practical realization of such a coil.

To address this, we also consider what we will call the real twisted solenoid (RTS). Here, a single current segment at fixed azimuthal angle connects the last point of the last turn (i.e., $\theta = N\pi$) to the first point of the first turn (i.e., $\theta = -N\pi$) of an ITS, thereby forming the closed current loop, as shown in Fig. 4.4(b) that must exist for any real, operable coil. As such, this model represents the actual twisted solenoid coils described in previous works [63].

The double-wound twisted solenoid (DWTS) is the first alternative approach to the RTS. As shown in Fig. 4.4(c), it features a return ITS to form a closed current loop and is thus the twisted-solenoid analogue of a two-layer uniform solenoid. For the outgoing ITS,

$$H(\theta) = \frac{h}{2\pi}\theta, \qquad \theta \in [-N\pi,\, N\pi], \tag{4.31}$$

as above. For the return ITS,

$$H(\theta) = Nh - \frac{h}{2\pi}\theta, \qquad \theta \in [N\pi,\, 3N\pi], \tag{4.32}$$

which connects the two sections at both ends.

The discrete-loop twisted solenoid (DLTS) is our second alternative to the RTS and is based on the stream-function design method described above. Here, using Eq. 4.25 with $z_i = h\,i$,

$$H(\theta) = -\frac{h(N+1)}{2} + hi, \tag{4.33}$$

where i is the loop index running from 1 to N, and $\theta \in [-\pi,\, \pi]$ for each loop. For example, the first loop ($i = 1$) follows Eq. 4.29 with

$$H(\theta) = -\frac{hN}{2} + \frac{h}{2}, \tag{4.34}$$

and lies at the midpoint between the contours of ψ with $H(\theta) = -hN/2$ and $H(\theta) = -hN/2 + h$.

For the DLTS, h is the spacing between evenly spaced contours of ψ (for fixed θ). Equivalently, it is the loop-to-loop spacing (for fixed θ), and therefore $1/h$ is the axial loop density. For direct comparison to the ITS, RTS, or DWTS (Fig. 4.4(a)–(c)), one should choose h to match the winding pitch of those models, as was done in Figs. 4.3 and 4.4. In practice, the individual loops of the DLTS are connected in series, with a single return wire from the end of the Nth loop to the start of the first loop, as shown in Fig. 4.4(d). The overlap of the connecting wires with the return wire nullifies their net magnetic field, and one needs to consider only the closed current paths of the individual loops for Biot–Savart simulations [68, 69].

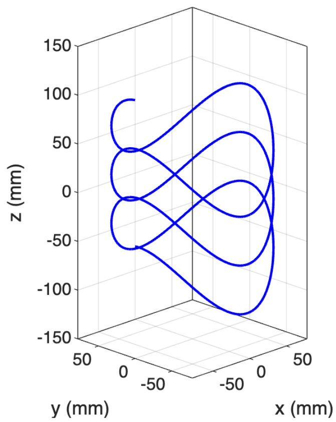

(a) ITS

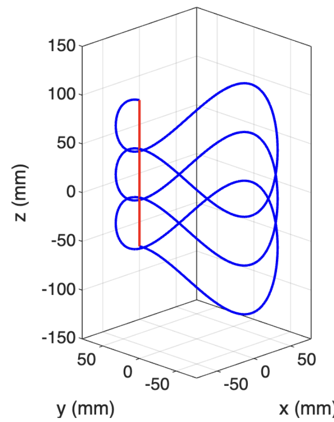

(b) RTS

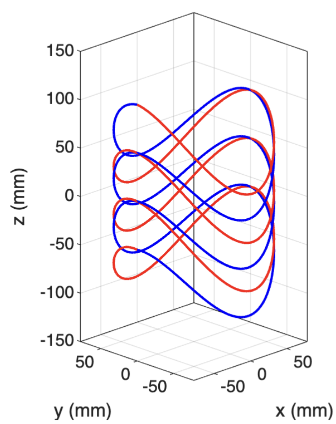

(c) DWTS

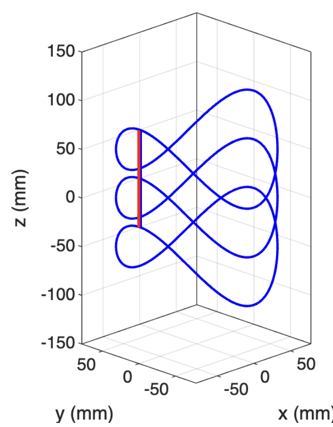

(d) DLTS

Figure 4.4: Examples of the four archetypal twisted-solenoid winding patterns considered in this work: (a) the incomplete twisted solenoid (ITS), (b) the real twisted solenoid (RTS), (c) the double-wound twisted solenoid (DWTS), and (d) the discrete-loop twisted solenoid (DLTS). The red lines in the RTS, DWTS, and DLTS indicate return wires or windings. The following parameters were used for all coils: $a = 78$ mm, $A = 40$ mm, $\varphi = 90°$, $h = 50$ mm, and $N = 3$.

4.4 Magnetic field calculation using the Biot–Savart law

One of the key steps following the design and fabrication of an RF coil is the evaluation of the B_1 magnetic field produced by the coil. In high-field MRI systems, the RF excitation frequency is sufficiently high that the corresponding electromagnetic wavelength becomes comparable to the dimensions of the RF coil and the human body. Under these conditions, the interaction between the B_1 field and the human body cannot be neglected, and the current distribution along the coil elements becomes spatially non-uniform, exhibiting variations in both amplitude and phase. Several studies have shown that these electrodynamic effects lead to complex current patterns, B_1 field inhomogeneity, and increased electric fields and specific absorption rate (SAR) at high frequencies, thereby necessitating the use of full-wave numerical solutions of Maxwell's equations for accurate RF coil analysis and design[70, 71, 72]. In contrast, for low-field MRI systems, the electromagnetic wavelength is much larger than the dimensions of the RF coil and the human body. In this regime, these electrodynamic effects become negligible, and the B_1 field can be accurately calculated using the Biot–Savart law in the absence of the human body.

To evaluate and compare the performance of the different winding configurations investigated in this thesis, the B_1 magnetic field is calculated using the Biot–Savart law. As illustrated in Fig. 4.5, an example of an incomplete twisted solenoid is shown to demonstrate the magnetic field calculation procedure. The winding pattern is defined by the parametric equation introduced earlier in this chapter, from which a set of discrete points is generated to describe the coil geometry.

For clarity, a representative portion of the winding is highlighted in Fig. 4.5(a) and magnified in Fig. 4.5(b), where the continuous wire is approximated by a sequence of discrete points $\mathbf{X}_1, \mathbf{X}_2, \ldots$. Each pair of adjacent points defines a finite straight-line segment carrying a uniform current. A representative segment, defined by two neighboring points $\mathbf{X}_i$ and $\mathbf{X}_f$, is shown in Fig. 4.5(c), where the magnetic field contribution at an observation point $\mathbf{X}$ is evaluated using the Biot–Savart law.

Following the formulation presented in Ref. [73], the magnetic field generated by a finite straight current segment carrying a current I is given by

$$\mathbf{dB} = \frac{\mu_0 I}{4\pi}\,\hat{\mathbf{e}} \times \mathbf{R}_i\,\frac{2L\,(R_i + R_f)}{R_i R_f\left[(R_i + R_f)^2 - L^2\right]}, \tag{4.35}$$

where the segment length is defined as $L = |\mathbf{X}_f - \mathbf{X}_i|$, and the unit vector along the segment is

$$\hat{\mathbf{e}} = \frac{\mathbf{X}_f - \mathbf{X}_i}{L}. \tag{4.36}$$

The vectors from the segment endpoints to the observation point $\mathbf{X}$ are given by

$$\mathbf{R}_i = \mathbf{X} - \mathbf{X}_i, \qquad \mathbf{R}_f = \mathbf{X} - \mathbf{X}_f, \tag{4.37}$$

with corresponding magnitudes $R_i = |\mathbf{R}_i|$ and $R_f = |\mathbf{R}_f|$. Here, $\mu_0 = 4\pi \times 10^{-7}$ H/m is the permeability of free space.

The total magnetic field is then obtained by summing the Biot–Savart contributions from all individual segments.

$$\mathbf{B} = \sum_{j=1}^{N_{\text{seg}}} d\mathbf{B}_j, \tag{4.38}$$

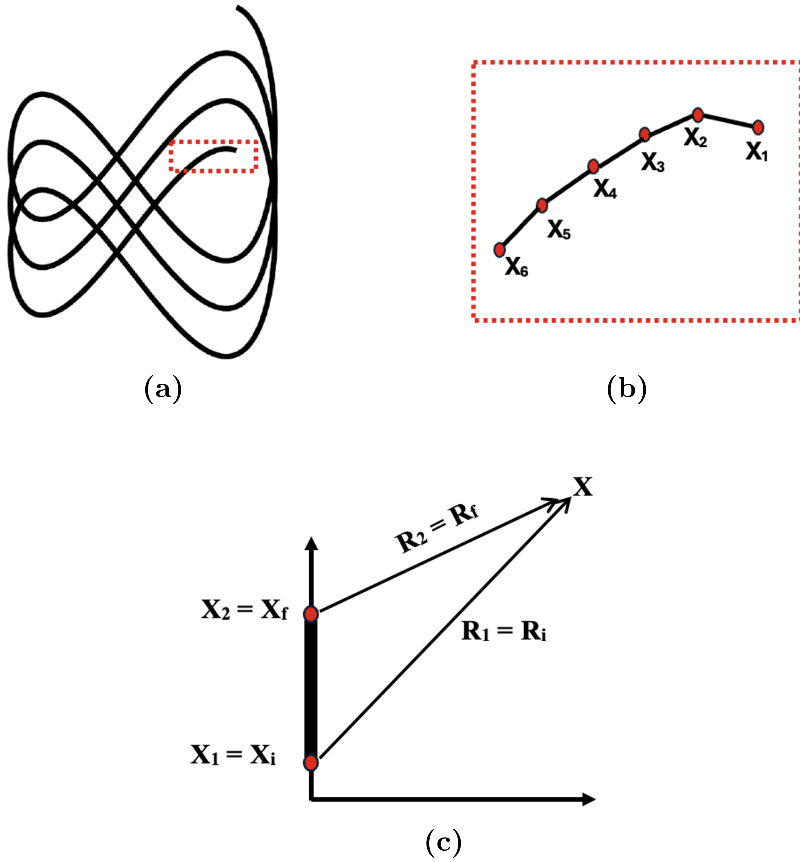

Figure 4.5: Schematic illustration of the magnetic field calculation for a twisted solenoid coil using finite straight current segments. (a) Example of an incomplete twisted solenoid with three turns. The red dashed box indicates a representative portion of the winding highlighted. (b) Magnified view of the highlighted region, showing the discretization of the wire into a sequence of points $\mathbf{X}_1, \mathbf{X}_2, \ldots$, where adjacent points define straight-line current segments. (c) Geometry of a representative segment defined by two neighboring points $\mathbf{X}_i$ and $\mathbf{X}_f$ (e.g., $\mathbf{X}_1$ and $\mathbf{X}_2$), along with the observation point $\mathbf{X}$ and the vectors $\mathbf{R}_i$ and $\mathbf{R}_f$ used in the Biot–Savart formulation.

Where N_{seg} is the total number of segments that constitute the coil winding pattern, and $d\mathbf{B}_j$ is the magnetic-field contribution of the jth segment evaluated using the Biot–Savart law. Thus, the coil geometry is represented as a superposition of magnetic fields generated by many straight current segments.

Following the approach adopted in Refs. [63, 64, 65], the magnetic field analysis in this work focuses on the radiofrequency (RF) field components relevant to TRASE MRI. The coordinate system is defined such that the x-axis is aligned with the static magnetic field B_0 as shown in Fig. 4.6. The transmitted RF magnetic field $\mathbf{B}_1$ can be decomposed into components that are perpendicular and parallel to the static magnetic field $\mathbf{B}_0$. The component of the RF field that lies parallel to $\mathbf{B}_0$ is commonly referred to as the concomitant field, B_{1x} (assuming $\mathbf{B}_0$ is aligned along the x-axis), and is typically negligible. In conventional MRI, only the transverse components of $\mathbf{B}_1$ efficiently drive nuclear spin excitation, while the longitudinal (concomitant) component does not directly contribute to spin rotation.

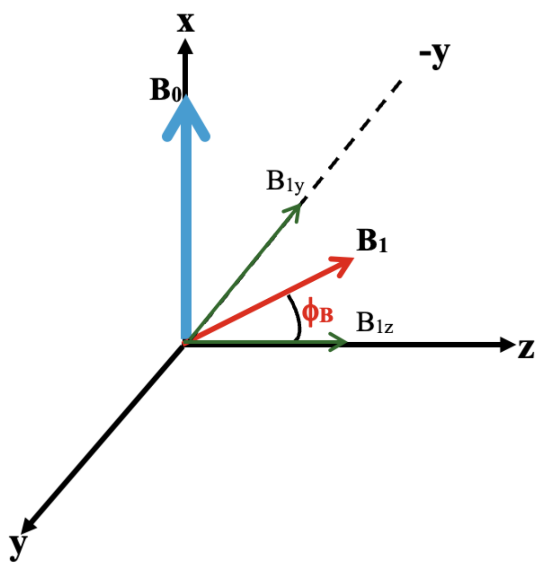

Figure 4.6: Definition of the coordinate system used for RF field analysis in TRASE MRI. The static magnetic field B_0 is aligned along the x-axis. The transmitted RF field $\mathbf{B}_1$ is shown together with its component perpendicular to B_0. The angle ϕ_B denotes the phase of $\mathbf{B}_1$ relative to the z-axis.

In standard implementations of TRASE MRI, the concomitant B_{1x} field is generally negligible and does not significantly affect image formation [9, 10, 63, 66, 74]. However, at very low static magnetic field strengths B_0, the relative contribution of B_{1x} may increase and should be taken into consideration [75]. Accordingly, the RF magnetic field $\mathbf{B}_1$ is taken to consist of the transverse components B_{1y} and B_{1z}. From these components, the magnitude of the RF field is defined as

$$|\mathbf{B}_1| = \sqrt{B_{1y}^2 + B_{1z}^2}, \tag{4.39}$$

while the spatial phase of the RF field is given by

$$\phi_B = \tan^{-1}\left(-\frac{B_{1y}}{B_{1z}}\right). \tag{4.40}$$

The spatial phase gradient is then defined as

$$G_r = \frac{\partial \phi_B}{\partial r}, \tag{4.41}$$

where r denotes the phase-gradient direction $(\pm x, \pm y)$ determined by the winding shift φ.

The equations presented in this chapter, including the Biot–Savart law for magnetic field calculation, the definition of the RF field phase, and the corresponding phase gradient, are used in the next chapter to evaluate the key characteristics of the magnetic field generated by the twisted solenoid with the different wire patterns described earlier. In particular, these expressions are used to compare different winding configurations in terms of B_1 field uniformity and phase-gradient linearity, and to identify the configurations that provide a better performance.

Chapter 5

Comparison of the Four Archetypal Winding Patterns

5.1 Introduction

The four twisted solenoid winding configurations (ITS, RTS, DWTS, and DLTS) are compared under identical geometric parameters to isolate the effect of winding pattern on RF field performance. By keeping the number of turns, coil radius, twist amplitude, winding shift, and turn advance fixed for all designs, any observed differences in the resulting B_1 characteristics can be attributed solely to the winding pattern.

The quasi-static magnetic field is calculated using the Biot–Savart formulation, and the resulting B_1 magnitude, phase, and phase-gradient distributions, computed using Eqs. 4.39, 4.40, and 4.41, are evaluated within the imaging region relevant to TRASE MRI. In particular, the comparison focuses on the homogeneity of $|B_1|$, the linearity of the phase, and the uniformity of the phase gradient G_x along the encoding direction. These criteria allow a direct assessment of how the winding pattern influences encoding performance. The winding geometries and corresponding B_1 field maps are presented at three axial planes ($z = -5$, 0, and 5 cm), with $|B_1|$ normalized to its value at the coil isocenter to allow direct comparison between configurations.

The parametric curve equations required to generate the four winding patterns, which were described in detail in the previous chapter, are summarized in the Table 5.1 below. They are the same as is given in Eq. 4.29, but are written out specifically for each coil here for clarity and convenience. These equations provide the coordinates of the coil segments, enabling their use in the Biot–Savart law calculations. Each set of parametric equations describes a different winding geometry. As a reminder, the ITS represents a twisted solenoid with no return wire. The RTS is the same as the ITS, but with a return wire added to complete the current path. The DWTS consists of two counter-wound ITS structures. The DLTS approximates the twisted geometry using a set of discrete loops indexed by i, rather than a continuous winding.

Coil type	$P_x(\theta)$	$P_y(\theta)$	$P_z(\theta)$
ITS	$a\cos\theta$	$a\sin\theta$	$A\sin(n\theta+\varphi)+\dfrac{h\theta}{2\pi},\ (\theta\in[-N\pi,N\pi])$
RTS	$a\cos\theta$	$a\sin\theta$	$A\sin(n\theta+\varphi)+\dfrac{h\theta}{2\pi},\ (\theta\in[-N\pi,N\pi])$ (connect last point to first point)
DWTS	$a\cos\theta$	$a\sin\theta$	(i) $A\sin(n\theta+\varphi)+\dfrac{h\theta}{2\pi},\quad(\theta\in[-N\pi,N\pi])$ (ii) $A\sin(n\theta+\varphi)+Nh-\dfrac{h\theta}{2\pi},\quad(\theta\in[N\pi,3N\pi])$
DLTS	$a\cos\theta$	$a\sin\theta$	$A\sin(n\theta+\varphi)-\dfrac{h(N+1)}{2}+hi,\quad(\theta\in[-\pi,\pi],\ i=1,2,\ldots,N)$

Table 5.1: Parametric curve equations defining the geometry of the ITS, RTS, DWTS, and DLTS coil configurations, based on the general formulation in Eq. 4.29. Here, a is the coil radius, A is the twist amplitude, n is the multipole order, φ is the winding shift, h is the axial pitch (turn advance), N is the number of turns, and i denotes the discrete loop index (for DLTS).

5.2 Numerical simulation and evaluation method

To ensure a consistent comparison between the four archetypal winding patterns, a numerical simulation framework is employed as described below. Simulation is achieved by splitting the coils into many small straight-line current segments set by 1° steps of the parameter θ in the equations in the Table Eq. 5.1, and subsequently calculating their contributions to the net magnetic field vector at a given point via in-house code (MATLAB) using the form of the Biot-Savart law for a filamentary segment in Eq. 4.35 as discussed in Section 4.4. The straight return wire of the RTS coil is treated as a single current segment. We use 18,000 sample points for the 2D plots featured in the following sections, and 200 sample points for the 1D plots. The phase gradient of Eq. 4.41 is determined numerically using the built-in gradient function in MATLAB.

5.3 Results

5.3.1 Comparison of the four archetypal twisted solenoid winding patterns

The parameters for all winding patterns in this study are summarized in the Table. 5.2 and were taken from coil number #1 in Ref. [63], which was the top ranking design that came out of a parameter search study, subject to selection criteria on the basis of B_1 field uniformity and phase gradient strength, followed by a ranking criterion based on a coil efficiency metric. A version of this coil was constructed and used along with a uniform saddle coil for a successful demonstration of 1D TRASE MRI [63]. Field mapping with a pick-up coil showed close agreement with Biot–Savart simulations [63]. According to Table 3.2 and the parameter of winding shift, all patterns produce a phase gradient along the x-axis, i.e., they are G_x coils.

Parameter	Value
Number of turns (N)	10
Coil radius (a)	7.8 cm
Twist amplitude (A)	5.5 cm
Winding shift (φ)	0°
Turn advance (h)	3.0 cm

Table 5.2: Coil parameters used for all twisted solenoid winding patterns considered in this study.

The winding patterns explored here are shown in Figs. 5.1 through 5.4, along with contour plots of B_1 magnitude and phase at three axial planes ($z = -5$, 0, and 5 cm). The B_1 field magnitude is normalized to its value at the coil isocenter $(0, 0, 0)$ for each coil type.

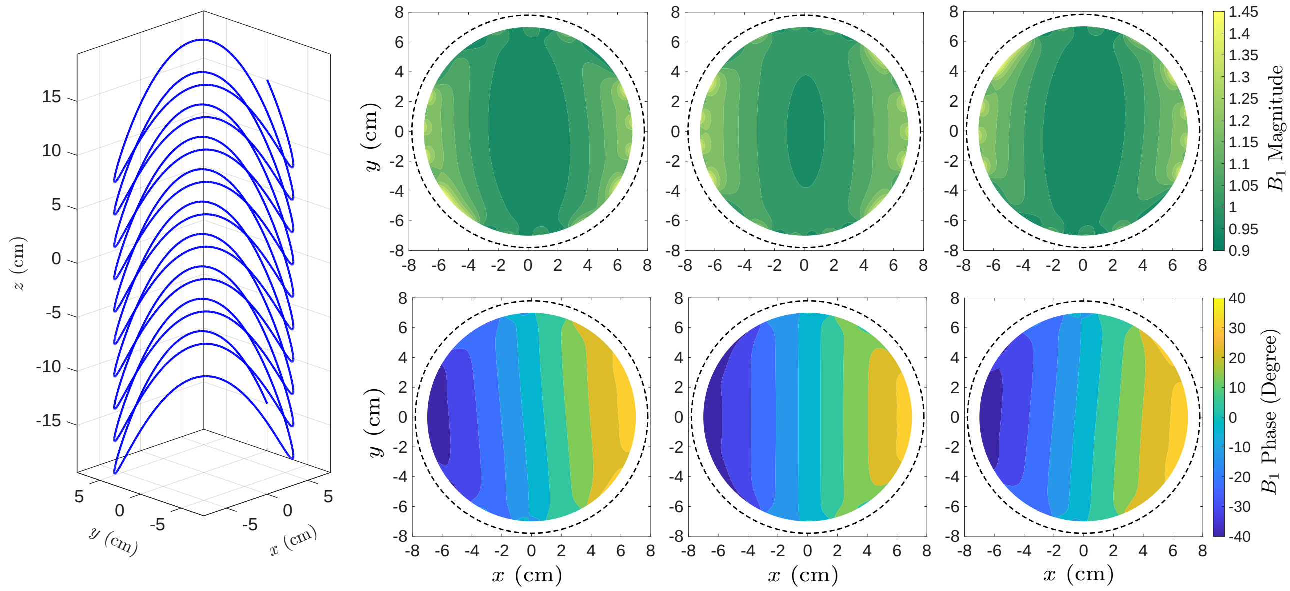

Figure 5.1: Results for the incomplete twisted solenoid. The left panel shows the ITS winding pattern. The top row of contour plots on the right displays the B_1 magnitude maps at three axial planes (left: $z = -5\,\text{cm}$, middle: $z = 0\,\text{cm}$, and right: $z = 5\,\text{cm}$), while the bottom row shows the corresponding B_1 phase maps. The dashed line indicates the coil winding surface.

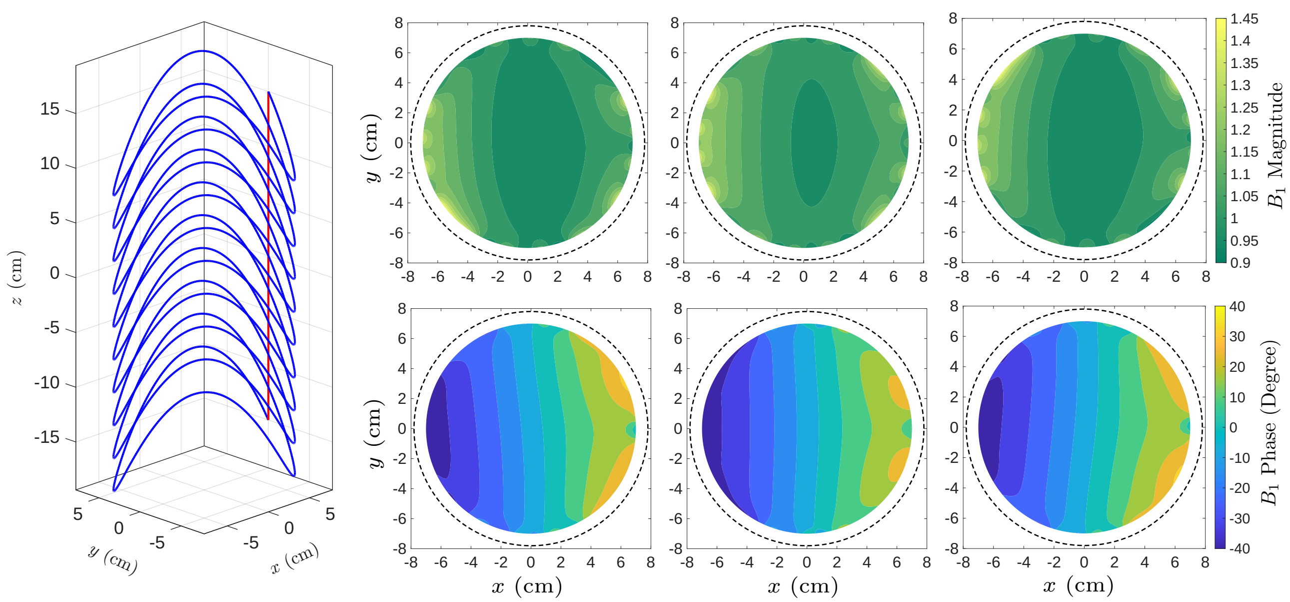

Figure 5.2: Same as Fig. 5.1, but for the RTS coil.

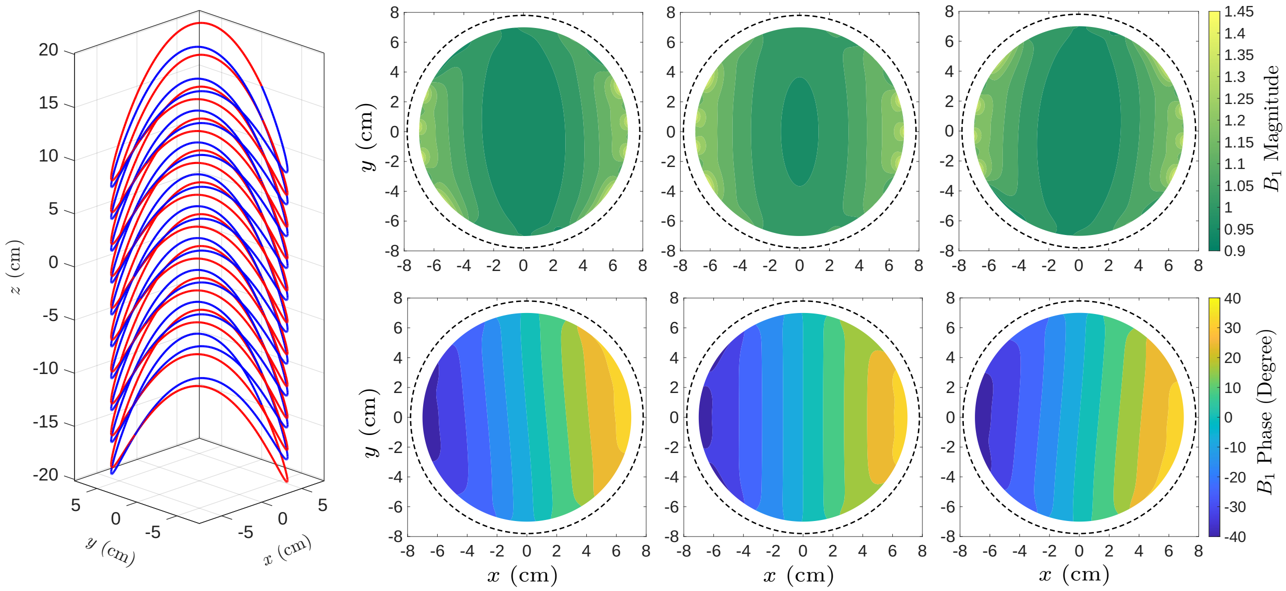

Figure 5.3: Same as Fig. 5.1, but for the DWTS coil.

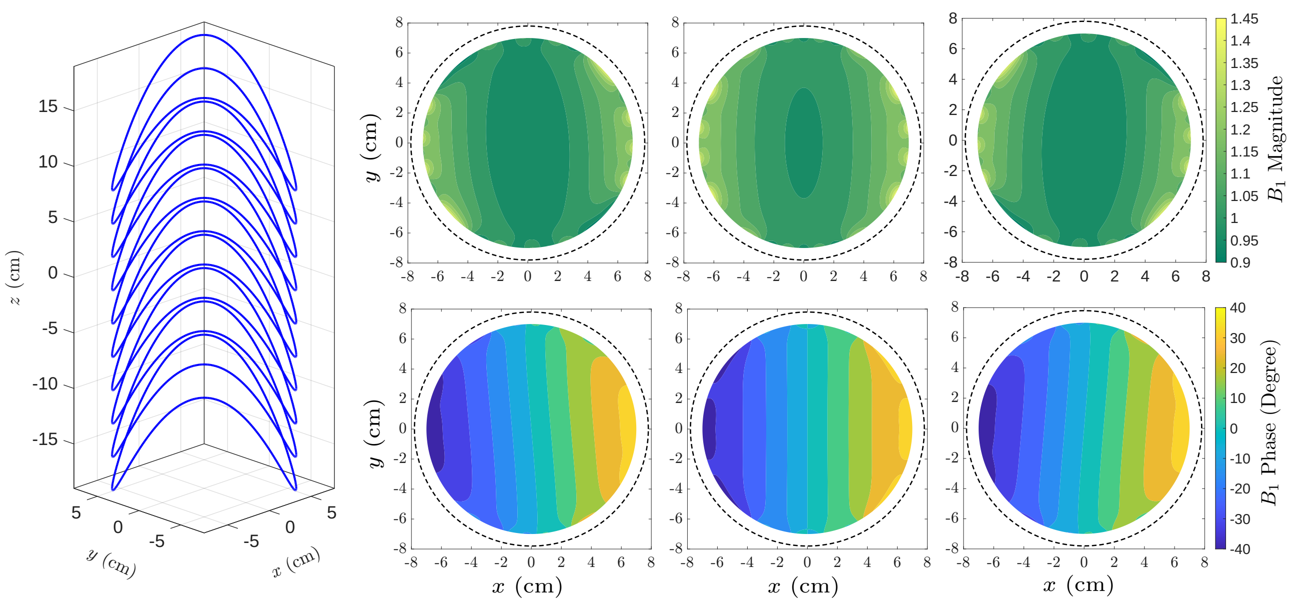

Figure 5.4: Same as Fig. 5.1, but for the DLTS coil.

As can be observed in Figs. 5.1 through 5.4, the ITS, DWTS and DLTS coils all produce very similar B_1 field distributions, with near equivalent phase and phase gradient profiles. For the RTS coil, on the other hand, the return wire introduces a strong asymmetry, resulting in significant degradation of all B_1 field characteristics.

As can be seen from Table 5.1, all four winding patterns, including the RTS design, contain the same sinusoidal axial modulation term $A\sin(n\theta + \varphi)$. This term is responsible for generating the spatially varying transverse current distribution that produces the desired RF phase gradient in TRASE encoding. Therefore, the fundamental phase-gradient mechanism is identical for the ITS, RTS, DWTS, and DLTS coils.

The differences do not arise from the modulation term itself, but rather from how the current path is completed. The ITS configuration represents an open winding pattern and cannot be realized in practice since it lacks a return wire and therefore does not form a closed current loop. The DWTS and DLTS designs preserve the sinusoidal modulation while implementing geometrically balanced return paths. In contrast, the RTS configuration closes the current wire with a straight longitudinal return conductor, introducing a localized perturbation to the otherwise sinusoidal current pattern. This asymmetry distorts the transverse B_1 field components, degrading the uniformity of B_1 magnitude, phase linearity, and phase-gradient homogeneity.

As a result, the DWTS and DLTS designs emerge as excellent alternative winding patterns for twisted solenoid coils for TRASE MRI, offering improved characteristics over the hitherto employed RTS design [63]. Of these two, the DLTS offers the additional advantage of requiring much less wire to construct, as it does not need two layers.

The nominal characteristic of the four winding patterns is summarized in Table 5.3. The ITS, DWTS, and DLTS designs have nearly identical mean phase-gradient values, whereas the RTS coil shows a noticeably reduced gradient, consistent with the degradation observed in the field plots. Although the DWTS configuration achieves approximately twice the B_1 magnitude at the isocenter due to its second layer, and thus twice the total number of turns, this improvement comes at the cost of substantially greater total wire length. The DLTS design, by contrast, preserves the desired phase-gradient performance while maintaining a total wire length comparable to the RTS coil.

Another important aspect in comparing these configurations is their expected electrical behavior, particularly the coil inductance. Since the DLTS coil has the same radius, the same number of turns (with similar spacing), and essentially the same total wire length as the RTS coil reported in Ref. [63], one expects it to exhibit a similar inductance and, if constructed using the same conductor material, a comparable quality factor and overall electrical performance. Here, the inductance represents the proportionality between the current flowing in the coil and the magnetic energy stored in its surrounding field. For a given geometry, inductance primarily depends on the number of turns and magnetic flux. Although the present work focuses on B_1 field calculations rather than circuit-level modeling, inductance remains relevant from a practical standpoint, as it affects the coil's overall RF efficiency.

In contrast, the DWTS coil, having approximately double the total number of turns, is expected to possess an inductance roughly four times greater than that of the RTS coil, according to standard solenoidal inductance scaling. This increased inductance may influence tuning requirements, matching network design, and transient response characteristics, and therefore constitutes an additional practical consideration in choosing between the DWTS and DLTS configurations.

Coil type	$B_1(0,0,0)$ (μT/A)	$\overline{G}_x$ (deg/cm)	Wire length (m)
ITS	36.61	5.38	6.81
RTS	36.71	4.50	7.11
DWTS	72.96	5.37	13.62
DLTS	36.52	5.36	7.35

Table 5.3: Summary of the nominal characteristics of the four different coil types, including the magnitude of B_1 at the coil isocenter, the mean phase gradient, and the total wire length. The mean phase gradient $\overline{G}_x$ is calculated along the x-axis at $y = z = 0$ over the imaging volume diameter used in Ref. [63], corresponding to 70% of the coil diameter (10.9 cm). For the DLTS coil, the total wire length also includes the connecting and return wires, which are not shown in Fig.5.4 for clarity.

5.3.2 Impact of wire length on practical coil design

Wire length may also become a limiting factor when it approaches a non-negligible fraction of the electromagnetic wavelength at the operating frequency. A commonly used rule of thumb is that the total conductor length should remain below $\lambda/20$ [76], in order to ensure that current phase variations along the wire remain small.

At the operating frequency of 9.28 MHz used in Ref. [63], the free-space wavelength is approximately 32.3 m, so $\lambda/20$ corresponds to about 1.6 m. This value is significantly shorter than the total wire length of the RTS coil (see Table 5.3), indicating that finite wavelength effects may become non-negligible if not properly managed. To mitigate potential wavelength-related effects, distributed capacitors along the coil length are employed [63], a standard technique that helps maintain a constant RF current phase throughout the entire conductor path.

Since the DLTS design requires only approximately 3% more wire than the RTS coil, it emerges as the ideal substitute, then, for implementations of TRASE at this frequency, assuming one uses the same distributed capacitance approach. By scaling with respect to wire length, the longer DWTS configuration, having nearly twice the total wire length, may require operation at lower frequencies than 9.28 MHz to maintain the same $\lambda/20$ criterion. One would similarly expect that the longer DWTS coil with distributed capacitors should perform equally well (as predicted by quasi-static Biot-Savart simulations) up to 4.8 MHz. Conversely, smaller coils with shorter total wire lengths should be useable at frequencies higher than 9.28 MHz. However, the extent to which any particular design can be used beyond this experimentally tested frequency [63] (scaled to total wire length) may require full-wave simulations to determine.

5.4 1D field profiles along phase gradient direction

Figure. 5.5 provides a side-by-side comparison of all coils for the B_1 magnitude, phase, and phase gradient along the x-axis at $y = 0$ in each of the three aforementioned axial planes. These 1D plots provide a clearer visualization of linearity and uniformity already observed in the two-dimensional contour maps.

The $|B_1|$ curves show again that the ITS, DWTS, and DLTS configurations exhibit nearly identical spatial variation across the imaging region, despite differences in absolute amplitude. Although the DWTS coil produces a higher overall field strength, its normalized magnitude distribution follows the same spatial behavior as the ITS and DLTS designs. In contrast, the RTS coil demonstrates clear asymmetry in its magnitude profile, particularly away from the isocenter.

The phase plots further emphasize these differences. The ITS, DWTS, and DLTS coils maintain highly linear phase across the central imaging region, whereas the RTS configuration shows degradation of phase linearity due to the return wire. It is also important to note that, due to the constraint of Maxwell equations, the transverse RF field cannot simultaneously exhibit perfectly linear phase and perfectly uniform magnitude. A spatially varying phase necessarily implies a redistribution of current density, which introduces variations in $|B_1|$. This trade-off is clearly visible in Fig. 5.5. A variation of approximately 10–15% in $|B_1|$ is typically considered acceptable in TRASE [9, 63, 65, 77].

Finally, it should be noted that the adverse effect of the return wire in the RTS configuration can be mitigated by physically rotating the coil and repositioning the return segment. This approach reduces the asymmetry introduced by the return conductor. A detailed description of this method is provided in the next section.

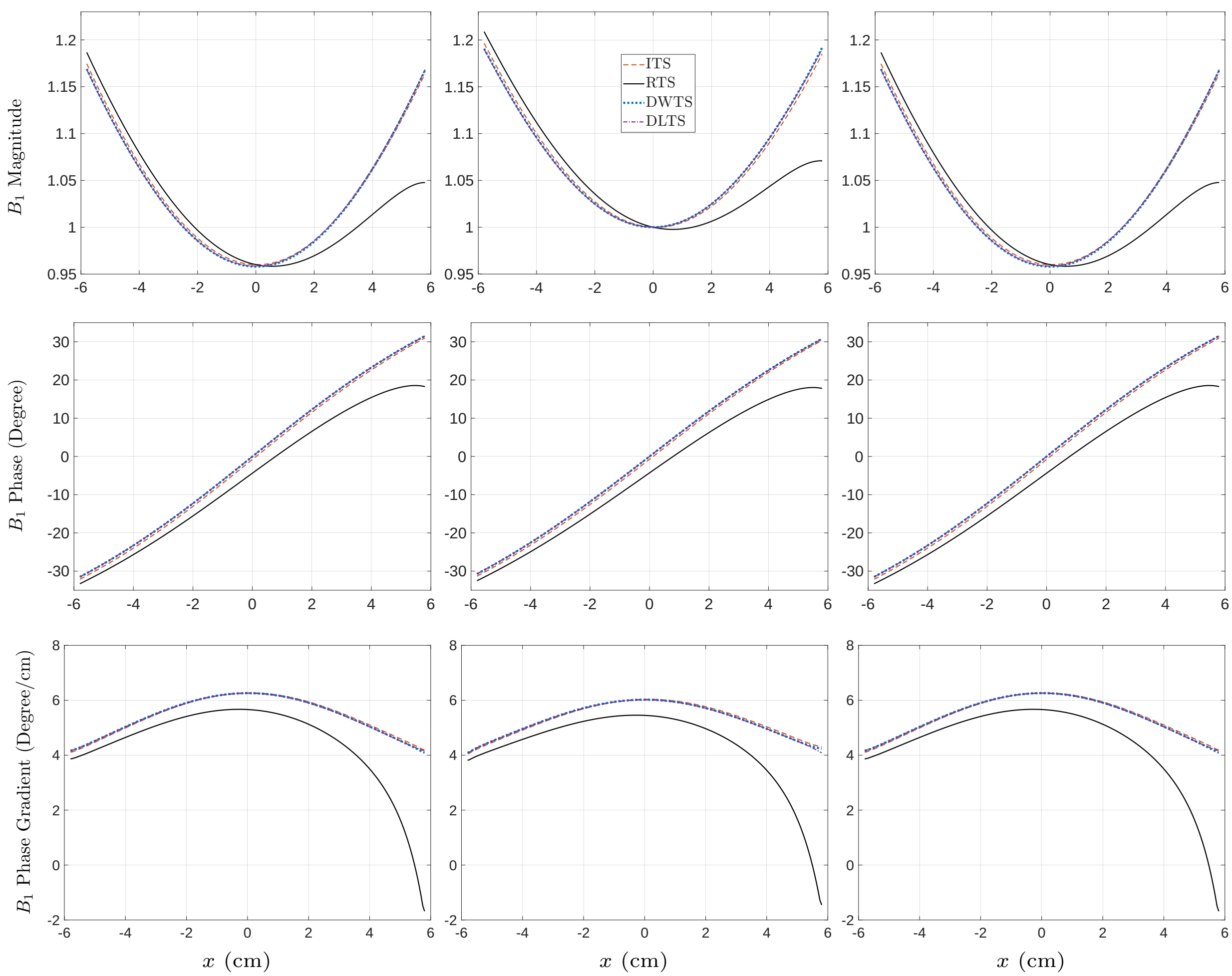

Figure 5.5: B_1 magnitude, phase, and phase gradient along the x-axis for $y = 0$ in three axial planes: $z = -5\,\text{cm}$ (left), $z = 0\,\text{cm}$ (middle), and $z = 5\,\text{cm}$ (right), across the four coil designs. The single legend applies to all panels.

5.5 Effect of shifting the angular location of the return wire in RTS

As noted previously, the RTS coil exhibits the poorest performance in terms of B_1 magnitude uniformity and phase linearity. This degradation is due to the additional return wire segment, which significantly alters the RF magnetic field distribution, in particular the B_{1y} component. It is worth noting, however, that the impact of this segment can be mitigated, making the RTS coil more suitable for TRASE MRI in situations where the impact of a B_{1x} component of the RF field can be safely ignored.

To address this issue, the position of the return wire can be adjusted to minimize its contribution to B_{1y}, thereby improving the overall magnetic field performance of the coil. This can be achieved by an appropriate combination of a winding shift φ and a physical rotation of the coil about the z-axis to change the angular position of the return wire while preserving the desired phase-gradient direction of the coil. For clarity and to avoid conflating the primary purpose of the winding shift, we propose a different, and, in our opinion, simpler schema. The specific steps are the following:

(i) φ is chosen, as usual, to set the phase gradient direction;

(ii) an offset θ_{offset} is added to the parameter θ in Table. 5.1 to shift the start and end points of the coil, thereby relocating the return path; and

(iii) the B_1 field of the coil is evaluated at, and relative to, its physical central plane, where imaging will occur. In this case, the central plane is no longer at $z = 0$ in the reference frame. In practice, the coil would be constructed and located in the MRI apparatus relative to its physical center, of course.

For the RTS coils considered here, the domain of θ becomes

$$\theta \in [-N\pi + \theta_{\text{offset}},\, N\pi + \theta_{\text{offset}}]\,,$$

where N is the total number of turns.

We first consider the regular case with $\theta_{\text{offset}} = 0$. The central plane of the coil along the z-axis is defined by

$$z_{\text{central}} = \frac{z_{\max} + z_{\min}}{2}. \tag{5.1}$$

The derivation of the central plane expression is provided in Appendix A. The result is

$$z_{\text{central}} = A \sin\varphi. \tag{5.2}$$

This equation shows that the location of the central plane depends on the winding shift φ, and in particular,

$$z_{\text{central}} = \begin{cases} 0, & \text{for } \varphi = 2m\pi, \\ \neq 0, & \text{for } \varphi = \dfrac{(2m+1)\pi}{2}, \end{cases} \qquad m = 0, 1, 2, \ldots \tag{5.3}$$

Thus, when $\varphi = 0$, the physical central plane is at $z = 0$.

We now consider an offset in the start and end position of θ, which gives new values of z_{min} and z_{max} and therefore shifts the physical central plane. The central plane is then given by

$$z_{\text{central}} = \frac{h\,\theta_{\text{offset}}}{2\pi} + A\sin(2\theta_{\text{offset}} + \varphi)\,, \tag{5.4}$$

which is equivalent to Eq. (5.2) when $\theta_{\text{offset}} = 0$.

For the coil configurations considered here,

$$\theta_{\text{offset}} = \frac{m\pi}{2}, \qquad m = 0, 1, 2, 3. \tag{5.5}$$

In this case,

$$z_{\text{central}} = \frac{mh}{4} + (-1)^m A\sin\varphi. \tag{5.6}$$

Finally, for the present analysis, where $\varphi = 0$,

$$z_{\text{central}} = \frac{mh}{4}, \qquad m = 0, 1, 2, 3. \tag{5.7}$$

Thus, shifting the angular location of the return wire changes the physical central plane of the coil, and the B_1 field must be evaluated relative to this shifted plane. As a result, the central plane of the shifted RTS coil, in the z-coordinate, for the angles mentioned here is $z = 0, h/4, h/2, 3h/2$.

As shown in Fig. 5.6(a) and (c), for $\theta_{\text{offset}} = 0$ and π, the return wire lies in the $y = 0$ plane (at $x = +a$ and $-a$, respectively) and will contributes most strongly to the B_{1y} component. Figure 5.6(b) and (d) show that for $\theta_{\text{offset}} = \pi/2$ and $3\pi/2$ the return wire lies in the $x = 0$ plane (at $y = +a$ and $-a$, respectively) and will contributes most strongly to the B_{1x} component, which does not enter into the definition of the transverse RF field B_1 given in Eq. 4.39.

The results of the B_1 evaluation in the central plane of each RTS coil are shown in Fig.5.7, together with those of the DLTS coil for comparison. The results for the RTS coil with $\theta_{\text{offset}} = 0$ and for the DLTS coil are identical to those presented in the central column of Fig. 5.5.

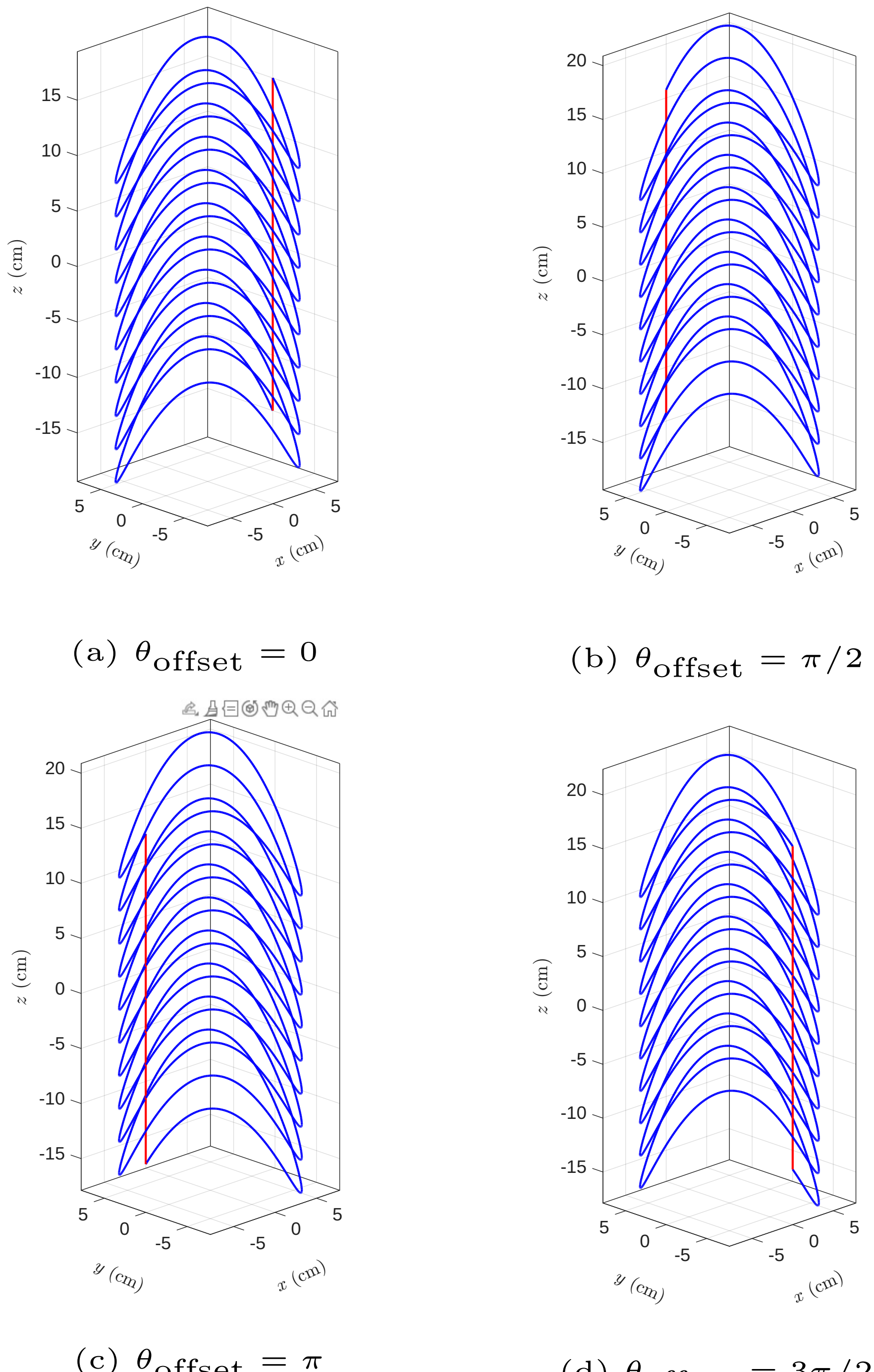

(a) $\theta_{\text{offset}} = 0$

(b) $\theta_{\text{offset}} = \pi/2$

(c) $\theta_{\text{offset}} = \pi$

(d) $\theta_{\text{offset}} = 3\pi/2$

Figure 5.6: RTS coil geometry showing the effect of the angular offset of the return wire. Panels (a)–(d) correspond to $\theta_{\text{offset}} = 0$, $\pi/2$, π, and $3\pi/2$, respectively. The return wire is highlighted in red.

As shown in Fig. 5.7, moving the return wire to the $x = 0$ plane, i.e., choosing $\theta_{\text{offset}} = \pi/2$ or $3\pi/2$, greatly improves the $\mathbf{B}_1$ field characteristics defined of Eqs. 4.39 through 4.41. Despite this improvement, the results also show that the DLTS coil remains the superior design across all evaluated metrics, including $|B_1|$ homogeneity, B_1 phase linearity, and G_x homogeneity. It should also be noted that the main RF field contribution of the improved RTS coils is still present; however, it is shifted from the B_{1y} component to the B_{1x} component. If $B_0 \gg B_{1x}$, the impact of this term is expected to be negligible [53, 63]. This would not be the case in very low B_0 fields, however [75]. Regardless, the strong RF field generated by the return wire of an RTS coil, and its potentially deleterious effects, can be completely eliminated by adopting a DLTS design.

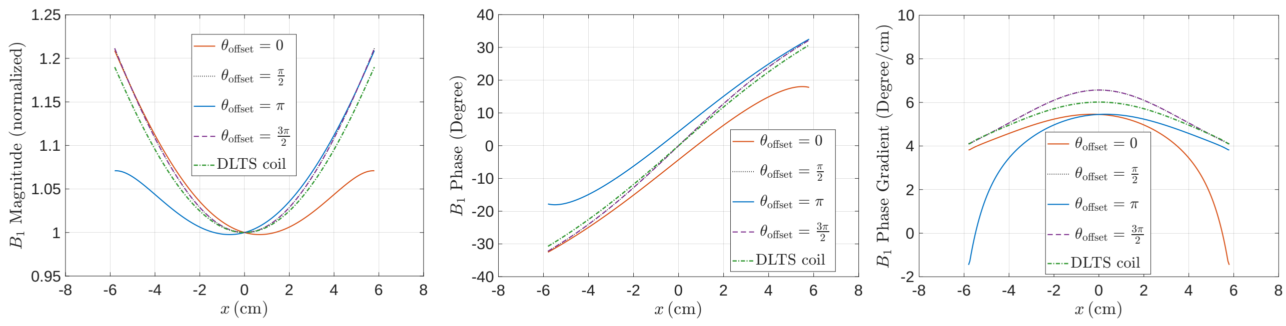

Figure 5.7: Comparison of the RTS coil for four different offset angles and the DLTS coil: B_1 magnitude (left), phase (middle), and phase gradient (right) along the x-axis in the central plane. The single legend refers to all panels.

5.6 Summary

Overall, the numerical analyses presented in this chapter demonstrate that while the RTS configuration suffers from a field asymmetry introduced by the return wire, which can be improved for high field applications by adding a winding offset, both the DWTS and DLTS winding patterns preserve the desired RF phase-gradient characteristics outright.

Chapter 6

Comparison of Truncated Twisted Solenoid Designs

6.1 Introduction

In TRASE MRI, the length of twisted solenoid coils increases with modulation amplitude, which limits their use in compact imaging systems. Truncated twisted solenoid designs have therefore been proposed to reduce coil length while preserving the RF phase gradient required for encoding [65]. In this chapter, we investigate the effect of truncation on twisted solenoid geometries and extend the truncation approach from existing RTS coils to our new DLTS designs. The resulting magnetic field characteristics are again evaluated using Biot–Savart simulations.

6.2 Truncation method

To reduce the overall length of the twisted solenoid coils while maintaining the phase gradient strength and field uniformity, a truncated coil design was introduced in Ref. [65]. In this approach, the z-coordinate of each point on the coil is restricted so that the winding remains within a specific axial length. Mathematically, the original z-coordinate $P_z(\theta)$ is mapped to a truncated coordinate $P'_z(\theta)$ according to the formula

$$P'_z(\theta) = \begin{cases} P_z(\theta), & \text{if } |P_z(\theta)| \leq \dfrac{L}{2} - pg, \\ \dfrac{L}{2} - pg, & \text{if } P_z(\theta) > \dfrac{L}{2} - pg, \\ pg - \dfrac{L}{2}, & \text{if } P_z(\theta) < pg - \dfrac{L}{2}, \end{cases} \tag{6.1}$$

where $P_z(\theta)$ is from Eq. (4.29), L is the desired axial length of the truncated coil, g is the axial truncation gap, and p is a non-negative integer starting from zero, used to define where the truncation process considers the "next turn" to begin. The truncation expression in Eq. (6.1) is based on Ref. [65]. A schematic illustration of all truncation parameters is provided in Fig. 6.1

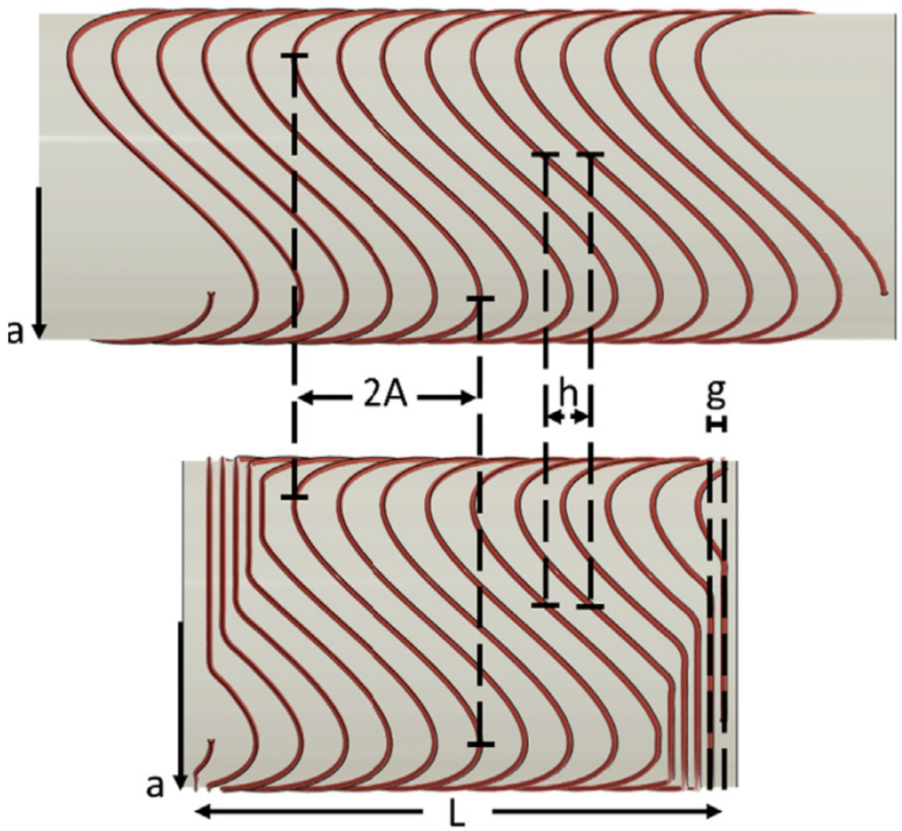

Figure 6.1: Schematic illustration of truncation parameters. The top figure shows an untruncated twisted solenoid. The bottom one shows a truncated, twisted solenoid of length L. In this figure, A is the modulation amplitude, h is the pitch, and g is the parameter for the truncation gap. (Image taken from Ref. [65], with permission from Elsevier under license number 6184291486091.)

To fit the twisted solenoid length within a prescribed axial length L, a progressive turn-wise truncation strategy was applied. The method constrains the axial coordinate of the coil in a controlled manner near both ends, while leaving the central turns unchanged whenever they already satisfy the axial limits. The truncation procedure is presented step by step below.

- **Step 1: Identify points outside the axial bounds.**

  The twisted solenoid coil trajectory is first generated according to Table 5.1. The radial components describe a circular winding of radius a, which need not be included in the truncation process. In contrast, the axial coordinate $P_z(\theta)$, on which the entire truncation process depends, consists of a sinusoidal modulation with amplitude A, superimposed on a linear term that produces an axial pitch h per turn. Thus, the coil has a certain number of turns, denoted by N, and each turn is discretized into a specified number of points. The number of points used in the simulation determines the numerical accuracy.

- **Step 2: Assign turn indices and define the truncation limits.**

  This step involves shortening the coil to a length L. To do this, we must identify all points along the coil that lie outside the turn-dependent axial bounds derived from the interval $[-L/2, +L/2]$. Any point beyond these bounds is flattened back into the allowed interval so that the coil fits within the desired length. However, there is an important condition: we cannot simply flatten all turns uniformly to exactly $\pm L/2$, because the coil's shape and the spacing between its turns must be preserved. This is where Eq. (6.1) is applied.

  This equation involves two primary parameters. The first parameter, p, is an integer starting at 0 that indicates how the truncation process proceeds from the outermost turns of the coil toward its center. Specifically, for the outermost turns located at the two ends of the coil, p is set to 0. As we move inward toward the center, p increases by one with each subsequent turn, reflecting the progression of truncation from the outer turn inward. The second parameter is g, as shown in Fig. 6.1, which represents the incremental vertical offset between the truncation boundaries of successive turns. This parameter remains constant for all truncated turns.

  For the outermost turns on either side of the coil with $p = 0$, the boundaries are positioned at $-L/2$ and $+L/2$ from Eq. 6.1, which define the initial limits of the truncated turns. Moving inward, for the next turn where $p = 1$, these boundaries are no longer at the original positions but are shifted inward by a distance g. For example, instead of being at $-L/2$ and $+L/2$, the boundaries are now located at

  $$-\left(\frac{L}{2} - g\right) \quad \text{and} \quad +\left(\frac{L}{2} - g\right),$$

  respectively.

  Overall, this process gradually compresses each turn in a controlled manner, preserving the coil's winding pattern (and field profile) near the centre and ensuring that the entire structure fits neatly within the length L. The truncation procedure described in Steps 1 and 2 is illustrated in Fig. 6.2, which shows both the axial coordinate representation and the corresponding three-dimensional geometry of the twisted solenoid before and after truncation. Because the truncation is applied separately to each coil turn, small axial jumps may appear between neighboring turns in the truncated regions. This can be seen in Fig. 6.2(d), where jumps are clearly visible in the upper part of the coil. The origin of these jumps and how they can be removed are described in the next step.

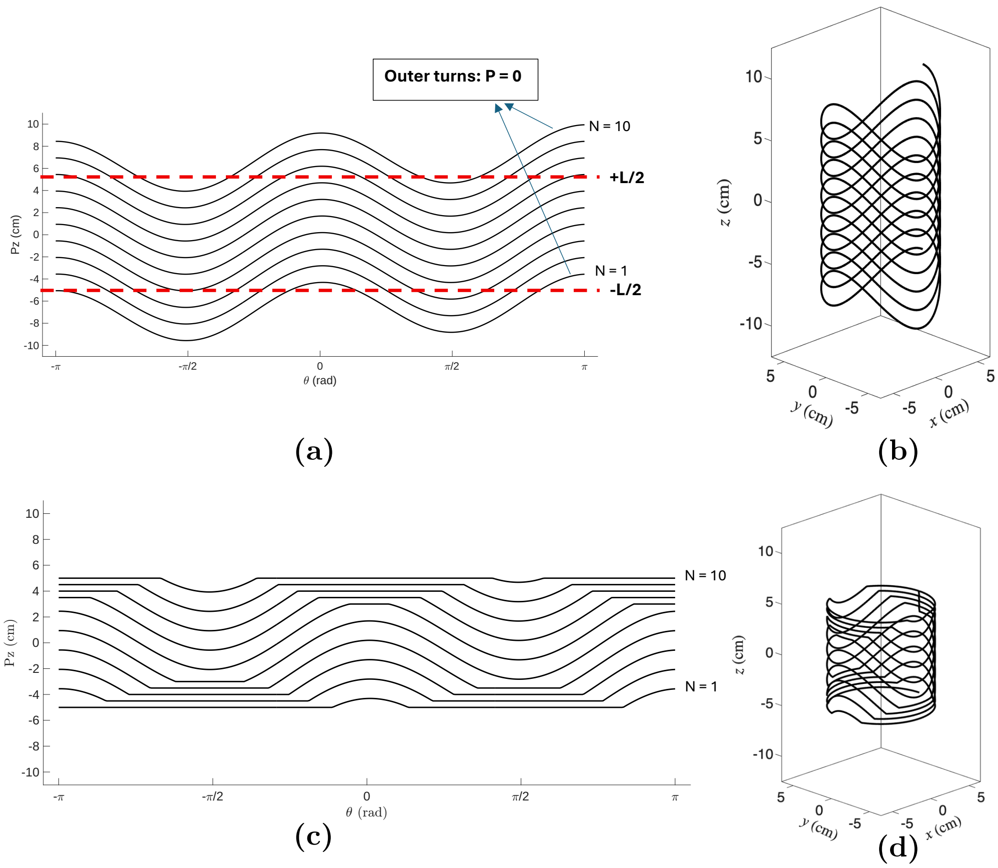

Figure 6.2: Depictions of the untruncated and truncated twisted solenoid coil. (a) Axial coordinate P_z of individual turns as a function of the winding parameter θ prior to truncation. The dashed red lines indicate the desired axial bounds $\pm L/2$. Several outermost turns $p = 0, 1, 2, 3$ clearly exceed these limits. (b) Three-dimensional view of the untruncated twisted solenoid. (c) Axial coordinate P_z' after applying the progressive turn-wise truncation strategy described in Step 2, showing that all turns are confined within the axial extent $[-L/2, +L/2]$ while preserving the central winding pattern. (d) Corresponding three-dimensional view of the truncated coil geometry. The winding parameters for both coils here are $N = 10$, $a = 5.0$ cm, $L = 10$ cm, $A = 2.44$ cm, $\phi = 90°$, $g = 0.05$ cm and $h = 1.5$ cm.

- **Step 3: Apply truncation and verify geometric continuity.**

  At this stage, the truncation step has been completed. However, as discussed earlier, several axial jumps remain visible in the upper part of the coil, as can be seen in Fig. 6.3. These jumps arise because the change from one outer turn (e.g., $p = 0$) to the next one (e.g., $p = 1$) sometimes occurs in the middle of a section of the coil that needs to be truncated or flattened. However, because of the jump in p value here, there ends up being a jump in what would preferably be a flat wire section. As a result, the transition between two consecutive truncated turns introduces a discontinuity in the axial direction.

  To eliminate these jumps, an additional numerical procedure is applied, if necessary, to reorder the points assigned to each truncation level $\pm(L/2 - pg)$. In this step, the truncated points of each turn that exceed the final axial position of the preceding turn are adjusted to match that value. In this way, the transition between successive turns becomes continuous, and the axial discontinuities are effectively removed. This effect is illustrated in Fig. 6.3, where the axial coordinate is plotted as a function of the winding angle over the full range from $-N\pi$ to $+N\pi$. The discontinuities are clearly visible before reordering. Figure 6.4 shows the final version of the truncated twisted solenoid following the reordering process of $P_z(\theta)$.

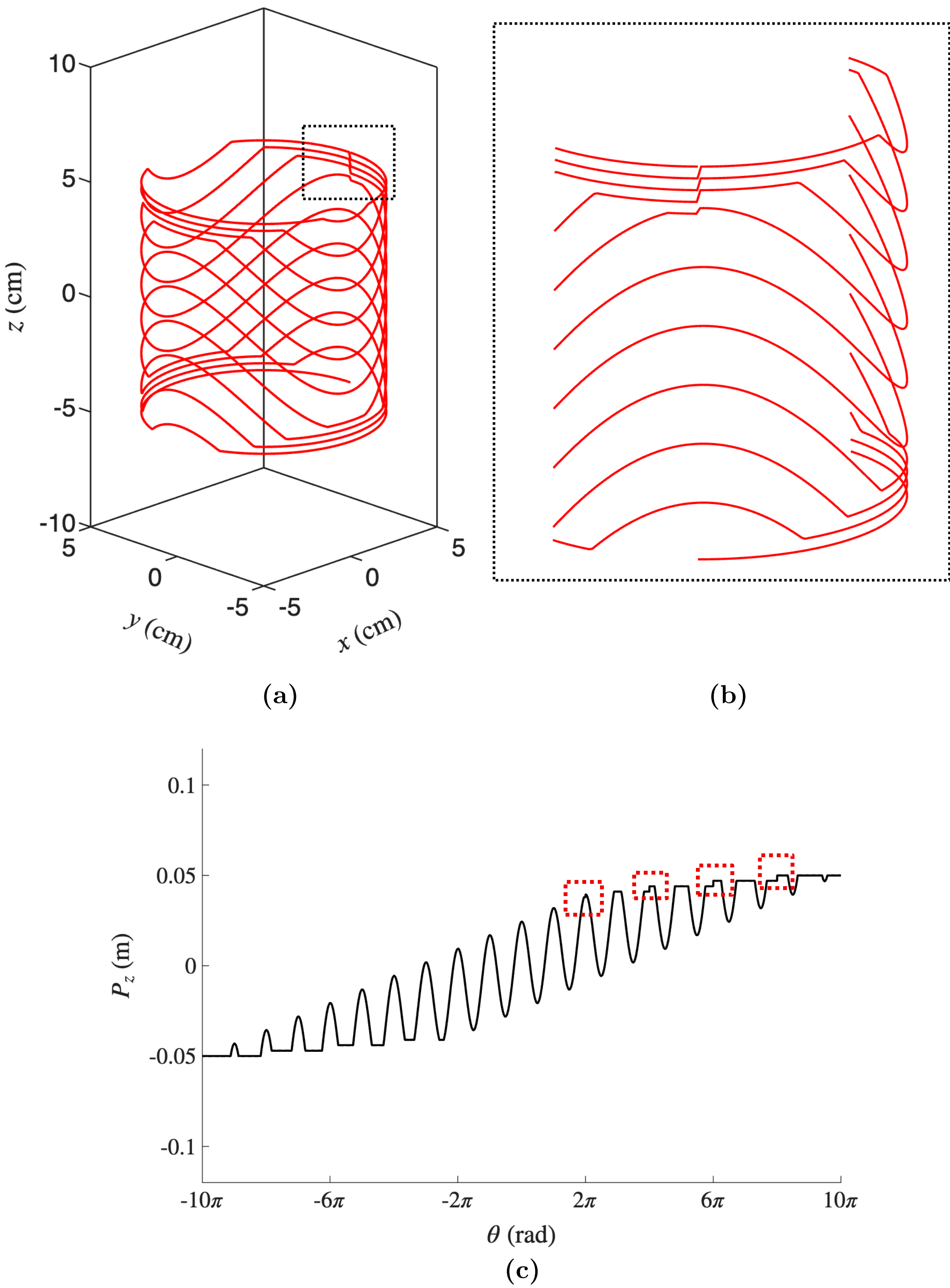

Figure 6.3: Axial coordinate P_z as a function of the winding parameter θ for a truncated twisted solenoid coil with 10 turns. (a) shows the truncated winding geometry before applying the reordering procedure, with the dashed box indicating a region where discontinuities occur between adjacent turns. (b) The zoomed view highlights the axial transitions at these turn-to-turn connections. (c) $P_z(\theta)$ as a function of the winding parameter θ prior to reordering, where the axial jumps are visible and marked by red boxes.

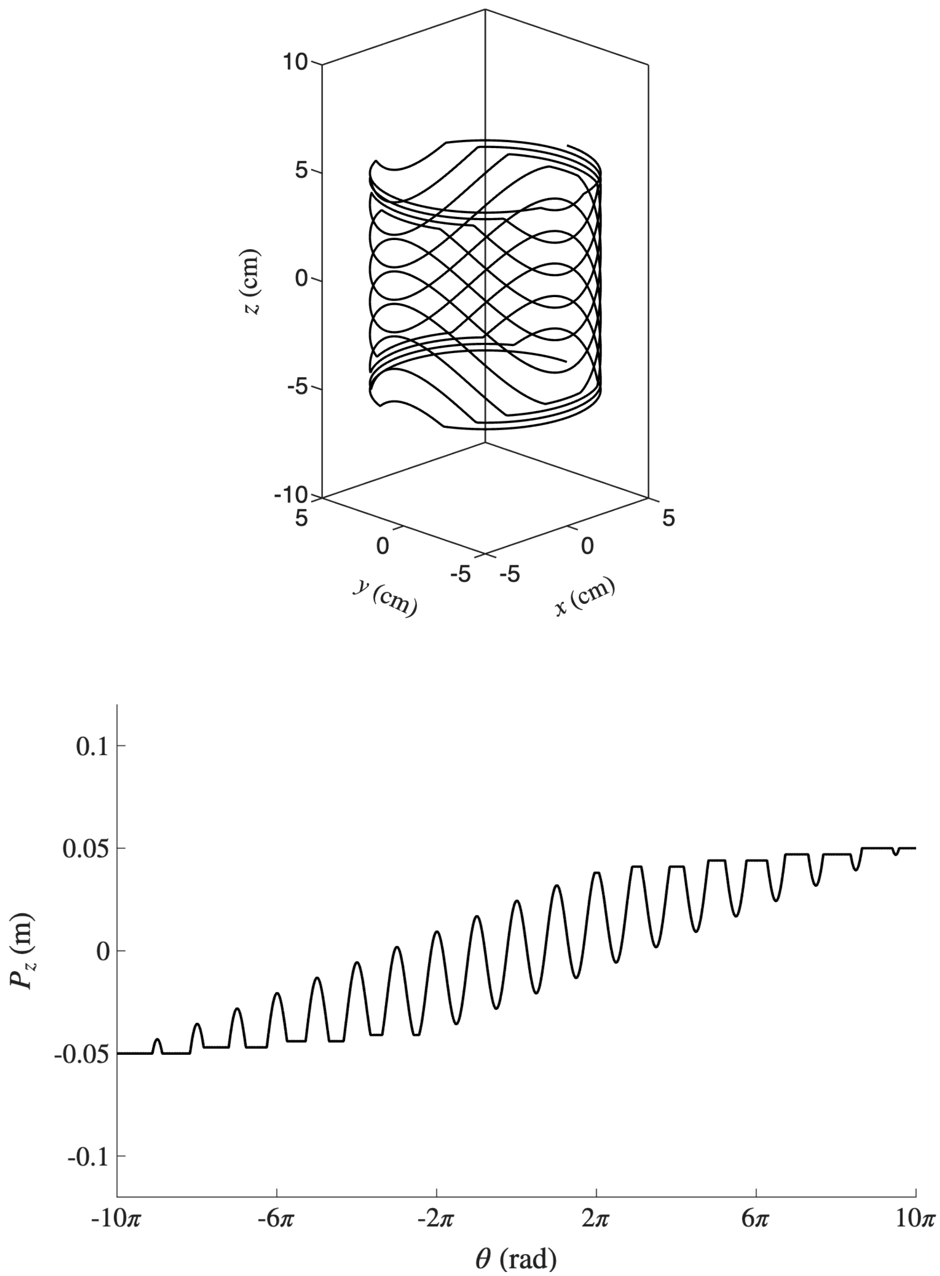

Figure 6.4: The top figure shows the 3D truncated twisted solenoid, and below one is P_z as a function of the winding parameter θ after applying a reordering step.

Note that changing the winding phase shift (φ) shifts where truncation affects each turn. In some cases, the truncated region appears at the start of a turn, whereas in others it appears at the end.

Consequently, the resulting axial jump may occur either at the beginning or at the end of the turn. Accordingly, the reordering procedure is applied in a direction consistent with the location of the truncated segment within each turn.

After applying the truncation and reordering procedures described above, the resulting coil geometry remains continuous while satisfying the prescribed axial constraint. The truncated design can therefore be used directly in the Biot–Savart simulations used to evaluate the RF magnetic field properties.

6.3 Results

In this section, results are presented for two twisted solenoid coil configurations: a truncated real twisted solenoid with a return wire (RTS) and a truncated twisted solenoid composed of discrete loops (DLTS). All previously reported truncated coil results in Ref. [65] correspond to RTS geometries and serve as the primary reference for understanding the effects of truncation on the B_1 magnitude and phase. Building on these results, the RTS configuration is examined to evaluate how the inclusion of the return wire alters the B_1 magnitude and phase. In contrast, the impact of truncation on the DLTS coil design is also investigated.

6.3.1 Truncated RTS coil

The truncated twisted solenoid coils considered here are based on the designs reported in Ref. [65]. In that study, pairs of coils, referred to as inner and outer coils, were used to generate transverse phase gradients in opposite directions, which are required for spatial encoding in TRASE MRI. From the range of configurations investigated in Ref. [65], the inner and outer coils that exhibited the best overall performance, based on criteria such as B_1 field uniformity, magnitude, and phase gradient strength, were selected for use in this work. These selected coil parameters have been reproduced in Table 6.1. Both coils employ a 90° winding shift to generate a transverse phase gradient $-G_y$, perpendicular to the static magnetic field B_0. To obtain a phase gradient in the opposite direction, the outer coil is physically rotated by 90° about the z-axis, resulting in a $+G_y$ field.

The effects of truncation on the B_1 magnitude and phase of twisted solenoid coils without a return wire have been examined in detail in Ref. [65]. In that work, truncation was shown to preserve the transverse B_1 phase gradient while improving the usable imaging volume. In the following, attention is restricted to the additional field variations introduced by the inclusion of a return wire in the truncated geometry.

Parameter	Inner Coil	Outer Coil
Number of turns (N)	16	15
Coil radius (a)	5 cm	6.25 cm
Twist amplitude (A)	2.44 cm	3.32 cm
Winding shift (φ)	90°	90°
Turn advance (h)	1.5 cm	1.7 cm
Axial length of truncated coil (L)	20 cm	
Truncation gap (g)	0.5 cm	

Table 6.1: Winding parameters of the inner and outer truncated twisted solenoid coils used as reference designs. The axial truncation length and truncation gap are identical for both coils. Values taken from Ref. [65].

Figures 6.5 and 6.6 show the simulated B_1 magnitude and phase distributions for the truncated inner and outer real twisted solenoid (RTS) coils, respectively. The left panels illustrate the truncated winding geometries, while the right panels present transverse contour maps of the B_1 magnitude (top row) and B_1 phase (bottom row) at three axial positions ($z = -5$ cm, $z = 0$ cm, and $z = 5$ cm), obtained from Biot–Savart simulations.

For both the inner and outer RTS coils, the B_1 magnitude exhibits noticeable spatial nonuniformity across the transverse plane. Distortions are most evident near the periphery of the field of view, where the field deviates from the nearly uniform behavior expected for an ideal twisted solenoid. These deviations arise primarily from the additional current segment introduced by the return wire, which perturbs the otherwise symmetric current distribution even in the truncated coil configuration.

The corresponding B_1 phase maps reveal the presence of a transverse phase gradient along the $-y$-direction for the outer RTS coil and along the $+y$-direction for the inner RTS coil, consistent with the relative 90° rotation between the two designs. In both cases, however, the phase distributions deviate from an ideal linear profile. The phase contours are unevenly spaced across the transverse plane, indicating nonlinear phase behavior. These distortions are particularly visible near the edges of the imaging region and vary with axial position. Such behavior indicates that the return wire introduces a perturbation to the sinusoidal current pattern, degrading both the magnitude uniformity and the linearity of the phase distribution.

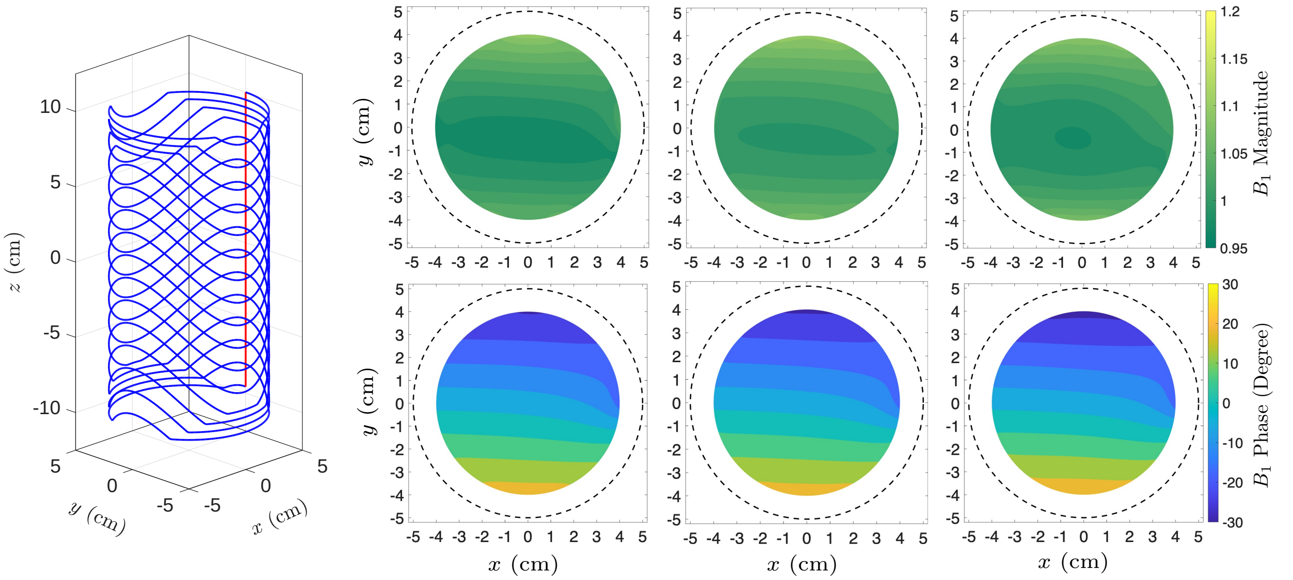

Figure 6.5: Results for the truncated version of the inner RTS coil. The left plot shows the winding pattern. The top row of contour plots on the right displays B_1 magnitude maps at three axial planes (left: $z = -5$ cm, middle: $z = 0$ cm, and right: $z = 5$ cm), while the bottom row shows the corresponding B_1 phase maps. The dashed line indicates the coil winding surface.

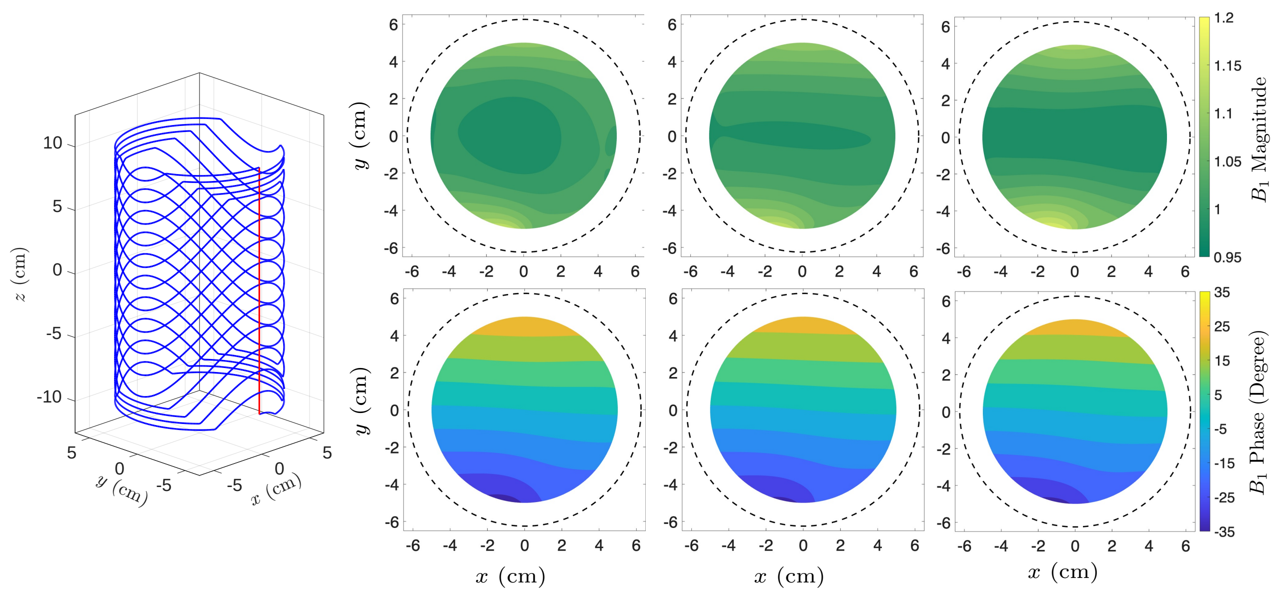

Figure 6.6: Results for the truncated outer RTS coil. The left panel shows the winding geometry. The top row of contour plots on the right displays B_1 magnitude maps at three axial planes ($z = -5$ cm, $z = 0$ cm, and $z = 5$ cm), while the bottom row shows the corresponding B_1 phase maps. The dashed line indicates the coil winding surface.

6.3.2 Truncated DLTS coil

Figures 6.7 and 6.8 show the simulated B_1 magnitude and phase distributions for the truncated inner and outer twisted solenoid coils composed of discrete loops (DLTS), respectively. The DLTS coils are generated using the same winding and truncation parameters listed in Table. 6.1, ensuring a direct comparison with the truncated RTS configuration. As in the RTS case, the left panels illustrate the truncated winding geometries, while the right panels present transverse contour maps of the B_1 magnitude (top row) and B_1 phase (bottom row) at three axial positions ($z = -5$ cm, $z = 0$ cm, and $z = 5$ cm), obtained from Biot–Savart simulations.

In contrast to the RTS configuration, the DLTS coils exhibit improved B_1 magnitude uniformity across the transverse plane. The magnitude maps show reduced spatial variation both near the center and toward the periphery of the field of view, with fewer localized distortions. This behavior is observed for both the inner and outer DLTS coils and is maintained across all axial positions considered. The improved uniformity is attributed to the absence of a return wire and the discrete loop structure, which preserves a symmetric current distribution around the coil. With the elimination of the return wire found in the RTS design, the symmetry of the winding is maintained, and no degradations are introduced into the transmit field.

The corresponding B_1 phase maps display a well-defined transverse phase gradient for both DLTS coils. Compared to the RTS case, the DLTS phase distributions exhibit reduced deviations from linearity and more uniform spacing of the phase contours across the transverse plane. The phase patterns remain qualitatively consistent across the three axial positions, indicating that the discretized geometry preserves a stable and approximately linear transverse phase distribution.

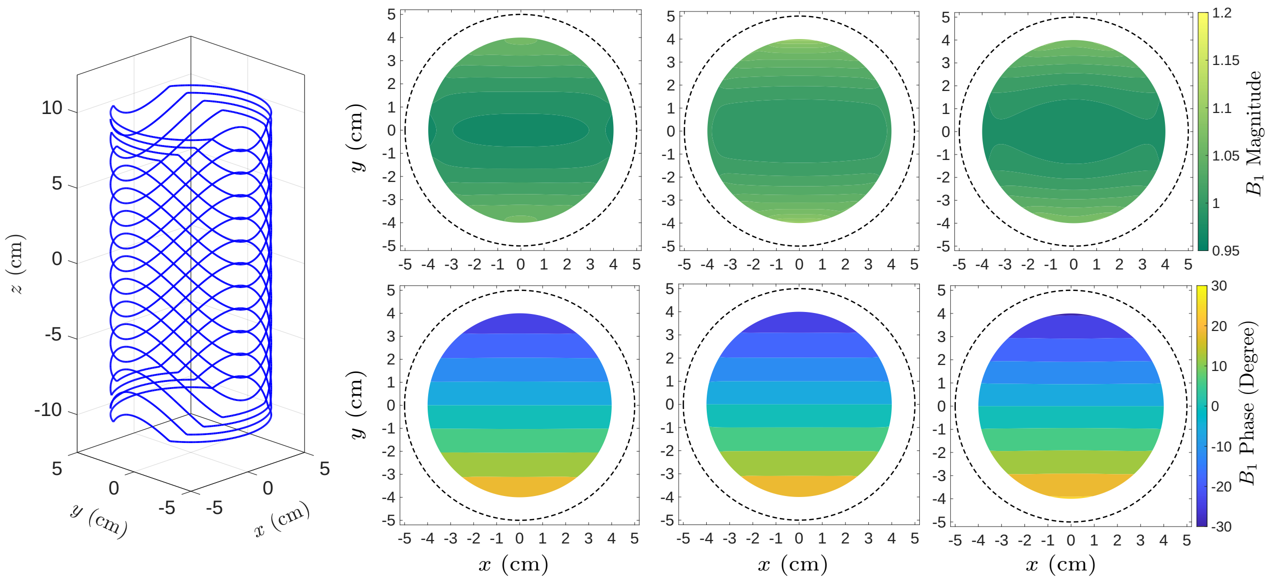

Figure 6.7: Results for the truncated version of the inner DLTS coil. The left plot shows the winding pattern. The top row of contour plots on the right displays B_1 magnitude maps at three axial planes (left: $z = -5$ cm, middle: $z = 0$ cm, and right: $z = 5$ cm), while the bottom row shows the corresponding B_1 phase maps. The dashed line indicates the coil winding surface.

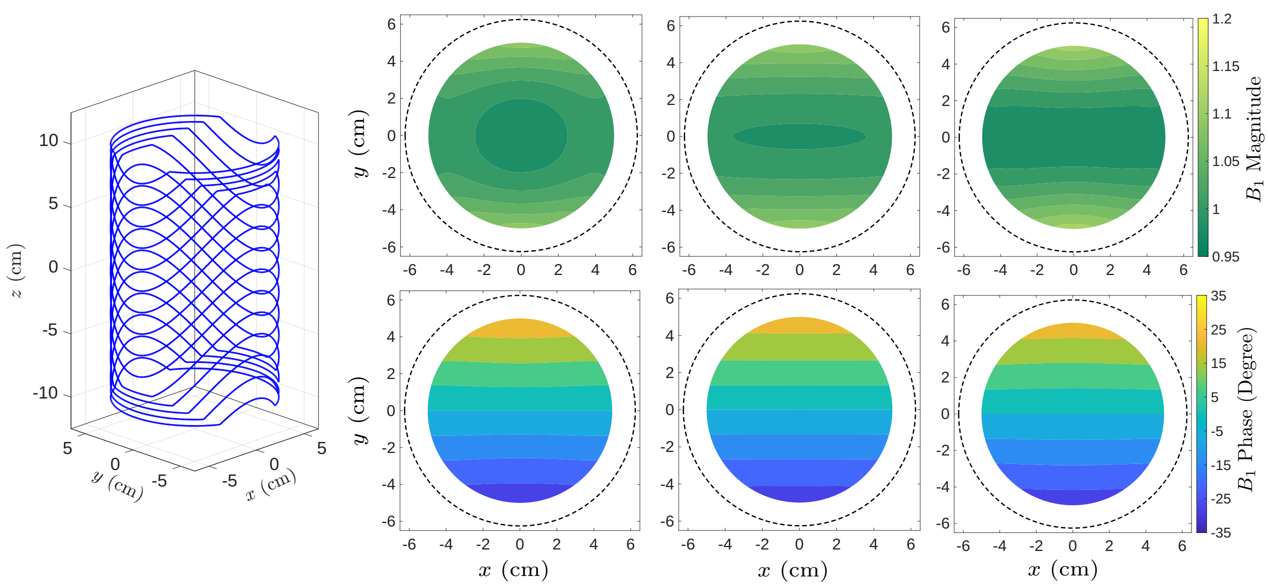

Figure 6.8: Results for the truncated outer DLTS coil. The left panel shows the winding geometry. The top row of contour plots on the right displays B_1 magnitude maps at three axial planes ($z = -5$ cm, $z = 0$ cm, and $z = 5$ cm), while the bottom row shows the corresponding B_1 phase maps. The dashed line indicates the coil winding surface.

Although there is negligible difference in the central field magnitude and phase gradient strength between the corresponding versions of the coils, as summarized in Table 6.2, the DLTS preserves the main magnetic and phase characteristics. In particular, the DLTS winding pattern provides clear improvement in B_1 magnitude uniformity and phase behavior compared to the standard RTS design, while maintaining the desired phase gradient. With the DLTS requiring only about 3% more wire to construct, these improvements are achieved without a significant compromise in coil complexity.

Coil type	$\lvert B_1(0,0,0)\rvert$ (μT/A)	$\bar{G}_y$ (deg/cm)	Wire length (m)
RTS inner	78.57	-5.67	6.02
DLTS inner	78.38	-5.75	6.21
RTS outer	68.44	5.13	7.09
DLTS outer	68.33	5.12	7.28

Table 6.2: Summary of nominal characteristics of the inner and outer truncated RTS and DLTS coils. Shown are the magnitude of B_1 at the coil isocenter, the mean transverse phase gradient $\bar{G}_y$, and the total wire length. The value of $\bar{G}_y$ is calculated along the y-axis at $x = z = 0$ over the imaging volume diameter used in Ref. [65] (i.e., 80% of the inner coil diameter or 8 cm).

These results indicate that the DLTS winding pattern preserves the essential magnetic field characteristics of the twisted solenoid while eliminating the symmetry-breaking effects introduced by the return wire. As a result, the DLTS configuration provides a more uniform transmit field and improved phase behavior while maintaining comparable phase gradient strength.

Figures 6.9 and 6.10 present a comparison between the RTS and DLTS designs, showing the B_1 magnitude, phase, and phase gradient along the y-axis for the inner and outer coils introduced earlier, evaluated within 80% of the coil radius. As can be observed in Fig. 6.9, corresponding to the inner coil, our DLTS design preserves symmetry even in the truncated configurations, resulting in a more uniform magnetic field and improved linearity of the magnetic field phase. DLTS coil demonstrates enhanced performance compared to the RTS coil, and this improvement can be attributed to the unavoidable influence of the return wire in the RTS configuration, which degrades the field characteristics unless its position is modified, as discussed in Chapter 5.

Figure 6.10 presents a similar analysis for the outer coil, which has been rotated by 90° about the z-axis. This rotation changes the location of the return wire, and an improvement in the RTS field is observed. This observation is consistent with our previous discussion that modifying the return wire location can improve field performance. However, the plot clearly shows that the DLTS design remains the more favorable choice, as it exhibits better RF field characteristics, particularly in the phase gradient distribution.

n.

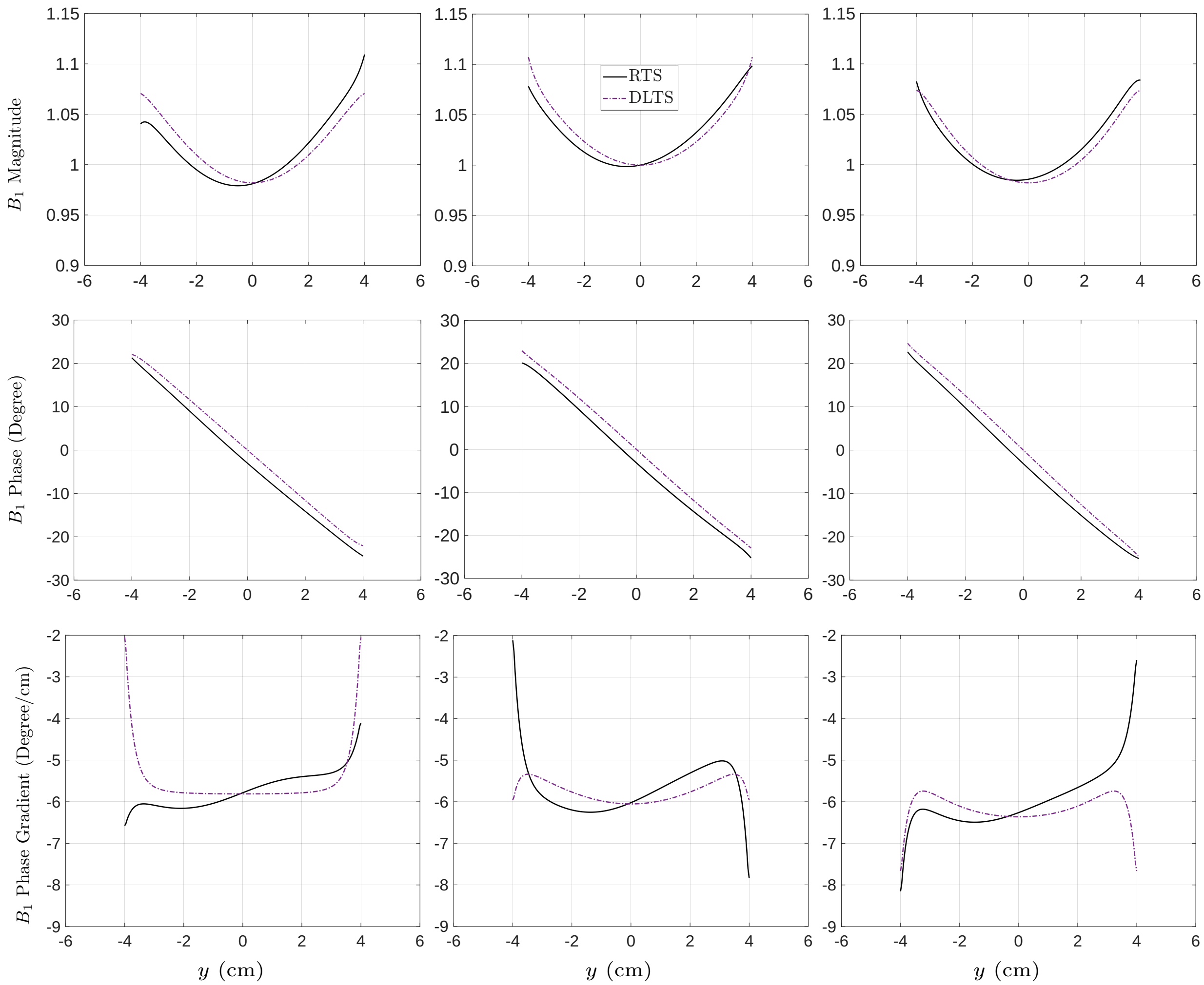

Figure 6.9: B_1 magnitude, phase, and phase gradient along the y-axis for $x = 0$ in three axial planes: $z = -5\,\mathrm{cm}$ (left), $z = 0\,\mathrm{cm}$ (middle), and $z = 5\,\mathrm{cm}$ (right), across inner RTS and inner DLTS. The single legend applies to all panels.

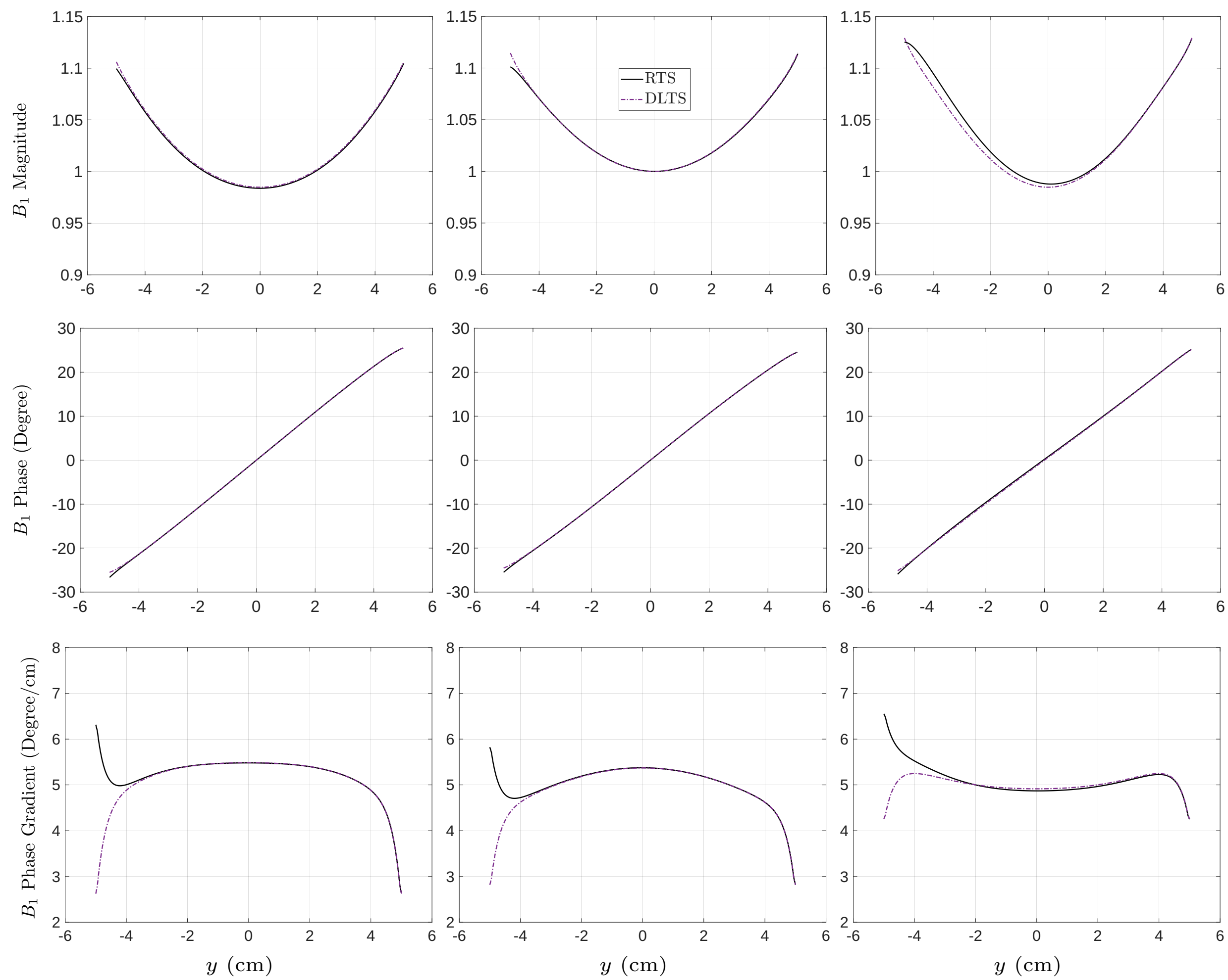

Figure 6.10: B_1 magnitude, phase, and phase gradient along the y-axis for $x = 0$ in three axial planes: $z = -5\,\mathrm{cm}$ (left), $z = 0\,\mathrm{cm}$ (middle), and $z = 5\,\mathrm{cm}$ (right), across outer RTS and outer DLTS. The outer coil is rotated 90° about the z-axis relative to the inner coil, producing a $+G_y$ phase gradient. The single legend applies to all panels.

Chapter 7

Conclusion and future works

7.1 Conclusions

This thesis presented a comparative study of twisted solenoid winding patterns for RF phase-gradient coils used in TRASE MRI systems employing vertical B_0 magnets. The main objective of this work was to investigate alternative winding patterns capable of improving the B_1 field uniformity and phase linearity compared to existing twisted solenoid designs.

The incomplete twisted solenoid (ITS) has previously been used as a conceptual model for guiding TRASE coil design. However, this configuration does not represent a physically realizable coil because it neglects the return wire that must be present in practical implementations. When this return wire is included, forming a real twisted solenoid (RTS) coil, its additional current segment introduces unwanted RF field contributions that degrade the B_1 magnitude uniformity and phase linearity. The severity of these distortions depends on both the azimuthal location of the return wire and the orientation of the generated phase gradient.

To address these limitations, two alternative winding configurations were investigated: the double-wound twisted solenoid (DWTS) and the discrete-loop twisted solenoid (DLTS). Both designs eliminate the asymmetric current contribution associated with the return wire by preserving a symmetric current distribution around the coil. Using Biot–Savart simulations, the magnetic field characteristics of these configurations were evaluated with parameters corresponding to several RTS coil designs reported in previous works, including coils that produce phase gradients along the x- and y-directions, truncated geometries, and rotated configurations.

The results showed that both the DWTS and DLTS coils successfully preserve the desired transverse phase gradient while improving the uniformity and linearity of the B_1 field compared to the RTS design.

Among these two alternatives, the DLTS coil offers a practical advantage because it requires less wire than the DWTS configuration and therefore reduces the risk of finite-wavelength effects at typical operating frequencies.

Furthermore, the DLTS geometry was shown to be particularly well-suited for truncated coil designs, allowing a reduction in coil length while maintaining the desired RF field characteristics. The DLTS winding pattern is directly derived from the stream function coil design method, which may enable additional design flexibility in future work.

Given that twisted solenoid coils for TRASE MRI are commonly constructed using 3D-printed coil formers, the transition from RTS designs to either the DWTS or DLTS configurations can be implemented with minimal modification to existing fabrication methods. In addition, a novel strategy was presented for shifting the azimuthal position of the return wire in RTS coils, providing an alternative approach for mitigating its adverse effects.

7.2 Future Work

While the present study focused on numerical modeling and Biot–Savart simulations of twisted solenoid coil geometries, several directions for future work remain. The next step would be the fabrication of the proposed DLTS and DWTS coils and the experimental validation of their RF magnetic field characteristics. Measurements of the B_1 magnitude, phase, and phase gradient could be performed using experimental measurement methods to directly compare the results with the numerical predictions presented in this thesis.

Furthermore, TRASE imaging experiments using these coil designs would allow the impact of the improved phase gradient coils on image quality and spatial resolution to be assessed in practice. Such experiments would provide valuable confirmation of the advantages predicted by the simulation results.

Appendices

Appendix A

Derivation of the Central Plane for Shifted RTS Coils

In Section 5.5 of Chapter 5, the effect of shifting the angular location of the return wire in the RTS coil is analyzed. This shift is implemented through a physical rotation of the coil, which results in a corresponding change in the location of its central plane. In this appendix, the expression for the central plane of the twisted solenoid is derived for a physically rotated coil configuration. The general expression for the central plane of a twisted coil is defined as follows:

$$z_{\text{central}} = \frac{z_{\text{max}} + z_{\text{min}}}{2}. \tag{A.1}$$

For the twisted solenoid, the extrema are given by

$$z_{\text{max}} = A\sin(2N\pi + \varphi) + \frac{hN\pi}{2\pi}, \tag{A.2}$$

$$z_{\text{min}} = A\sin(-2N\pi + \varphi) + \frac{h(-N\pi)}{2\pi}. \tag{A.3}$$

Substituting into the definition of the central plane gives

$$\begin{aligned} z_{\text{central}} &= \frac{1}{2}\left[A\sin(2N\pi + \varphi) + \frac{hN}{2} + A\sin(-2N\pi + \varphi) - \frac{hN}{2}\right] \\ &= \frac{A}{2}\left[\sin(2N\pi + \varphi) + \sin(-2N\pi + \varphi)\right]. \end{aligned} \tag{A.4}$$

Using $\sin(\pm 2N\pi + \varphi) = \sin\varphi$, we obtain

$$z_{\text{central}} = A\sin\varphi. \tag{A.5}$$

For the rotated case, the angular limits become

$$\theta \in \left[-N\pi + \theta_{\text{offset}},\ N\pi + \theta_{\text{offset}}\right].$$

Therefore,

$$
\begin{aligned}
z_{\text{min}} &= A\sin[n(-N\pi+\theta_{\text{offset}})+\varphi] + \frac{h(-N\pi+\theta_{\text{offset}})}{2\pi} \\
&= A\sin(-2N\pi+2\theta_{\text{offset}}+\varphi) - \frac{hN}{2} + \frac{h\theta_{\text{offset}}}{2\pi},
\end{aligned} \tag{A.6}
$$

and

$$
\begin{aligned}
z_{\text{max}} &= A\sin[n(N\pi+\theta_{\text{offset}})+\varphi] + \frac{h(N\pi+\theta_{\text{offset}})}{2\pi} \\
&= A\sin(2N\pi+2\theta_{\text{offset}}+\varphi) + \frac{hN}{2} + \frac{h\theta_{\text{offset}}}{2\pi}.
\end{aligned} \tag{A.7}
$$

Hence,

$$
\begin{aligned}
z_{\text{central}} &= \frac{z_{\text{max}}+z_{\text{min}}}{2} \\
&= \frac{A\sin(-2N\pi+2\theta_{\text{offset}}+\varphi) + A\sin(2N\pi+2\theta_{\text{offset}}+\varphi) + \dfrac{h\theta_{\text{offset}}}{\pi}}{2}.
\end{aligned} \tag{A.8}
$$

Using $\sin(\pm 2N\pi + x) = \sin x$, this becomes

$$
\begin{aligned}
z_{\text{central}} &= \frac{h\theta_{\text{offset}}}{2\pi} + \frac{A}{2}\left[\sin(2\theta_{\text{offset}}+\varphi) + \sin(2\theta_{\text{offset}}+\varphi)\right] \\
&= \frac{h\theta_{\text{offset}}}{2\pi} + A\sin(2\theta_{\text{offset}}+\varphi).
\end{aligned} \tag{A.9}
$$

For

$$\theta_{\text{offset}} = \frac{m\pi}{2}, \qquad m = 0, 1, 2, 3, \tag{A.10}$$

and using

$$\sin(m\pi + \varphi) = (-1)^m \sin\varphi, \tag{A.11}$$

the central plane becomes

$$z_{\text{central}} = \frac{mh}{4} + (-1)^m A\sin\varphi. \tag{A.12}$$

Finally, for $\varphi = 0$,

$$z_{\text{central}} = \frac{mh}{4}, \qquad m = 0, 1, 2, 3. \tag{A.13}$$

Bibliography

[1] G. Katti, S. A. Ara, and A. Shireen, "Magnetic resonance imaging (MRI)–a review," *International journal of dental clinics*, vol. 3, no. 1, pp. 65–70, 2011.

[2] E. Pagani, A. Bizzi, F. Di Salle, N. De Stefano, and M. Filippi, "Basic concepts of advanced MRI techniques," *Neurological Sciences*, vol. 29, no. Suppl 3, pp. 290–295, 2008.

[3] E. Moser, F. Stahlberg, M. E. Ladd, and S. Trattnig, "$7-T$ (MR)—from research to clinical applications," *NMR in Biomedicine*, vol. 25, no. 5, pp. 695–716, 2012.

[4] R. A. Bell, "Economics of MRI technology," *Journal of Magnetic Resonance Imaging*, vol. 6, no. 1, pp. 10–25, 1996.

[5] S. Murali, H. Ding, F. Adedeji, C. Qin, J. Obungoloch, I. Asllani, U. Anazodo, N. A. Ntusi, R. Mammen, T. Niendorf, *et al.*, "Bringing MRI to low-and middle-income countries: directions, challenges and potential solutions," *NMR in Biomedicine*, vol. 37, no. 7, p. e4992, 2024.

[6] A. E. Campbell-Washburn, K. E. Keenan, P. Hu, J. P. Mugler III, K. S. Nayak, A. G. Webb, J. Obungoloch, K. N. Sheth, J. Hennig, M. S. Rosen, *et al.*, "Low-field MRI: a report on the 2022 ISMRM workshop," *Magnetic resonance in medicine*, vol. 90, no. 4, pp. 1682–1694, 2023.

[7] T. C. Arnold, C. W. Freeman, B. Litt, and J. M. Stein, "Low-field MRI: clinical promise and challenges," *Journal of Magnetic Resonance Imaging*, vol. 57, no. 1, pp. 25–44, 2023.

[8] A. Samardzija, K. Selvaganesan, H. Z. Zhang, H. Sun, C. Sun, Y. Ha, G. Galiana, and R. T. Constable, "Low-field, low-cost, point-of-care magnetic resonance imaging," *Annual Review of Biomedical Engineering*, vol. 26, 2024.

[9] J. C. Sharp and S. B. King, "MRI using radiofrequency magnetic field phase gradients," *Magnetic Resonance in Medicine: An Official Journal of the International Society for Magnetic Resonance in Medicine*, vol. 63, no. 1, pp. 151–161, 2010.

[10] J. C. Sharp, S. B. King, Q. Deng, V. Volotovskyy, and B. Tomanek, "High-resolution MRI encoding using radiofrequency phase gradients," *NMR in Biomedicine*, vol. 26, no. 11, pp. 1602–1607, 2013.

[11] C. J. Sedlock, B. Tomanek, and J. C. Sharp, "Twisted solenoid B1 field and isolation requirements for two-coil radial trase," *Journal of Magnetic Resonance*, p. 108056, 2026.

[12] I. I. Rabi, J. R. Zacharias, S. Millman, and P. Kusch, "A new method of measuring nuclear magnetic moment," *Physical review*, vol. 53, no. 4, p. 318, 1938.

[13] F. Bloch, "Nuclear induction," *Physical review*, vol. 70, no. 7-8, p. 460, 1946.

[14] E. M. Purcell, H. C. Torrey, and R. V. Pound, "Resonance absorption by nuclear magnetic moments in a solid," *Physical review*, vol. 69, no. 1-2, p. 37, 1946.

[15] P. C. Lauterbur, "Image formation by induced local interactions: examples employing nuclear magnetic resonance," *nature*, vol. 242, no. 5394, pp. 190–191, 1973.

[16] A. Kumar, D. Welti, and R. R. Ernst, "NMR fourier zeugmatography," *Journal of Magnetic Resonance (1969)*, vol. 18, no. 1, pp. 69–83, 1975.

[17] R. Damadian, M. Goldsmith, and L. Minkoff, "NMR in cancer: Xvi. fonar image of the uve human body," *Physiological chemistry and physics*, vol. 9, no. 1, pp. 97–100, 1977.

[18] D. B. Plewes and W. Kucharczyk, "Physics of MRI: a primer," *Journal of magnetic resonance imaging*, vol. 35, no. 5, pp. 1038–1054, 2012.

[19] M. A. Brown and R. C. Semelka, *MRI: basic principles and applications.* John Wiley & Sons, 2011.

[20] R. W. Brown, Y.-C. N. Cheng, E. M. Haacke, M. R. Thompson, and R. Venkatesan, *Magnetic resonance imaging: physical principles and sequence design.* John Wiley & Sons, 2014.

[21] M. H. Levitt, *Spin dynamics: basics of nuclear magnetic resonance.* John Wiley & Sons, 2008.

[22] J. P. Ridgway, "Generating a signal: RF pulses and echoes," in *Cardiovascular MR Manual*, pp. 21–29, Springer, 2015.

[23] M. A. Bernstein, K. F. King, and X. J. Zhou, *Handbook of MRI pulse sequences.* Elsevier, 2004.

[24] C. M. Collins and Z. Wang, "Calculation of radiofrequency electromagnetic fields and their effects in MRI of human subjects," *Magnetic resonance in medicine*, vol. 65, no. 5, pp. 1470–1482, 2011.

[25] S. D. Serai, K. Ruppert, S. Chawla, and S. Jambawalikar, "MR physics, hardware considerations, and practical steps for clinical mri of the kidney," in *Advanced Clinical MRI of the Kidney: Methods and Protocols*, pp. 13–46, Springer, 2023.

[26] S. D. Serai, M.-L. Ho, M. Artunduaga, S. S. Chan, and G. B. Chavhan, "Components of a magnetic resonance imaging system and their relationship to safety and image quality," *Pediatric radiology*, vol. 51, no. 5, pp. 716–723, 2021.

[27] E. N. Manson, S. Inkoom, and A. N. Mumuni, "Impact of magnetic field inhomogeneity on the quality of magnetic resonance images and compensation techniques: a review," *Reports in Medical Imaging*, pp. 43–56, 2022.

[28] J. Zhao, M. Zhu, L. Xia, Y. Fan, and F. Liu, "A novel passive shimming optimization method of MRI magnet based on a psa-sqp hybrid algorithm," *Scientific Reports*, vol. 15, no. 1, p. 28419, 2025.

[29] D. G. Norris and J. M. Hutchison, "Concomitant magnetic field gradients and their effects on imaging at low magnetic field strengths," *Magnetic resonance imaging*, vol. 8, no. 1, pp. 33–37, 1990.

[30] S. S. Hidalgo-Tobon, "Theory of gradient coil design methods for magnetic resonance imaging," *Concepts in Magnetic Resonance Part A*, vol. 36, no. 4, pp. 223–242, 2010.

[31] P. Volegov, J. Mosher, M. Espy, and R. Kraus Jr, "On concomitant gradients in low-field MRI," *Journal of Magnetic Resonance*, vol. 175, no. 1, pp. 103–113, 2005.

[32] D. A. Yablonskiy, A. L. Sukstanskii, and J. J. Ackerman, "Image artifacts in very low magnetic field MRI: the role of concomitant gradients," *Journal of Magnetic Resonance*, vol. 174, no. 2, pp. 279–286, 2005.

[33] M. A. Jacobs, T. S. Ibrahim, and R. Ouwerkerk, "MR imaging: brief overview and emerging applications," *Radiographics*, vol. 27, no. 4, pp. 1213–1229, 2007.

[34] Q. Wang, "Hardware of MRI system," in *Nuclear Magnetic Resonance*, IntechOpen, 2019.

[35] W. E. Kwok, "Basic principles of and practical guide to clinical MRI radiofrequency coils," *Radio-Graphics*, vol. 42, no. 3, pp. 898–918, 2022.

[36] W. Foltz and D. Jaffray, "Principles of magnetic resonance imaging," *Radiation research*, vol. 177, no. 4, pp. 331–348, 2012.

[37] S. Plein, J. Greenwood, J. P. Ridgway, *et al.*, *Cardiovascular MR manual.* Springer, 2011.

[38] J. P. Ridgway, "Cardiovascular magnetic resonance physics for clinicians: part I," *Journal of cardiovascular magnetic resonance*, vol. 12, no. 1, p. 71, 2010.

[39] F. B. W. H. M. Packard, F. Bloch, and W. Hansen, "The nuclear induction experiment," *Physical Review*, vol. 70, no. 7-8, pp. 474–485, 1946.

[40] C. B. Paschal and H. D. Morris, "K-space in the clinic," *Journal of Magnetic Resonance Imaging: An Official Journal of the International Society for Magnetic Resonance in Medicine*, vol. 19, no. 2, pp. 145–159, 2004.

[41] M. Hori, A. Hagiwara, M. Goto, A. Wada, and S. Aoki, "Low-field magnetic resonance imaging: its history and renaissance," *Investigative radiology*, vol. 56, no. 11, pp. 669–679, 2021.

[42] C. Z. Cooley, J. P. Stockmann, B. D. Armstrong, M. Sarracanie, M. H. Lev, M. S. Rosen, and L. L. Wald, "Two-dimensional imaging in a lightweight portable mri scanner without gradient coils," *Magnetic resonance in medicine*, vol. 73, no. 2, pp. 872–883, 2015.

[43] Z. H. Ren, L. Maréchal, W. Luo, J. Su, and S. Y. Huang, "Magnet array for a portable magnetic resonance imaging system," in *2015 IEEE MTT-S 2015 International Microwave Workshop Series on RF and Wireless Technologies for Biomedical and Healthcare Applications (IMWS-BIO)*, pp. 92–95, IEEE, 2015.

[44] C. Z. Cooley, P. C. McDaniel, J. P. Stockmann, S. A. Srinivas, S. F. Cauley, M. Śliwiak, C. R. Sappo, C. F. Vaughn, B. Guerin, and M. S. Rosen, "A portable scanner for magnetic resonance imaging of the brain," *Nature biomedical engineering*, vol. 5, no. 3, pp. 229–239, 2021.

[45] T. O'Reilly, W. Teeuwisse, and A. Webb, "Three-dimensional MRI in a homogenous 27 cm diameter bore Halbach array magnet," *Journal of Magnetic Resonance*, vol. 307, p. 106578, 2019.

[46] T. O'Reilly, W. M. Teeuwisse, D. de Gans, K. Koolstra, and A. G. Webb, "In vivo 3D brain and extremity MRI at 50 mT using a permanent magnet Halbach array," *Magnetic resonance in medicine*, vol. 85, no. 1, pp. 495–505, 2021.

[47] K. Koolstra, T. O'Reilly, P. Börnert, and A. Webb, "Image distortion correction for MRI in low field permanent magnet systems with strong B_0 inhomogeneity and gradient field nonlinearities," *Magnetic Resonance Materials in Physics, Biology and Medicine*, vol. 34, no. 4, pp. 631–642, 2021.

[48] K. Selvaganesan, Y. Ha, H. Sun, Z. Zhang, C. Sun, A. Samardzija, G. Galiana, and R. T. Constable, "Encoding scheme design for gradient-free, nonlinear projection imaging using Bloch-Siegert RF spatial encoding in a low-field, open MRI system," *Scientific Reports*, vol. 14, no. 1, p. 3307, 2024.

[49] S. A. Srinivas, J. B. Martin, C. E. Vaughn, and W. A. Grissom, "Linear bloch–siegert phase-encoded low-field MRI: RF coils, pulse sequence, and image reconstruction," *NMR in Biomedicine*, vol. 37, no. 12, p. e5245, 2024.

[50] D. Hoult, "Rotating frame zeugmatography," *Journal of Magnetic Resonance (1969)*, vol. 33, no. 1, pp. 183–197, 1979.

[51] G. E. Sarty and L. Vidarsson, "Magnetic resonance imaging with RF encoding on curved natural slices," *Magnetic resonance imaging*, vol. 46, pp. 47–55, 2018.

[52] D. Hoult, "Rotating frame zeugmatography," *Philosophical Transactions of the Royal Society of London. B, Biological Sciences*, vol. 289, no. 1037, pp. 543–547, 1980.

[53] Q. Deng, S. B. King, V. Volotovskyy, B. Tomanek, and J. C. Sharp, "B_1 transmit phase gradient coil for single-axis TRASE RF encoding," *Magnetic resonance imaging*, vol. 31, no. 6, pp. 891–899, 2013.

[54] Q. Qin, "Point spread functions of the $T2$ decay in k-space trajectories with long echo train," *Magnetic resonance imaging*, vol. 30, no. 8, pp. 1134–1142, 2012.

[55] H. Sun, "Radio-frequency transmit coils and imaging techniques for trase mri," 2020.

[56] J. P. Stockmann, C. Z. Cooley, B. Guerin, M. S. Rosen, and L. L. Wald, "Transmit array spatial encoding (TRASE) using broadband wurst pulses for RF spatial encoding in inhomogeneous B0 fields," *Journal of Magnetic Resonance*, vol. 268, pp. 36–48, 2016.

[57] P.-J. Nacher, S. Kumaragamage, G. Tastevin, and C. P. Bidinosti, "A fast MOSFET RF switch for low-field NMR and MRI," *Journal of magnetic resonance*, vol. 310, p. 106638, 2020.

[58] C. Goodzeit, M. Ball, and R. Meinke, "The double-helix dipole-a novel approach to accelerator magnet design," *IEEE transactions on applied superconductivity*, vol. 13, no. 2, pp. 1365–1368, 2003.

[59] R. Meinke, C. Goodzeit, and M. Ball, "Modulated double-helix quadrupole magnets," *IEEE transactions on applied superconductivity*, vol. 13, no. 2, pp. 1369–1372, 2003.

[60] J. Alonso, A. Soleilhavoup, A. Wong, A. Guiga, and D. Sakellariou, "Double helix dipole design applied to magnetic resonance: A novel NMR coil," *Journal of Magnetic Resonance*, vol. 235, pp. 32–41, 2013.

[61] L. Queval and R. Gottkehaskamp, "Analytical field calculation of modulated double helical coils," *IEEE Transactions on Applied Superconductivity*, vol. 25, no. 6, pp. 1–7, 2015.

[62] S. Yong, B. Tomanek, and J. C. Sharp, "The twisted solenoid RF phase gradient transmit coil for TRASE imaging," *Proc. of the Intl. Soc. Mag. Reson. Med.*, vol. 25, p. 4281, 2017.

[63] H. Sun, S. Yong, and J. C. Sharp, "The twisted solenoid RF phase gradient transmit coil for TRASE imaging," *Journal of Magnetic Resonance*, vol. 299, pp. 135–150, 2019.

[64] H. Sun, A. AlZubaidi, A. Purchase, and J. C. Sharp, "A geometrically decoupled, twisted solenoid single-axis gradient coil set for TRASE," *Magnetic resonance in medicine*, vol. 83, no. 4, pp. 1484–1498, 2020.

[65] C. J. Sedlock, A. R. Purchase, B. Tomanek, and J. C. Sharp, "A truncated twisted solenoid RF phase gradient transmit coil for TRASE MRI," *Journal of Magnetic Resonance*, vol. 347, p. 107361, 2023.

[66] L. Quéval and R. Gottkehaskamp, "Analytical field calculation of modulated double helical coils," *IEEE Transactions on Applied Superconductivity*, vol. 25, no. 6, pp. 1–7, 2015.

[67] G. N. Peeren, "Stream function approach for determining optimal surface currents," *Journal of Computational Physics*, vol. 191, no. 1, pp. 305–321, 2003.

[68] M. A. Brideson, L. K. Forbes, and S. Crozier, "Determining complicated winding patterns for shim coils using stream functions and the target-field method," *Concepts in Magnetic Resonance: an Educational Journal*, vol. 14, no. 1, pp. 9–18, 2002.

[69] C. Bidinosti, I. Kravchuk, and M. Hayden, "Active shielding of cylindrical saddle-shaped coils: Application to wire-wound rf coils for very low field NMR and MRI," *Journal of Magnetic Resonance*, vol. 177, no. 1, pp. 31–43, 2005.

[70] J. Jin, J. Chen, W. Chew, H. Gan, R. Magin, and P. Dimbylow, "Computation of electromagnetic fields for high-frequency magnetic resonance imaging applications," *Physics in Medicine & Biology*, vol. 41, no. 12, p. 2719, 1996.

[71] T. S. Ibrahim, R. Lee, A. M. Abduljalil, B. A. Baertlein, and P.-M. L. Robitaille, "Dielectric resonances and B_1 field inhomogeneity in UHFMRI: computational analysis and experimental findings," *Magnetic resonance imaging*, vol. 19, no. 2, pp. 219–226, 2001.

[72] T. S. Ibrahim, Y.-K. Hue, and L. Tang, "Understanding and manipulating the RF fields at high field MRI," *NMR in Biomedicine: An International Journal Devoted to the Development and Application of Magnetic Resonance In vivo*, vol. 22, no. 9, pp. 927–936, 2009.

[73] J. D. Hanson and S. P. Hirshman, "Compact expressions for the biot–savart fields of a filamentary segment," *Physics of Plasmas*, vol. 9, no. 10, pp. 4410–4412, 2002.

[74] J. Alonso, A. Soleilhavoup, A. Wong, A. Guiga, and D. Sakellariou, "Double helix dipole design applied to magnetic resonance: A novel NMR coil," *Journal of Magnetic Resonance*, vol. 235, pp. 32–41, 2013.

[75] C. B. Bidinosti, P.-J. Nacher, and G. Tastevin, "Concomitant B_1 field in low-field MRI: Potential contributions to TRASE image artefacts," in *Joint annual meeting ISMRM-ESMRMB 2018*, vol. 26, p. 2670, 2018.

[76] C.-N. Chen and D. I. Hoult, *Biomedical magnetic resonance technology*, vol. 100. Adam Hilger Bristol, 1989.

[77] P. Bohidar, H. Sun, J. C. Sharp, and G. E. Sarty, "The effects of coupled B_1 fields in B_1 encoded TRASE MRI - A simulation study," *Magnetic Resonance Imaging*, vol. 74, pp. 74–83, 2020.